Centre for Catalysis Research

Department of Chemical Engineering

University of Cape Town

Study of the effects of promoters (MnO_x and FeO_x) on Co_3O_4/CeO_2 during Preferential Oxidation of Carbon monoxide

Author: Noluvuyo Ndila

Supervisor: Prof. Patricia J. Kooyman

Submitted in partial fulfillment of the requirements for the degree of Master of Science in Chemical Engineering

Acknowledgments

I would like to thank God for His grace and for giving me the strength to complete my MSc journey.

I would like to thank my supervisor, Professor Patricia Kooyman, for her guidance which has helped me throughout my MSc. Thank you for your patience and constant support in my academics and personal life. Lastly, thank you for seeing potential in me and for every opportunity you have given me.

I would like to thank the Vice-Chancellor for the Womxn for Womxn grant which made it possible to complete this study and to travel to attend conferences.

Thank you to the Norwegian Centre of Transmission Electron Microscopy for giving us time in their Centre time to perform the elemental mapping. Thank you to Martin Jensen from the University of Oslo for performing some of the elemental mappings of my catalysts.

Thank you to the technical staff in the lab for their training and assistance when using lab equipment.

I would like to sincerely thank my friends: Somila Mateza, Shaine Raeseela, and Motlokoa Khasu. Thank you for your support, encouragement, and willingness to always listen.

Last but not least thank you to my parents and siblings (Zizo and Zusaluse), for their continuous love and emotional support.

Plagiarism Declaration

I, Noluvuyo Ndila, hereby declare that the work on which this thesis is based is my original work (except where acknowledgements indicate otherwise) and that neither the whole work nor any part of it has been, is being, or is to be submitted for another degree in this or any other university. I authorize the University to reproduce for the purpose of research either the whole or any portion of the contents in any manner whatsoever.

Signature: Signed by candidate Date: 11/02/2022

Conference contributions

2019

N. Ndila and P.J. Kooyman

Study of the effects of promoters (MnO_x and FeO_x) on Co_3O_4/CeO_2 during CO-PROX.

Poster presentation at the 29th Annual Conference of the Catalysis Society of South Africa (CATSA), Western Cape, South Africa.

N. Ndila and P.J. Kooyman

Study of the effects of promoters (MnO_x and FeO_x) on Co_3O_4/CeO_2 during CO-PROX.

Poster presentation at the 56th Congress of the Microscopy Society of South Africa (MSSA), Western Cape, South Africa.

2021

N. Ndila, M. Jensen, and P.J. Kooyman

Study of the effects of promoters (MnO_x and FeO_x) on Co_3O_4/CeO_2 during CO-PROX.

Poster presentation at the 31st Annual Conference of the Catalysis Society of South Africa (CATSA), online conference.

Synopsis

The provision of sustainable, clean, safe, reliable, and affordable energy towards the advancement of the quality of life in all societies is goal 7 of the United Nations sustainable development goals . Currently, most energy production relies on the use of fossil fuels (Büyüközkan, Karabulut and Mukul, 2018). However, these have negative environmental impacts such as global warming, land degradation, and water pollution (Haryanto et al., 2005). Hence there is an urgent need for improving access to eco-friendly and reliable energy alternatives.

One of the leading and promising pollution-free high-energy carriers is hydrogen for fuel cells. Currently, hydrogen gas is mostly produced via steam reforming followed by the water-gas shift reaction (Edwards et al., 2008). However, the concern with using this hydrogen in fuel cells is the carbon monoxide content which is between 0.5-1.0 vol % (Liu, Song & Subramani, 2010). Carbon monoxide is poisonous to the platinum anode of the fuel cell so it needs to be reduced to below 10 ppm before being introduced in the fuel cell (Liu, Song & Subramani, 2010).

One of the methods for carbon monoxide removal is preferential oxidation (PROX) of carbon monoxide to carbon dioxide. This process has been identified as being cost-effective, much easier to implement, and ensures minimum loss of hydrogen when compared to other techniques such as selective CO methanation and pressure swing adsorption (Park, Lee and Lee, 2009).

Catalysts used for CO-PROX are either noble metal or transition metal oxide based. Noble metal-based catalysts have a low CO oxidation activity at temperatures below 200 °C, higher cost, and lower availability when compared to transition metal-based catalysts (Kahlich, Gasteiger & Behm, 1997; Grisel et al., 2002). Of the transition metal oxides, Co_3O_4 and CuO are the most active catalysts for CO-PROX (Woods et al., 2010).

The active species for CO oxidation in Co_3O_4 catalysts is the Co^{3+}/Co^{2+} redox pair. However, during CO-PROX at temperatures above 200 °C, Co_3O_4 reduces to metallic Co which is active for CO methanation (Nyathi, 2016; Khasu, 2017). This is undesirable as CO methanation results in H_2 consumption, hence the stability of the Co_3O_4 phase above 200 °C is crucial. In this study, our objective is to investigate the effects of the promoters MnO_x and FeO_x on the stability of the Co_3O_4 phase supported on CeO_2 and CO-PROX activity.

Monodispersed Co_3O_4 nanoparticles were synthesized via a surfactant-free non-aqueous thermal method. 10 wt.% Co_3O_4 was supported and promoted via wet impregnation using ultrasonication. The addition of the promoters improves the redox properties of Co_3O_4. TPR showed an increase in the reduction temperature of Co_3O_4, while TPO showed a decrease in the re-oxidation temperature of metallic Co. Additionally, CO-TPRE showed that the promoted catalysts have a higher oxygen storage capacity when compared to the unpromoted catalyst.

Catalytic performance evaluation was performed in a fixed bed reactor in the feed gas 1 % CO, 1 % O_2, 47 % H_2, and 51 % N_2 from 50 to 450 °C. The onset temperature for CO methanation on Co_3O_4/CeO_2 was 275 °C and the highest CO conversion achieved was 70% at 220 °C. The addition of 0.3 wt.% MnO_x does not change the onset temperature for CO methanation. However, CO conversion increased to 84 % between 240-260 °C. An increase in the MnO_x content to 0.5 wt.% increases the onset temperature for CO methanation to 300 °C and the highest CO conversion achieved was 98 % from 200-240 °C. A further increase in MnO_x to 1 wt.% increases the CO methanation onset temperature to 310 °C, however, the CO conversion decreases to 92 % from 180-200 °C. The decrease in the optimum temperature for the 0.5 wt.% MnO_x promoted catalysts might be beneficial

Addition of 0.3 wt.% FeO_x increases the onset temperature for CO methanation when compared to the unpromoted catalyst to 300 °C. Furthermore, CO conversion increased to 84% between 240-260 °C. An increase in the FeO_x content to 0.5 wt.% does not change the onset temperature for CO

methanation but the highest CO conversion achieved was 100 % from 210-220 °C. A further increase in FeO_x to 1 wt.% increases the CO methanation onset temperature to 310 °C, however, the CO conversion decreases to 88 % from 220-230 °C.

Contents

List of Figures

List of Tables

Nomenclature

Abbreviations

CO-PROX	Preferential Oxidation of Carbon monoxide
CO-SMET	Selective methanation of Carbon monoxide
CO-TPD	Carbon monoxide Temperature programmed desorption
CO-TPRE	Carbon monoxide Temperature programmed reaction
DFT	Density Functional state Theory
DOR	Degree of reduction
DRIFTS	Diffuse Reflectance Infrared Fourier Transform Spectroscopy
EDX	Energy-Dispersive X-ray spectroscopy
GC	Gas chromatography
GHSV	Gas hourly space velocity
HRTEM	High-Resolution Transmission Electron Microscopy
ICP-OES	Inductively coupled plasma –optical emission spectroscopy
MFC	Mass Flow Controller
MvK	Mars van Krevelen
NTP	Normal temperature and pressure (298.15 K and 1 atm)
PEMFC	Polymer electrolyte membrane fuel cell
PGMs	Platinum group metals
PXRD	Powder X-ray diffraction
RWGS	Reverse water gas shift
STEM	Scanning Transmission Electron Microscopy
TCD	Thermal conductivity detector
TEM	Transmission Electron Microscopy
TPO	Temperature programmed oxidation
TPR	Temperature programmed reduction
WGS	Water gas shift

1 Introduction

Goal 7 of the United Nations' Sustainable Development goals seeks to promote and stimulate international cooperation and engagement on sustainable energy-related technologies and infrastructure. Currently, most energy production relies on the use of fossil fuels (Büyüközkan, Karabulut and Mukul, 2018). However, these have negative environmental impacts such as global warming, land degradation, and water pollution (Haryanto et al., 2005). Hence there has been more research and development focusing on improving access to eco-friendly and reliable energy alternatives.

One of the leading and promising pollution-free high energy carriers that is receiving considerable attention is hydrogen. The primary advantage is that H_2 can be obtained from diverse sources. Some of the raw materials that are H_2 sources are water and hydrocarbons (Edwards et al., 2008).

Currently, some of the industries that utilize H_2 are methanol and ammonia production, metallurgy, and the pharmaceutical industry (Bičáková and Straka, 2010). However, because of its high power density and clean combustion (it doesn't produce carbon dioxide emissions), it is an energy source in fuel cells (Haryanto et al., 2005).

Fuel cells are electrochemical devices that convert the chemical energy of a fuel and an oxidant (O_2) directly into electrical energy as shown in figure 1.1 (Giorgi and Leccese, 2013). A variety of fuels can be used in fuel cells, however, H_2 is the most effective because of its higher electrochemical reactivity compared to hydrocarbons (Giorgi and Leccese, 2013). Fuel cells can have efficiencies of up to 60 %, can continuously generate electricity as long as fuel and air are supplied, and have no polluting emissions (Edwards et al., 2008).

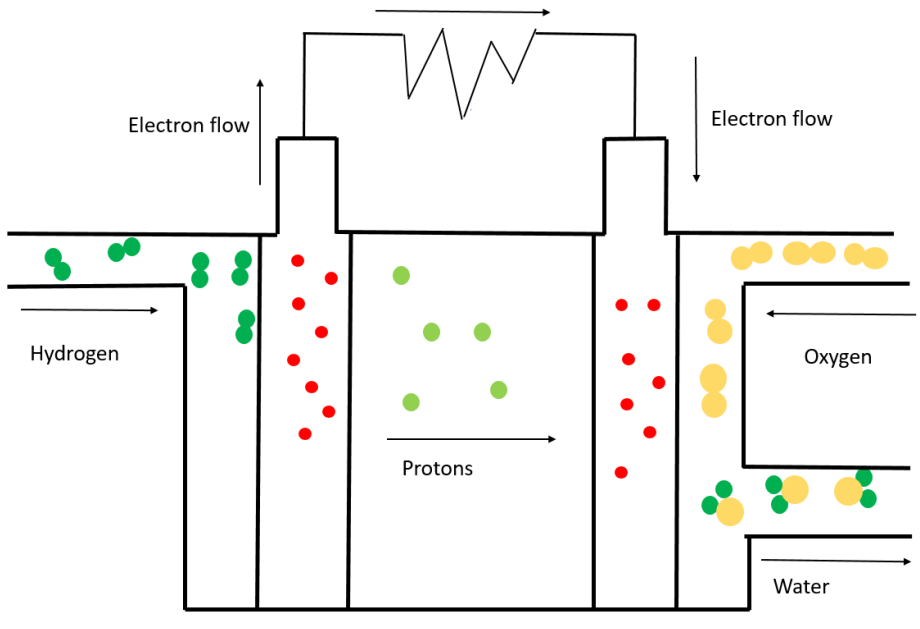

Figure 1.1: General scheme of a hydrogen fuel cell (adapted from Giorgi and Leccese, 2013).

Fuel cells are classified according to the electrolyte they use, which in turn determines their operating temperatures as shown in table 1.1. High temperature fuel cells operate at temperatures above 600°C, e.g. molten carbonate fuel cells (MCFCs) and solid oxide fuel cells (SOFCs) (Giorgi and Leccese, 2013). The high temperature operation allows for internal reforming of hydrocarbon fuels in the anode into H_2 and carbon in the presence of water (Giorgi and Leccese, 2013). This eliminates the need for pure H_2 as fuel. However, at these temperatures, most materials making up the components of the fuel cell degrade and high temperature fuel cells are not suitable for operations where a quick start-up is required.

Low temperature fuel cells operate at temperatures below 250°C. These include alkaline fuel cells (AFCs), proton exchange membrane fuel cells (PEMFCs), and phosphoric acid fuel cells (PAFCs) (Giorgi and Leccese, 2013). The low temperature operation of these fuel cells doesn't allow for internal reforming of hydrocarbons, hence an external source of H_2 is required (Lipman and Weber, 2018). However, the low temperatures allow for quick start-up and have less wear of the materials in the components of the fuel cells.

PEMFCs are the most widely used of the low temperature fuel cells because of their high power, current, and voltage density (Liu, Song & Subramani, 2010). Unlike AFCs and PAFCs, PEMFCs have a solid non-corrosive electrolyte which makes their mechanical design and handling easier. One of the major drawbacks of PEMFCs is their sensitivity to CO as it poisons the platinum catalyst on the anode. In several H_2 production processes, the reformate gas contains CO content above 1 % (Rodrigues et al., 1997). The amount of CO in H_2 gas has to be reduced to less than 10 ppm for use in fuel cells (Rodrigues et al., 1997).

Currently, the CO content present in reformate gas is reduced via water gas shift reaction which reduces the CO content to 0.5-1 vol.%. For further reduction of the CO content several techniques such as preferential oxidation of CO (CO-PROX), selective methanation of CO (CO-SMET), hydrogen selective membrane purification, and pressure swing adsorption can be used (Park, Lee and Lee, 2009). The major drawback of selective methanation of CO is the consumption of H_2 (desired product) during the reaction. For pressure swing adsorption it is the use of high pressure which results in design issues and high energy consumption. This makes CO-PROX a more cost-effective and efficient method for hydrogen purification for fuel cells when compared to other techniques.

CO-PROX requires a highly selective catalyst to minimize H_2 loss through its oxidation to form water and hydrogenation to form methane. Co_3O_4 is currently one of the most promising catalysts for CO-PROX because of its redox properties which are necessary for the MvK mechanism. However, at temperatures higher than 225 °C in H_2 rich streams, Co_3O_4 deactivates by the reduction of the active Co^{3+}/Co^{2+} species to Co^0. Co^0 is active for methanation (Zhao et al., 2012; Nyathi, 2016; Lukashuk et al., 2016; Khasu, 2017).

The study presented herein investigates the effect of promoters (FeO_x and MnO_x) on Co_3O_4/CeO_2 during CO-PROX.

Table 1.1: Types of fuel cells (Liu, Song & Subramani, 2010; Giorgi and Leccese, 2013; Lipman and Weber, 2018).

	MCFCs	**SOFCs**	**PEMFCs**	**AFCs**	**PAFCs**
Operating temperature (°C)	~650	800-1000	70-90	65-250	150-205
Electrolyte	Molten mixture of lithium and potassium carbonate	Ceramic	Proton conducting solid polymer	Potassium hydroxide	Phosphoric acid immobilized on silicon carbide
Fuel	Hydrocarbons	Hydrocarbons	H_2	H_2	H_2
Power released	<2.8MW	<3MW	<1MW	<400kW	<1MW
Advantages	-Internal reforming of hydrocarbons, no need for an external reformer -No expensive Pt catalyst -Tolerant to CO_2	-Internal reforming of hydrocarbons, no need for an external reformer -No expensive Pt catalyst -Tolerant to CO_2	-Quick start-up -Non-corrosive electrolyte -Tolerant to CO_2	-Quick start-up -No expensive Pt catalyst -Non-corrosive electrolyte	-Quick start-up -No expensive Pt catalyst -Tolerant to CO_2
Disadvantages	-Corrosive electrolyte -Long start-up -Degradation of components	-Long start-up -Degradation of components	-Pt catalyst can only tolerant CO amount less than 10ppm	-Intolerant to CO_2	-Corrosive electrolyte

2 Literature Review

2.1 Hydrogen production

i. Steam reforming

This is the most common production method because of its high efficiency of operation (Bičáková and Straka, 2010). Moreover, steam reforming operates at low temperatures compared to other processes such as partial oxidation and autothermal reforming. The common raw materials used in steam reforming are light hydrocarbons. At 500-900 °C, hydrocarbons are fed into steam, leading to the production of syngas (mixture of CO and H_2) and a low proportion of carbon dioxide as seen in equations 2.1 and 2.2. The catalysts commonly used during steam reforming are Ni and PGM-based. Overall, this method is known to generate high H_2: CO ratios (~3:1) (Holladay et al., 2009). Some of the drawbacks of steam reforming are the need for an external heat source and higher CO_2 emission when compared to other hydrogen production methods (Bičáková and Straka, 2010).

$$CH_4 + H_2O \rightleftharpoons CO + 3H_2 \qquad \Delta H^0_{298} = 206\ kJ/mol \qquad \text{Equation 2.1}$$

$$CH_4 + 2H_2O \rightleftharpoons CO_2 + 4H_2 \qquad \Delta H^0_{298} = 165\ kJ/mol \qquad \text{Equation 2.2}$$

ii. Partial oxidation

Without a catalyst, hydrocarbons are partially oxidized (combusted) with oxygen at temperatures of 1300-1500 °C as shown in equation 2.3 (Holladay et al., 2009). The addition of catalysts such as Ni-based catalysts does lower the operating temperatures (700-1000°C) (Bičáková and Straka, 2010). In this process, heat is provided by the controlled combustion of the hydrocarbons, leading to the production of H_2: CO ratios (2:1 or 1:1) that are lower than those obtained in steam reforming.

$$2CH_4 + O_2 \rightleftharpoons 2CO + 4H_2 \quad \Delta H^0_{298} = -36\ kJ/mol \qquad \text{Equation 2.3}$$

iii. Autothermal reforming

This process involves the addition of steam to a gasified hydrocarbon feedstock in the presence of oxygen, effectively combining steam reforming and partial oxidation processes as shown in equations 2.1 and 2.3 (Holladay et al., 2009). The heat released from the exothermic partial oxidation reaction is used to drive the steam reforming process, leading to a heat-integrated auto-sustainable process.

iv. Water-gas shift

The H_2 produced in the above reforming techniques contains a significant amount of CO (up to 10 vol.%), so these techniques are usually followed by the water gas shift (WGS) reaction. WGS reduces the CO content while increasing the H_2 yield as shown in equation 2.4. This reaction is moderately exothermic and reversible (Liu, Song & Subramani, 2010). At low temperatures, high conversions of CO to CO_2 are achieved. However, the reaction rate is kinetically limited. At high temperatures, the WGS reaction is kinetically fast but thermodynamically limited as the reverse water gas shift is favored (Liu, Song & Subramani, 2010). To overcome this limitation, a two-step configuration was developed. The first step is the high temperature WGS reaction, usually carried out at a temperature range of 310 -450 °C (Liu, Song & Subramani, 2010). Usually, a Fe_3O_4/Cr_2O_3 catalyst is used and the CO content is reduced from 10 vol.% to 3 vol.%. The second step is the low temperature WGS reaction, carried out in the temperature range of 180-250°C over a $Cu/ZnO/Al_2O_3$ catalyst (Liu, Song & Subramani, 2010). In this step, the CO concentration is reduced from 3 vol% to 0.5-1 vol.%.

$$CO + H_2O \rightleftharpoons CO_2 + H_2 \qquad \Delta H^0_{298} = -41\ kJ/mol$$ Equation 2.4

2.2 Hydrogen purification

Hydrogen produced *via* the water-gas shift process contains 0.5-1.0 % carbon monoxide (Rodrigues, 1997). In PEFMCs, carbon monoxide adsorbs strongly on the Pt electrocatalyst in the anode of the fuel cell, inhibiting the dissociation of hydrogen and the subsequent electron transfer (Rodrigues, 1997). This results in a net decrease in the performance of the fuel cell, creating the need to reduce the amount of carbon monoxide to less than 10 ppm (Rodrigues, 1997). Several techniques have been employed to reduce the carbon monoxide content, and these include the following:

2.2.1 Physical methods

i. Hydrogen selective membrane

The driving force for the separation of hydrogen from gases such as methane, carbon monoxide, and nitrogen is the concentration gradient or pressure across the membrane (Mishra and Prasad, 2011). Favorably, hydrogen has a high diffusion coefficient when compared to other molecules, which aids the separation in the membrane-based approach. The membranes allow H_2 to pass through while retaining all the other gasses.

Membranes are classified into three categories: metallic, polymeric, and inorganic. Polymeric membranes are of relatively low cost when compared to the other two classes, although notably, they possess low mechanical strength (Ockwig and Nenoff, 2007). Metallic membranes have an advantageously high hydrogen permeability of the three classes, with the major drawback of possibly experiencing hydrogen embrittlement at

low temperatures. Inorganic membranes have good thermal stability and are inert to poisonous gases (Ockwig and Nenoff, 2007). The disadvantage of inorganic membranes is the higher cost due to the thickness requirements needed to withstand pressure drop differences (Ockwig and Nenoff, 2007).

Metallic membranes are the most commercialized membranes due to their high H_2 selectivity (Liu, Song & Subramani, 2010). For polymeric membranes and inorganic membranes, the gas mixture has to pass through multiple membrane stages to achieve 99.9 % pure H_2 (Liu, Song & Subramani, 2010).

ii. Pressure swing adsorption

This strategy uses pressure to separate hydrogen from a mixture of gases by taking advantage of the differences in the molecular characteristics and affinity for an adsorbent material. The adsorbents usually used for H_2 purification are zeolites, alumina gel, silica gel, and activated carbon (Mishra and Prasad, 2011). There are four main steps during pressure swing adsorption: adsorption, depressurization, regeneration, and re-pressurization. Adsorption is carried out at high pressure until adsorption capacity is reached. In this step, the separation is caused by the differences in the binding strengths of gasses to the adsorbent material. Compared to molecules such CO, CO_2, and N_2, H_2 is highly volatile with low polarity (Sircar and Golden, 2000; Yang et al., 2008). Consequently, H_2 does not get adsorbed on the adsorbent while other molecules get adsorbed from a H_2 containing stream (Yang et al., 2008). The adsorbent is then regenerated by lowering the pressure this allows the adsorbed impurities to desorb. The pressure is then increased to start the cycle again (Sircar and Golden, 2000; Yang et al., 2008).

Majlan et al. (2009) reported the reduction of CO concentration in H_2/CO/CO_2 gas mixture from 4000 ppm to 1.4 ppm. The adsorbent used in this study was activated carbon. Most recently, Relvas et al. (2018) reduced CO concentration from 1 % CO to 0.17 ppm from a 70 % H_2, 25 % CO_2, 4 % CH_4, and 1 % CO gas feed. Activated carbon impregnated with $CuCl_2.2H_2O$ was used as an adsorbent.

The major drawbacks of pressure swing adsorption are the use of high pressure, the need to replace the adsorbent bed because of its deterioration over time, and the use of multiple adsorption columns operating under cyclic steady state using a series of sequential, non-isothermal, non-isobaric, and non-steady-state process steps (Liu, Song & Subramani, 2010).

2.2.2 Chemical methods

i. Selective catalytic methanation of CO

CO methanation is the conversion of CO to CH_4 over a hydrogenation catalyst as shown in equation 2.5. At the same time, the CO_2 methanation (undesired reaction) results in the consumption of the valuable H_2 (equation 2.6). At low temperatures, CO methanation is the dominant reaction due to the strong adsorption strength of CO on the catalyst surface (Dagle et al., 2007). At high temperatures, CO_2 methanation becomes more dominant as the CO adsorption strength weakens. Therefore, the hydrogenation catalyst used must be highly selective for the conversion of CO to CH_4 over a wide temperature range.

$$CO + 3H_2 \rightleftharpoons CH_4 + H_2O \qquad \Delta H^0_{298} = -206\ kJ/mol$$ Equation 2.5

$$CO_2 + 4H_2 \rightleftharpoons CH_4 + 2H_2O \qquad \Delta H^0_{298} = -165\ kJ/mol$$ Equation 2.6

Several catalysts have been studied for CO methanation, with Ni and Ru-based catalysts being the most active (Takenaka, Shimizu & Otsuka, 2003; Park, Lee and Lee, 2008). Ni/ZrO_2 and Ru/TiO_2 can decrease CO concentration via methanation from 0.5 % to 20ppm (Takenaka, Shimizu & Otsuka, 2003). In a study by Dagle et al. (2007), CO concentration was reduced from 0.9 % to less than 100 ppm using 3 wt.% Ru/Al_2O_3. Reduction of CO concentration to less than 10ppm while maintaining CO_2 conversion below 5 % using Ru/Al_2O_3 catalysts required multiple steps of methanation (Echigo and Tabata, 2004; Li et al., 2010). The first step is performed at temperatures between 250-300 °C over 0.4 wt.% Ru/Al_2O_3 catalyst (Li et al., 2010). In this step, CO concentration is reduced from 1 % to 0.1 %. The second step is performed at 150-185 °C over 0.8 wt.% Ru/Al_2O_3, reducing CO concentration to below 10 ppm (Li et al., 2010).

The main advantage of CO Methanation is that it requires no addition of oxygen. However, the main disadvantage is the consumption of hydrogen during the hydrogenation, making this process less effective for fuel cells (Dagle et al., 2007).

ii. Preferential oxidation of carbon monoxide (CO-PROX)

Preferential oxidation of carbon monoxide (CO-PROX) is the oxidation of CO to CO_2 in the presence of hydrogen (Oh and Sinkevitch, 1993). The targeted reaction during CO-PROX is equation 2.7, however, it competes with reaction 2.8 which is undesired because of the consumption of H_2 and O_2. The feed gas used for CO-PROX has 45-75 vol.% H_2, 15-25 vol.% CO_2, 0.5-1vol.% CO, up to 10 % H_2O, and N_2. Hence, there are other undesired side reactions (equations 2.4 and 2.5) that can occur in the course of the reaction.

$$2CO + O_2 \rightarrow 2CO_2 \qquad \Delta H^0_{298} = -283\ kJ/mol$$ Equation 2.7

$$2H_2 + O_2 \rightarrow 2H_2O \qquad \Delta H^0_{298} = -242\ kJ/mol$$ Equation 2.8

These reactions are influenced by temperature, amount of excess oxygen, and catalyst used. For Co_3O_4 based catalysts at temperatures below 175 °C, CO oxidation is the prominent reaction (Woods et al., 2010; Lukashuk et al., 2016; Khasu, 2016; Nyathi, 2016). Above 175 °C, CO_2 concentration decreases, while CO and H_2O concentrations increase as shown in figure 2.1 (Woods et al., 2010; Lukashuk et al., 2016; Nyathi, 2016). This indicates the onset of H_2 oxidation and reverse water gas shift. CO methanation commences at 275°C (Woods et al., 2010). However, Nyathi (2016) reported that CO methanation commences at 250 °C. The difference of onset temperature for CO methanation may be due to differences in catalyst characteristics (particle size distribution, shape, and support) and performance evaluation conditions.

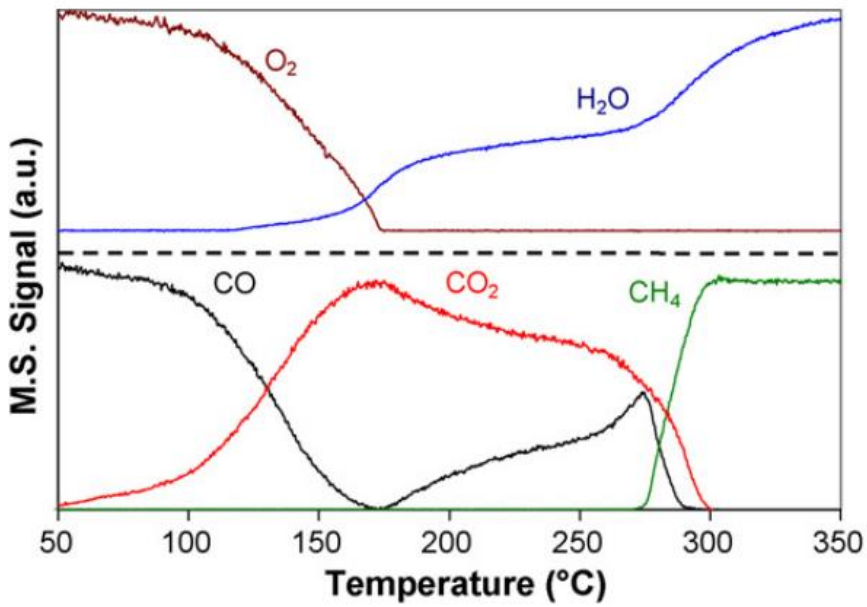

Figure 2.1: Temperature programmed CO-PROX reaction over CoO_x/CeO_2 in the presence of 1 % CO, 1 % O_2, 60 % H_2, and balance He (Woods et al., 2010).

2.3 Catalysts for CO-PROX

The requirements for an effective CO-PROX catalyst are (Mishra and Prasad, 2011):

- High activity for CO oxidation
  The high activity ensures that the CO concentration is reduced to levels below 10ppm
- High selectivity for O_2 to CO_2
  The high selectivity ensures reduced H_2 consumption.
- Good resistance to deactivation caused by CO_2 and H_2O
  The reformate gas from WGS contains 15-25 vol.% CO_2 and up to 10 % H_2O.

Mishra and Prasad (2011) categorized CO-PROX catalysts into Platinum Group Metal (PGM) catalysts, nano-gold-based catalysts, and base metal oxides.

2.3.1 Platinum Group Metals-based catalysts

Oh and Sinkevitch (1993) investigated CO-PROX activity as a function of temperature on noble metals (Pt, Pd, Rh, and Ru) supported on Al_2O_3. They showed that CO oxidation activity decreases in the order Ru/Al_2O_3> Rh/Al_2O_3> Pt/Al_2O_3> Pd/Al_2O_3 as shown in figure 2.2. Similar results were reported by Di et al. (2015) where the PGMs were supported on TiO_2. The catalysts exhibited maximum CO conversion at temperatures

below 200 °C. The decrease in CO conversion with increasing temperature was attributed to the onset of H_2 oxidation and the reverse water gas shift reaction.

The catalytic performance of Ru-based catalysts is dependent on factors like Ru precursor, pre-treatment, O_2/CO molar ratio, and support used. Ru catalysts prepared from $Ru(NO)(NO_3)_3.xH_2O$ precursor perform better than those from $Ru_3(CO)_{12}$ and $RuCl_3$, achieving CO concentration levels below 1ppm between 140-180 °C as shown in figure 2.2. The high activity of catalysts synthesized from $Ru(NO)(NO_3)_3.xH_2O$ was attributed to the high dispersion of these catalysts when compared to other precursors (Worner, Friedrich & Tamme, 2003). The poor performance of Ru catalysts prepared from chloride precursor was attributed to poisoning caused by residuals Cl^- ions (Chin, Alexeev & Amiridis, 2005) as well as sintering enhanced by the presence of Cl^- ions (Worner, Friedrich & Tamme, 2003).

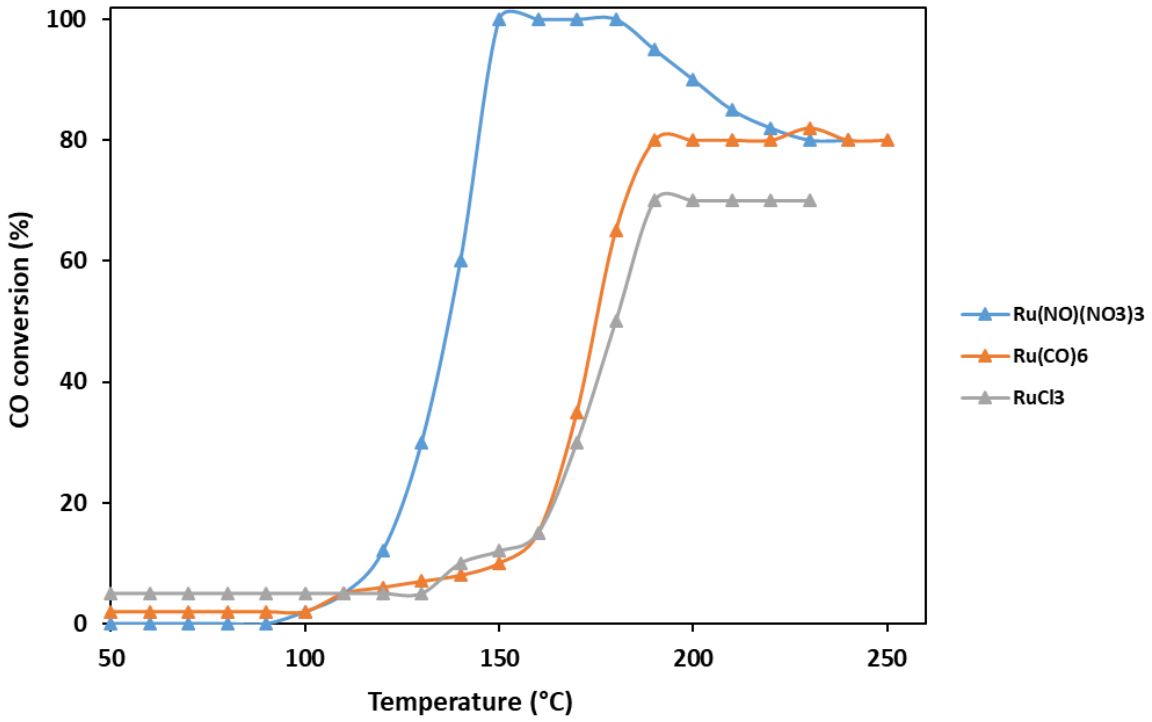

Figure 2.2: CO conversion as a function of temperature for Ru/Al_2O_3 catalyst prepared from different precursors (Chin, Alexeev & Amiridis, 2005).

Ru catalysts supported on yttria-stabilized zirconia (YSZ), ZrO_2, TiO_2, SiO_2, and Al_2O_3 were investigated for CO-PROX by (Kim et al., 2009). The CO-PROX activity decreased in the following order: Ru/YSZ >> Ru/SiO_2 > Ru/TiO_2 > Ru/ZrO_2 > Ru/Al_2O_3. Based on CO chemisorption, Ru/ZrO_2, Ru/Al_2O_3, and Ru/TiO_2 had the highest CO adsorption which limits the number of vacant sites for adsorption and dissociation of O_2. CO_2-TPD showed that Ru/YSZ had weak CO_2 adsorption compared to Ru/Al_2O_3 and Ru/ZrO_2. Chin, Alexeev, and Amiridis (2005) reported that the addition of 10 vol% CO_2 during CO-PROX decreases the activity of Ru/SiO_2. CO_2 adsorbs on active sites blocking the adsorption of CO and O_2 and also results in RWGS. Pre-treating catalysts can result in changes in the morphology of catalysts which affects metal-support interactions and electron donation between the metal and support (Di et al., 2015). Echigo and Tabata (2004) reported that Ru/Al_2O_3 pre-treated with 9.5 % H_2 in N_2 at 250 °C reduces CO concentration to less than 10ppm from 95 °C until 180 °C. While the catalyst not pre-treated achieved CO

concentration less than 10ppm at 160 °C. Therefore, the pre-treatment resulted in a wide optimal temperature range. Similar results were reported by Di et al. (2015) where Ru/TiO_2 was pre-treated in H_2 and H_2-CO. However, Echigo and Tabata (2004) reported that pre-treated Ru/Al_2O_3 had high CO methanation activity. When compared to Pt and Rh catalysts, Ru has a higher activity for methanation and RWGS during CO-PROX which makes it less favorable for CO-PROX (Han et al., 2003; Kim et al., 2009)

For noble metals supported on irreducible supports like Al_2O_3 and SiO_2, CO oxidation proceeds via the competitive Langmuir-Hinshelwood mechanism. In this mechanism O_2, H_2, and CO compete for active sites as shown in figure 2.3 (Kahlich, Gasteiger & Behm, 1997). At low temperatures, the CO adsorption strength is higher than that of O_2 and H_2, which inhibits the adsorption and dissociation of O_2 on the Pt surface (Grisel et al., 2002). At high temperatures, CO desorbs resulting in O_2 adsorption and an increase in CO oxidation.

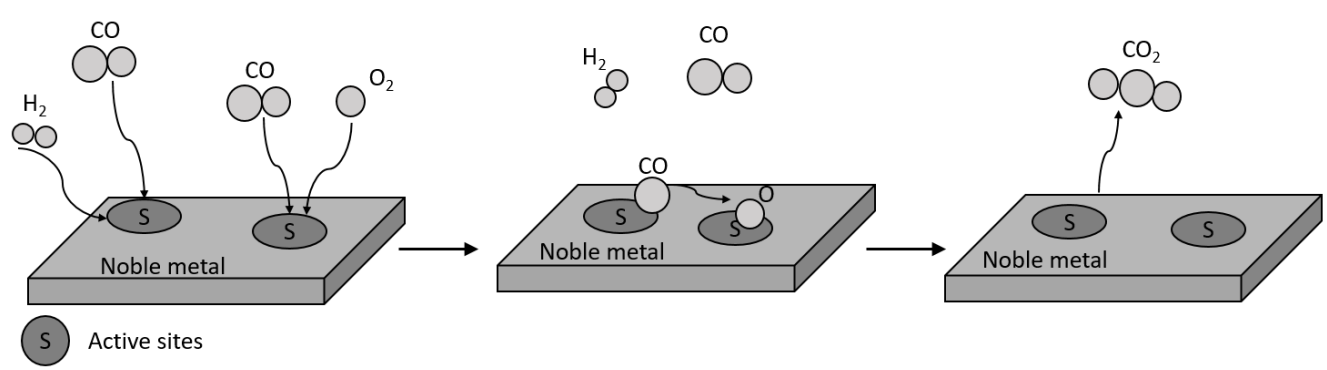

Figure 2.3: Competitive Langmuir-Hinshel Woods mechanism (Kahlich, Gasteiger & Behm, 1997).

Igarashi et al. (1997) investigated the activity and selectivity of 5 wt.% Pt supported on zeolites (type X, type A, and mordenite) and Al_2O_3. The zeolite-supported catalysts had the highest selectivity which was attributed to the concentration of CO and O_2 in the zeolite pores because of their high chemisorption properties compared to H_2 (Igarashi et al., 1997; Kotobuki et al., 2005). Therefore, CO and O_2 have a longer residence time in the pores of the zeolites and a higher chance of adsorption on Pt which results in selective oxidation of CO to CO_2. Wootsch et al. (2004) compared the activity and selectivity of Pt on different supports (Al_2O_3, CeO_2, ZrO_2, and $Ce_{0.68}Zr_{0.32}O_2$). The activity and selectivity decreased in the following order: $Pt/CeO_2 \approx Pt/Ce_{0.68}Zr_{0.32}O_2 > Pt/ZrO_2 > Pt/Al_2O_3$. When noble metals are supported on reducible supports like CeO_2, CO oxidation proceeds via the Mars-van Krevelen mechanism. In this mechanism the support provides its lattice oxygen for the oxidation of CO adsorbed on the metal as shown in figure 2.4 (Kang et al., 2003). This leads to an oxygen vacancy on the support which is filled by oxygen from the gas phase. The high CO methanation activity and low CO oxidation activity of PGMs limit their use for CO-PROX.

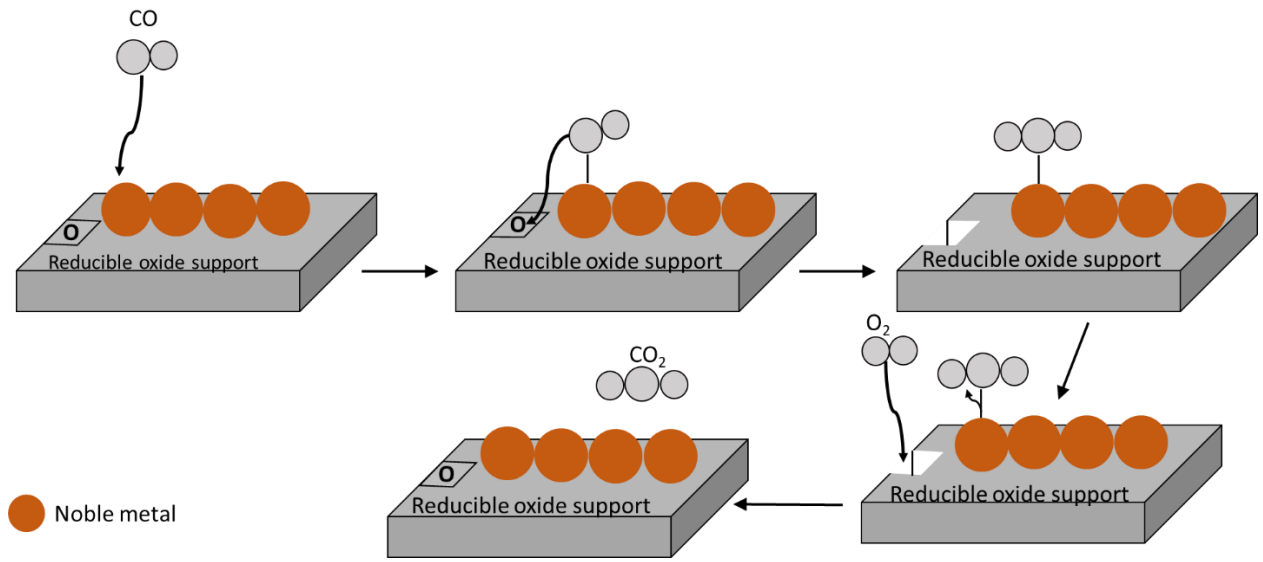

Figure 2.4: Mars-van Krevelen mechanism (Kang et al., 2003).

2.3.2 Gold-based catalysts

At low temperatures, Au catalysts are more active for CO oxidation than PGM-based catalysts and their O_2 to CO_2 selectivity is higher due to the limited capacity of Au to chemisorb and dissociate H_2 when compared to PGMs (Lakshmanan et al., 2014). The performance of Au catalyst is influenced by factors such as the particle size, oxidation state, and the support used.

Several studies have investigated the effect of support used for Au nanoparticles (Schubert et al., 2001; Ivanova et al., 2010; Beck et al., 2018). It was observed that the CO conversion and CO_2 selectivity decreased in the following order: $Au/CeO_2 > Au/Fe_2O_3 \approx Au/TiO_2 > Au/ZrO_2 > Au/Al_2O_3 \approx Au/ZnO_2$. Ceria supported Au achieved maximum CO conversion of 60 % while Au/Al_2O_3 and Au/ZnO achieved 20 % maximum conversion (Beck et al, 2018). The high activity of Au supported on reducible supports was attributed to the Mars-van Krevelen mechanism, where the supports provide O_2, and enhanced electronic interaction between Au and reducible support (Beck et al., 2018; Guczi, Beck & Frey, 2009).

For high activity, the particle size of supported Au should be in the range of 2-5nm regardless of the support (Quinet et al., 2009; Valden, Lai, and Goodman, 1998; Beck et al., 2018). Small Au nanoparticles have a high ratio of low coordinated sites (edges, kink, and corner sites) compared to large nanoparticles (> 9nm) (Quinet et al., 2009). Mavrikakis, Stoltze, and Norskov (2000) reported that for low Au coordinated sites the adsorption energy of CO and O_2 is lowered, resulting in the high activity of small nanoparticles. Additionally, Beck et al. (2018) reported that 2nm Au/CeO_2 had a higher ratio of Au^+/Au^0 than 7.8nm Au/CeO_2 from XPS. Hernandez et al. (2015) reported that a high ratio of Au^+ leads to an increase in activity.

Luengnaruemitchai, Osuwan, and Gulari (2014) investigated the effect of different preparation methods for 1% Au/CeO_2 for CO-PROX. The methods used were sol-gel, co-precipitation, and impregnation. The different methods resulted in Au particles of different sizes. For the impregnation and sol-gel method, the particle size was 30nm and for co-precipitation, it was less than 5nm. 1 % Au/CeO_2 catalyst prepared via co-precipitation had the highest activity, as shown in figure 2.5. The high activity of Au catalysts prepared via co-precipitation has been attributed to the small particle size of Au.

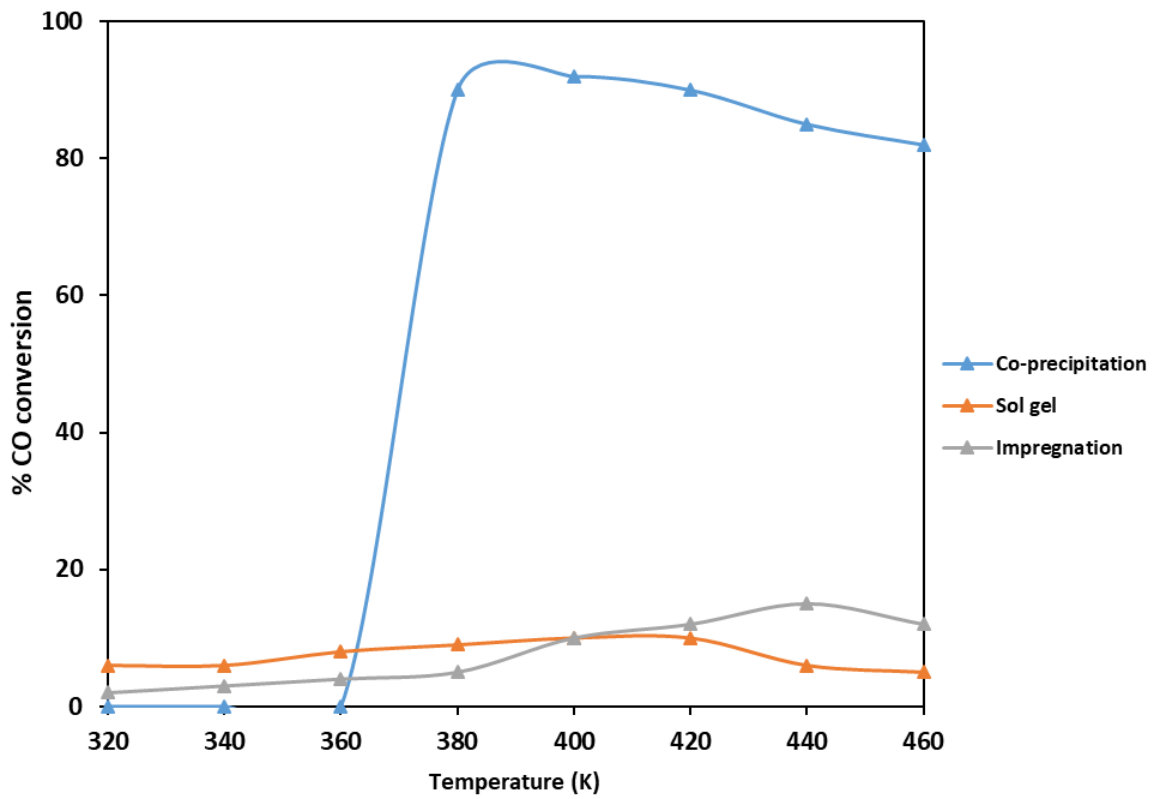

Figure 2.5: CO conversion as a function of temperature on 1 % Au/CeO_2 catalyst. Reaction conditions: 1 % CO, 1 % O_2, 2.6 % H_2O, 2 % CO_2, 40 % H_2, and helium (Luengnaruemitchai, Osuwan & Gulari, 2014).

The small nanoparticles Au nanoparticles have a strong interaction with the support (Luengnaruemitchai, Osuwan & Gulari, 2014; Lakshmanan et al., 2014). The strong metal-support interaction between Au and CeO_2 weakens the Ce-O bond in CeO_2 allowing high oxygen mobility hence higher CO oxidation. The presence of H_2O and CO_2 in the feed stream drastically decreases the activity of CO oxidation and selectivity due to the blockage of active sites. This limits the use of Au catalysts.

2.3.3 Base metal oxide catalysts

i. Copper-based catalysts

Due to the limited availability of noble metals, their cost, and poor selectivity, research is conducted on base metal oxide catalysts such as Co_3O_4 and CuO. For CO-PROX CuO/CeO_2 has been identified as the most active catalyst when compared to other CuO-based catalysts such as CuO/Fe_2O_3, CuO/ZrO_2, and CuO/SiO_2 (Kim and Ko, 2004; Ratnasamy et al., 2004). The superior performance of CuO/CeO_2 catalysts has been attributed to the synergistic interaction between Cu and Ce, which is a result of the redox interchange between Cu^{n+} and Ce^{n+} as shown in equation 2.9 (Gamarra, Belver & Ferna, 2007; Gamarra and Martinez-Arias, 2009; Wang et al., 2016).

$$Cu^{2+} + Ce^{3+} \leftrightarrow Cu^{+} + Ce^{4+} \qquad \text{Equation 2.9}$$

Gamarra and Martinez-Arias (2009) reported that CuO dispersed on CeO_2 becomes easily reducible and can effectively adsorb CO, while Cu^{2+} incorporated in the lattice causes defects on CeO_2 which increases O_2 mobility. The Mars-van Krevelen mechanism and identification of active sites for CuO/CeO_2 were described by (Gamarra et al., 2007, Gamarra and Martinez- Arias, 2009) as follows:

Step 1: Adsorption of CO on Cu^{2+}

$$CO_{(g)} + O - Cu^{2+} \rightarrow CO^{*} - O - Cu^{+} \qquad \text{Equation 2.10}$$

Step 2: CO_2 desorption and Cu^{1+} reduction

$$CO^{*} - O - Cu^{+} \rightarrow CO_{2(g)} + [V] - Cu^{0} \qquad \text{Equation 2.11}$$

Step 3: Filling of O vacancy and Cu^0 reoxidation (two suggested pathways)

(a) Direct mechanism

$$O_{2(g)} + 2([V] - Cu^{0}) \rightarrow 2(O - Cu^{2+}) \qquad \text{Equation 2.12}$$

(b) Synergistic mechanism (via CeO_2 in Cu-Ce contact)

$$Ce^{4+} - O + [V] - Cu^{0} \rightarrow Ce^{3+} - [V] + O - Cu^{+} \qquad \text{Equation 2.13a}$$

$$O_{2(g)} + 2(Ce^{3+} - [V]) \rightarrow 2(Ce^{4+} - O) \qquad \text{Equation 2.13b}$$

Where [V] is O_2 vacancy

In equations 2.10 and 2.11, CO adsorbs on Cu^{n+} sites (Cu^{+} or Cu^{2+}) and is oxidized by lattice oxygen forming CO_2 and a reduced Cu^{n+} site. A study by Fu et al. (1991) showed CO adsorption is stronger on Cu^{+} sites than Cu^{2+} sites, because of the balance between electron donation and back donation in $CO–Cu^{+}$. For CuO/CeO_2 catalyst, $CO–Cu^{+}$ carbonyls were detected in in-situ DRIFTS as a signal at ~ 2100 cm^{-1} immediately after the CO-PROX mixture was fed into the gas chamber (Gamarra and Martinez –Arias, 2009). The $CO–Cu^{+}$ band was observed at low temperatures, which shows that CuO reduction is more facile on CeO_2 support which is promoted by an interaction between CuO_x and CeO_2. Kozlov et al. (2002) reported that CuO_x reduces at 300 °C when supported on Al_2O_3, and at 150 °C when CeO_2 support is used. In step 3 the O_2 vacancies are then filled by O_2 from the gas mixture; two pathways have been suggested for this (equation 2.12 and equation 2.13).

The catalytic performance of CuO_x/CeO_2 is influenced by factors such as preparation method, loading of CuO_x, CO_2, and H_2O. Avgouropoulos et al. (2001) compared the activity of CuO/CeO_2 catalysts prepared via urea nitrate combustion, coprecipitation, impregnation, and a citrate-hydrothermal method. Urea nitrate combustion and citrate-hydrothermal catalysts had the highest performance. This was attributed to the formation of well-dispersed CuO_x interacting with CeO_2 and the absence of bulk CuO_x. The chelating method was reported by Liu, Zhou, and Zheng (2007) as an effective method when compared to the co-precipitation and citrate-hydrothermal method. The chelating method promotes the formation of defects in CeO_2 which enhances the Cu-Ce redox cycle. There is still no consensus on which preparation method is best.

Gamarra and Martinez-Arias (2009) distinguished three reaction regions during CO-PROX over CuO/CeO_2 as shown in figure 2.6, however, it should be noted that the temperatures at which they occur depend on the performance evaluation conditions. At temperatures below 105 °C (region

I), the CO oxidation reaction is the only reaction taking place. In the temperature range 105-202 °C (region II), the H_2 oxidation reaction begins, so it takes place concurrently with CO oxidation. In this region, both oxidation reactions compete so the CO_2 selectivity can be affected depending on the inlet O_2 stoichiometric excess. Above 202 °C (region III) H_2 oxidation becomes the more dominant reaction which leads to a decrease in CO oxidation.

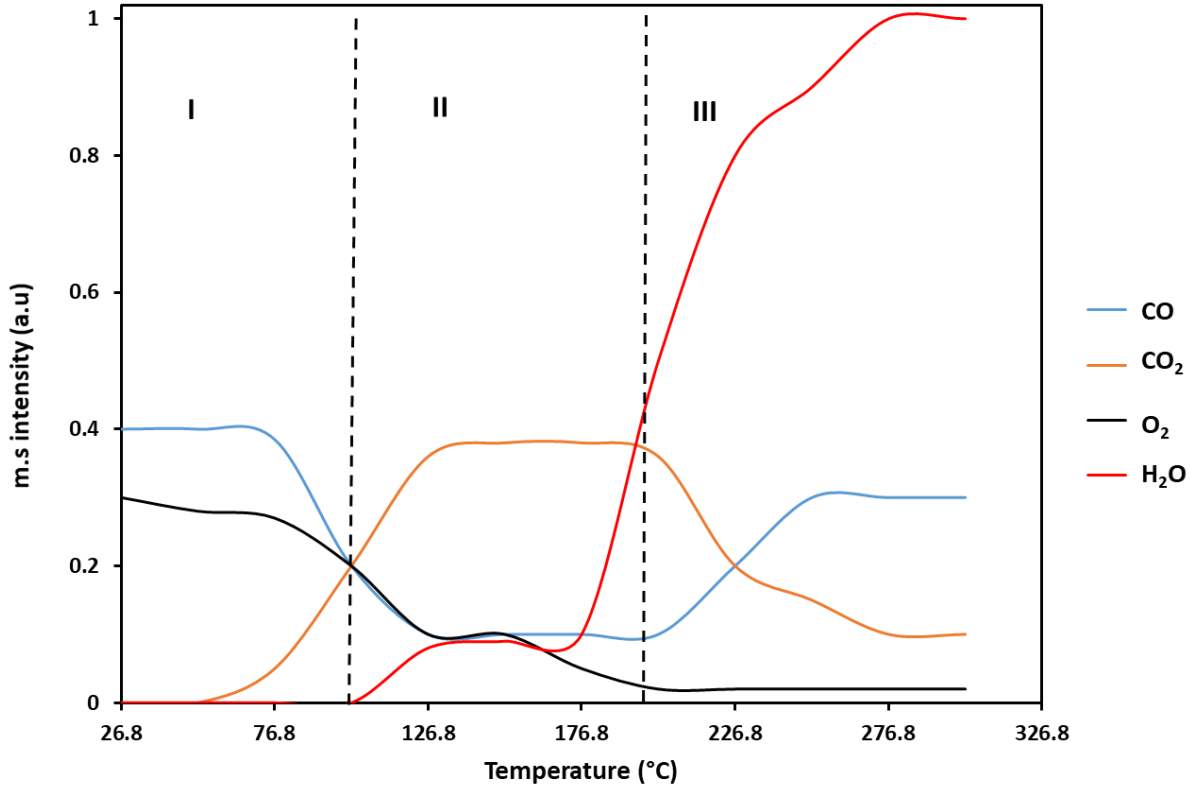

Figure 2.6: Reaction regions during CO-PROX over CuO/CeO_2 (Gamarra and Martinez-Arias, 2009).

The catalytic activity and selectivity of CuO-based catalysts are negatively affected by the presence of H_2O and CO_2 in the feed gas, which limits their use. Gamarra and Martinez-Arias (2009) performed operando-DRIFTS to investigate the deactivating effect of CO_2 and H_2O on CuO/CeO_2. In the absence of H_2O and CO_2, bands corresponding to hydroxyl species at 3712 cm^{-1}, carbonates at 1700 cm^{-1}, and Cu^+-carbonyls at 2115 cm^{-1} were observed. In the presence of 15 % CO_2 and 10 % H_2O, the intensity of the carbonate species increased while the intensity of the Cu^+-carbonyl decreased. The formation of carbonates and hydroxyl blocks the CuO-CeO_2 interfacial sites which inhibit oxygen mobility, thus limiting the redox cycle of these catalysts.

i. Cobalt-based catalysts

The other base metal oxide which has been investigated for use in CO-PROX is Co_3O_4. This is because Co_3O_4 has shown superior catalytic activity for CO oxidation in the absence of H_2 (Teng et al., 2011; Liu et al., 2013). Co_3O_4 has good redox properties, hence, it can fulfill the Mars-van Krevelen cycle (Omata et al., 1996; Jansson et al., 2000).

The catalytic performance of Co_3O_4-based catalysts during CO-PROX is influenced by the morphology, crystallite size, and the support used. Nyathi (2016) showed that the activity of CO oxidation increases with a decrease in Co_3O_4 crystallite size. The high activity was attributed to the facile reducibility of small crystallites when compared to larger crystallites (Fischer et al., 2014). However, in a similar study, Nyathi et al. (2017) reported that larger crystallites have higher activity. It was reported that smaller crystallites enter the pores of the supports, thus increasing the metal-support interactions and lowering reducibility (Nyathi et al., 2017).

The effect of Co_3O_4 morphology (spherical, nanocubes, nanosheets, nanobelts) was investigated by Khasu (2016). Spherical nanoparticles achieved the highest CO conversion (90.7 %) at 175 °C while nanobelts achieved 73.3 % at 200 °C followed by nanosheets which achieved 67.3 % at 175 °C. Nanocubes achieved 70 % CO conversion at 250 °C as shown in figure 2.7 (Khasu, 2017). Different morphologies expose different crystal planes which have different arrangements of surface atoms (Hu, Peng & Li, 2008). The effect of Co_3O_4 morphology (nanosheets, nanocubes, and nanobelts) was investigated during CH_4 combustion, which proceeds via the Mars-van Krevelen mechanism similarly > nanobelts > nanocubes. The high activity of Co_3O_4 nanosheets was attributed to the predominant exposure of high index {122} crystal planes, while for nanobelts and nanocubes the dominantly exposed crystal planes are low index planes {011} and {001}, respectively (Hu, Peng & Li, 2008; Su, Dou & Wang, 2014). Hu et al. (2010) investigated the effect of Co_3O_4 nanobelts and nanocubes during CO oxidation (in the absence of hydrogen). Co_3O_4 nanobelts had the best CO oxidation activity which was attributed to the facile reduction of these particles as the surface layer lattice oxygen in {011} planes is more easily activated than that found in {001} planes (Hu et al., 2010; Yong and Wenjie, 2012).

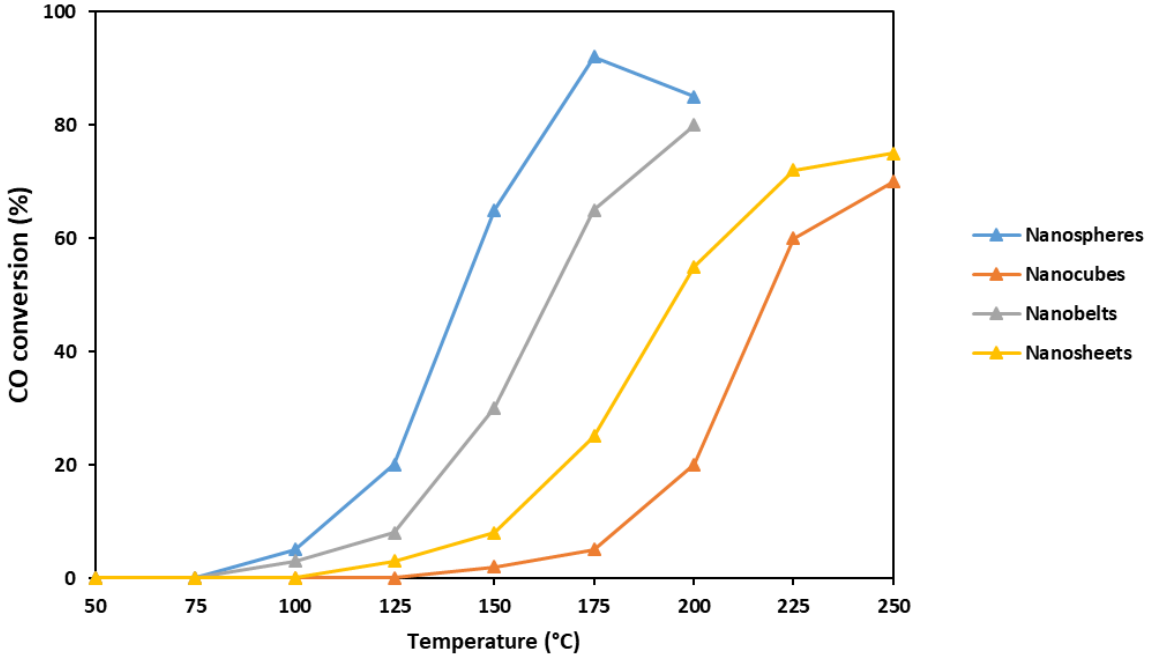

Figure 2.7: CO conversion of Co_3O_4 catalysts with different morphologies as a function of temperature (Khasu et al., 2017).

The effects of supports (ZrO_2, CeO_2, SiO_2, Al_2O_3, and TiO_2) on the activity of Co_3O_4 catalysts are reported by (Zhao, Yung & Ozkan, 2008; Zhao et al., 2011). Co_3O_4/CeO_2 and Co_3O_4/ZrO_2 have the highest activity for CO oxidation. H_2-TPR shows that for Co_3O_4/CeO_2 and Co_3O_4/ZrO_2 catalysts, the onset of reduction occurs at lower temperatures than for SiO_2, Al_2O_3 and TiO_2 supported Co_3O_4 (Zhao, Yung & Ozkan, 2008). Irreducible supports (SiO_2 and Al_2O_3) don't take part in the reaction and form stronger interactions with the Co_3O_4, which leads to poor reducibility

hence the low oxidation activity (Zhao, Yung & Ozkan, 2008). Facile reduction and re-oxidation of Co_3O_4 results in higher CO oxidation activity. During CO oxidation, CO adsorbs on cobalt species which releases its neighboring O^- ion to CO. This leads to partial reduction and oxygen vacancies in the CoO. Re-oxidation of the vacancies can be by O_2 co-fed in the gas mixture. Reduction to metallic cobalt has to be prevented because Co^0 is active for CO methanation (Broqvist et al., 2002; Konsolakis et al., 2015; Arango-Diaz et al., 2016; Huan et al., 2019).

Zhao et al. (2011) reported that 1.8 wt.% $Co_3O_4/Ce_{0.8}Zr_{0.2}O_2$ achieves 100 % CO conversion at 200 °C. The high activity of $Co_3O_4/Ce_{0.8}Zr_{0.2}O_2$ was attributed to the improved redox properties of the support. When CeO_2 is modified by the incorporation of other transition metals, defects form in its lattice (Trovarelli, 1999; Zhao et al., 2011; Zhao et al., 2012). Defects increase the oxygen mobility within the CeO_2 lattice and the ability of CeO_2 to change easily between oxidized and reduced state. This is affected by the type of dopant used, the ratio between the dopant and CeO_2, and the synthesis method of the mixed oxide (Trovarelli, 1999). Zhao et al. (2012) investigated the effect of incorporating different transition metals (Zr, Mn, Sn, Fe, and Ti) in the CeO_2 lattice. 20 wt.% $Co_3O_4/Ce_{0.85}Mn_{0.15}O_2$ had the highest activity and achieved 100 % CO conversion at 150 °C followed by $Co_3O_4/Ce_{0.8}Zr_{0.15}O_2$ which achieved 100 % conversion 165 °C. $Co_3O_4/Ce_{0.85}Ti_{0.15}O_2$ achieved a maximum of 95 % at 225 °C and $Co_3O_4/Ce_{0.85}Sn_{0.15}O_2$ a maximum of 92 % at 175 °C. H_2-TPR shows that the onset of reduction for $Co_3O_4/Ce_{0.85}Mn_{0.15}O_2$ and $Co_3O_4/Ce_{0.85}Zr_{0.15}O_2$ is 210 °C. While for $Co_3O_4/Ce_{0.85}Ti_{0.15}O_2$ the reduction onset temperature is 300 °C. The enhancement of oxygen mobility in $Ce_xZr_{1-x}O_2$ has been attributed to structural defects caused by the difference in ionic radius of Ce and Zr which causes a reduction in the unit cell (Trovarelli, 1999). While in $Co_3O_4/Ce_{0.85}Mn_{0.15}O_2$ increased oxygen mobility was attributed to the redox properties of MnO_x (Zhao et al., 2012)

The activity and selectivity of Co_3O_4 based catalysts are influenced by factors such as supports, particle size and, particle shape. CeO_2 and ZrO_2 based supports result in better catalytic performance because of their oxygen storage capacity and redox properties which are important for CO oxidation. The size of the supported Co_3O_4 plays a role in the metal-support interaction which affects the performance of Co_3O_4 based catalysts. Therefore, it is crucial to control the morphology of Co_3O_4.

2.4 Catalyst deactivation

The loss of catalytic activity and selectivity during the time on stream is a concern in catalytic processes because of the cost of catalyst replacement (Argyle and Bartholomew, 2015). Catalyst deactivation can be classified as inherent or operational. Operational deactivation is a result of conditions applied during a particular catalytic process that are not close to the ideal conditions, e.g. impurities in the feed (van Steen and Claeys, 2008). Inherent deactivation is due to changes in the catalyst formulation over time in ideal conditions. Some of the deactivation mechanisms include catalyst poisoning, sintering, gas-solid reactions, and fouling (Bartholomew, 2001; Forzatti and Lietti, 1999).

2.4.1 Poisoning

Poisoning is the strong chemisorption of reactants, products, or impurities on catalytically active sites. The poison blocks the active sites and may induce changes in the electronic or geometric structure (Bartholomew, 2001). The feed gas used during CO-PROX contains 10 % H_2O and 10-25 % CO_2, which have a negative effect on the CO oxidation activity of catalysts as shown in figure 2.8 (Zou, Dong & Lin, 2006; Wang et al., 2009; Bao et al., 2012). Nyathi et al. (2020) reported that in the absence of H_2O and CO_2, Co_3O_4 achieved a maximum CO conversion of 84.4 % at 175 °C during CO-PROX. In the presence of 10% H_2O, the maximum CO conversion achieved is 50.4 % at 225 °C. Additionally, the CO_2 selectivity

decreased with the addition of H_2O. While the addition of 10 % CO_2 did not affect the CO conversion and CO_2 selectivity. This might be due to the weaker surface adsorption of CO_2 when compared to H_2O (Nyathi et al., 2020). However, the addition of CO_2 did result in the reverse water gas shift reaction and CO_2 hydrogenation. When co-feeding both 10 % H_2O and CO_2, the maximum conversion decreased from 84.4 % to 72.1 %.

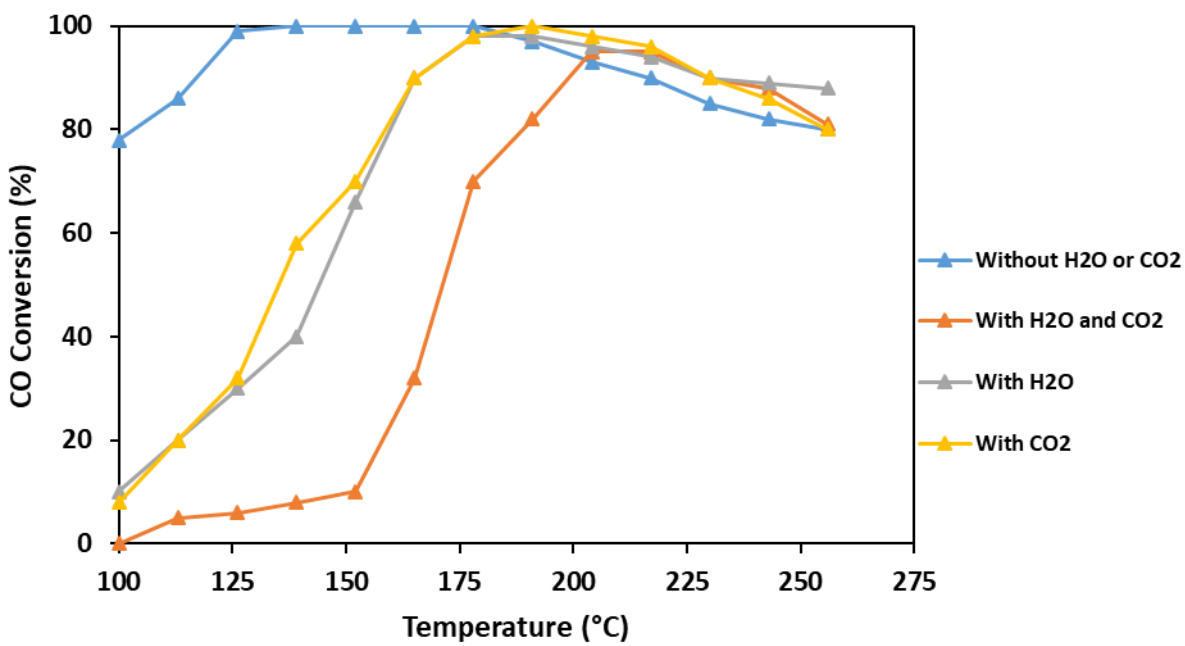

Figure 2.8: CO conversion during CO-PROX reaction over 35 wt.% Co_3O_4-CeO_2/AC in the presence/absence of H_2O and/or CO_2 in the feed. Reaction conditions: 1 % O_2, 1 % CO, 50 % H_2, 10 % H_2O, 10 % CO_2, and Ar balance. GHSV= 15000 ml $g^{-1}h^{-1}$(Bao et al., 2012).

2.4.2 Metal oxide reduction

The phase stability of catalysts is influenced by crystallite size, temperature, shape, and environment (reactants and products). In cobalt oxide-based catalysts the active species for CO oxidation is the Co^{3+}/Co^{2+} redox pair, while metallic Co is active for CO and CO_2 hydrogenation. Hence, reduction of Co_3O_4 to metallic Co decreases the CO oxidation activity and selectivity of the catalysts and results in the formation of CH_4. The formation of CH_4 is undesired because of the consumption of hydrogen.

It is reported in literature that reduction of Co_3O_4 occurs in two sequential steps as shown in equations 2.14 and 2.15 at temperatures between 150 °C and 500 °C (Sewell, van Steen & O'Connor, 1995).

$$Co_3O_4 + H_2 \rightarrow 3CoO + H_2O \qquad \text{Equation 2.14}$$

$$CoO + H_2 \rightarrow Co + H_2O \qquad \text{Equation 2.15}$$

The influence of reaction temperature and environment on the phase stability of cobalt oxide-based catalysts was investigated by (Lukashuk et al., 2016; Nyathi et al., 2020). Lukashuk et al. (2016) utilized operando XANES to study the composition of the bulk catalyst and operando NAP-XPS to study the surface phase composition. At temperatures between 50°C-250°C, the only phase present in the bulk was Co_3O_4; at 300°C Co_3O_4 was reduced to CoO (11.4%) and metallic Co (11%). At 350°C CoO (30%) and metallic Co (70%) were the only phases present (Lukashuk et al., 2016). In NAP- XPS the Co 2p spectra show that Co_3O_4 is the only phase present on the surface between 50°C-250°C (Lukashuk et al., 2016). Using in situ PXRD and magnetometer Nyathi et al. (2020) showed that the onset temperature for the reduction of Co_3O_4 is 200°C; CoO was stable between 200°C-300°C. Metallic Co was detected from 250°C which corresponds to the onset of CH_4. The effect of H_2O and CO_2 on phase stability was also investigated. The addition of 10% CO_2 did not affect the phase stability of the catalyst. The addition of 10% H_2O slightly delayed the formation of CoO and Co to higher temperatures and decreased the degree of reduction as shown in figure 2.9. H_2O is a stronger oxidizing agent than CO_2 hence it stabilizes the cobalt oxide phases.

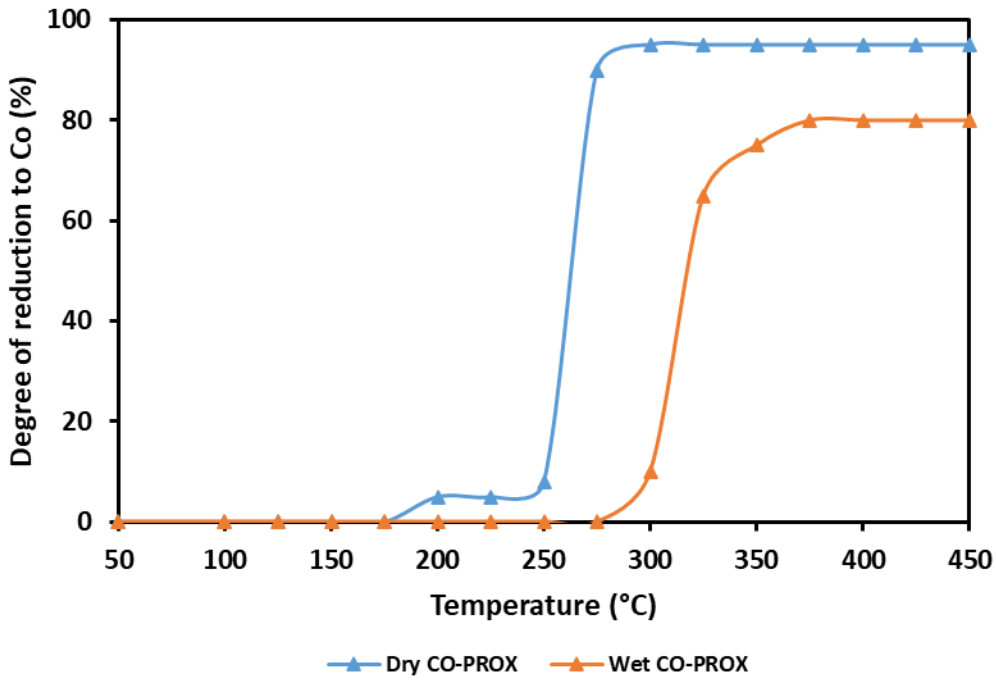

Figure 2.9: Degree of reduction of Co_3O_4 to metallic Co derived from the magnetometer during dry CO-PROX and wet CO-PROX (Nyathi et al., 2020).

Nyathi et al. (2016) investigated the effect of crystallite size (3-15 nm) on the phase stability of Co_3O_4/Al_2O_3. In situ, PXRD and magnetometer showed that the small crystallites (3 nm) start reducing at 180 °C while larger crystallites (15 nm) start to reduce at 200 °C. The degree of reduction at 350 °C for 3nm catalyst was 19.2 % while for 15 nm catalyst it was 45.7 %. H_2-TPR results showed for the 3 nm crystallites, the reduction occurred in the temperature range (180-450 °C). For the 15nm crystallites, the reduction temperature range was (200-300 °C). The small crystallites interact more strongly with the support which makes their reduction harder hence stabilizing the Co_3O_4 phase (Fischer, van Steen, and Claeys, 2011; Nyathi et al, 2016; Nyathi et al., 2017).

2.4.3 Sintering

Sintering is the loss of catalytic surface area due to the particle growth of the catalyst (Forzatti and Lietti, 1999; Bartholomew, 2001). The structural modification is thermally or chemically induced where the driving force is the need for small nanoparticles to reduce their surface energy (Forzatti and Lietti, 1999). The mechanisms for sintering are atomic migration and crystallite migration. During atomic migration, atoms escape from a crystallite and migrate to another metal crystallite while in crystallite migration the entire crystallite migrates over the support surface and coalesces with another crystallite (Bartholomew, 2001).

Sintering is dependent on temperature hence the melting point ($T_{melting}$) of the metal or oxide used plays a crucial role (Bartholomew, 2001). When the temperature is increased, lattice vibrations of the surface atoms increase until the Hütting temperature ($0.3T_{melting}$), where surface species migrate, while atoms in the bulk migrate at the Tamman temperature ($0.5T_{melting}$) (Forzatti and Lietti, 1999; Bartholomew, 2001).

2.5 Promoters

The activity, selectivity, and stability of catalysts can be improved by the addition of a promoter to the catalyst. Promoters are classified as electronic promoters and structural promoters (Hansen et al., 2001). Structural promoters facilitate the formation of catalysts with high surface area and dispersion, inhibit sintering, and stabilize the structure of the catalyst. (Hansen et al., 2001). Electronic promoters enhance the activity of the catalyst by chemical interaction which changes the chemical nature of the surface of the catalyst (Hansen et al., 2001).

It is hypothesized that adding an oxidizing promoter will stabilize Co_3O_4 as the temperature increases. The effect of the MnO_x promoter on Co_3O_4-CeO_2 was investigated by (Guo and Liu, 2008; Zhang et al., 2012; Zhao et al., 2012). The addition of MnO_x results in higher CO conversions, with promoted catalysts achieving 100% CO conversion from 60°C-180°C while for unpromoted catalysts the temperature window for 100% CO conversion was 80-160 °C (Guo and Liu, 2008). TEM and EDX showed that adding MnO_x increased the dispersion of Co_3O_4 (Guo and Liu, 2008; Zhang et al., 2012). XPS showed that the addition of MnO_x promoter to Co_3O_4-CeO_2 results in a higher Co^{3+}/Co^{2+} ratio. This is because of electron transfer between CoO_x and MnO_x which results in high CO oxidation activity (Guo and Liu, 2008; Zhang et al., 2012; Zhao et al., 2012). Mn can form oxides (MnO_x) with variable Mn oxidation states which can either co-exist or gradually become interconvertible (Imamura et al., 1996). MnO_x usually has a berthollide structure that contains labile lattice oxygen and good oxygen storage capacity (Ren et al., 2006). Due to its labile state, Mn has good redox properties making it capable of either being a reducing agent (Mn^{2+}- e^- →Mn^{3+}- e^- →Mn^{4+}) or an oxidizing agent (Mn^{4+}+ e^- →Mn^{3+}+ e^- →Mn^{2+}) (Ren et al., 2006). Thus, this redox interplay increases oxygen mobility thus increasing CO oxidation.

The effect of the Co: Mn atomic ratio was investigated by (Zhang et al., 2012; Zhao et al., 2012). The catalyst with an 8Co:1Mn atomic ratio was the best performing catalyst. O_2-TPD was performed to investigate the nature of oxygen species in Co_3O_4 during CO oxidation (Zhang et al., 2012; Zhao et al., 2012). The desorption peaks at temperatures lower than 350 ℃ are generally attributed to surface adsorbed oxygen species (α-oxygen species) which are weakly bound to the surface, while at higher temperatures the desorption peaks are attributed to lattice oxygen species (β-oxygen species) (Zhang et al., 2012; Liu et al., 2017). In unpromoted Co_3O_4 no peaks were observed at temperatures above 350 ℃, while for the MnO_x promoted catalyst both α-oxygen species (below 350 °C) and β-oxygen species (above 400 °C) were observed (Zhang et al., 2012). For catalysts with more MnO_x, the β-oxygen species peak shifted to higher temperatures (Liu et al., 2017). Thus, the presence of the correct amount of MnO_x is required to enhance the mobility of oxygen.

Zhao et al. (2012) investigated the effect of different promoters (MnO_x, FeO_x, CrO_x, and NiO_x) on $Co_3O_4/Ce_{0.85}Zr_{0.15}O_2$. MnO_x promoted catalyst was the most active catalyst followed by FeO_x promoted. The unpromoted catalyst performed better than the CrO_x and NiO_x promoted catalyst as shown in figure 2.10 below. Since the CrO_x and NiO_x-promoted catalysts achieved lower CO conversions they were not characterized in the study. Thus, an interpretation of their poor performance was not given. For O_2 to CO_2 selectivity all the promoted catalysts had a higher selectivity compared to $Co_3O_4/Ce_{0.85}Zr_{0.15}O_2$. CrO_x and FeO_x promoted had the highest selectivity, followed by MnO_x.

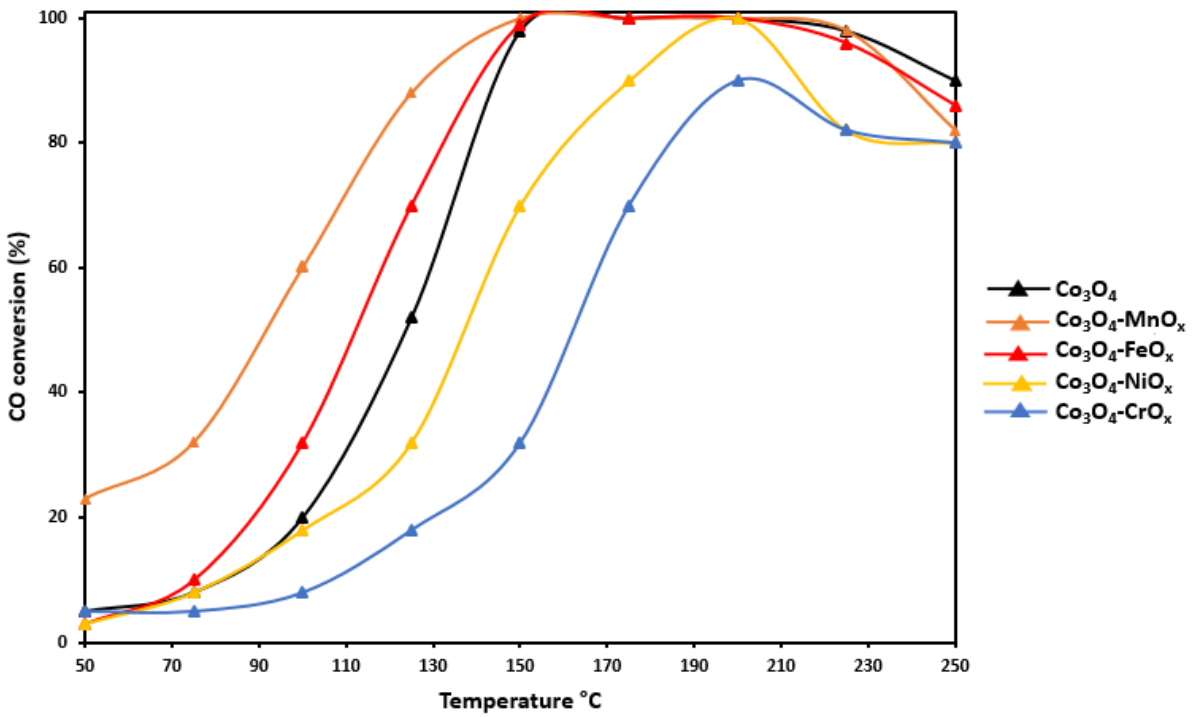

Figure 2.10: Effect of promoters on CO conversion during CO-PROX on 16 wt% Co_3O_4-$MO_x/Ce_{0.85}Zr_{0.15}O_2$ (M= Mn, Fe, Ni, or Cr). Reaction conditions: 1% CO, 1%O_2, 50% H_2, and Ar balance (Zhao et al., 2012).

2.6 Catalyst preparation

2.6.1 Impregnation

Impregnation is one of the most widely used methods for the preparation of supported catalysts. A metal precursor is dissolved in a solvent and then contacted with the support and subsequently dried (Campanati, Fornasari & Vaccari, 2003). There are two methods for contacting depending on the volume of the i.e. wet impregnation and incipient wetness impregnation. During incipient wet impregnation, the volume of the precursor solution is equal to the pore volume of the support (Campanati, Fornasari & Vaccari, 2003). When the solution is placed in contact with the support, it is drawn into the pores of the supports by capillary suction leaving no excess solution. During wet impregnation, an excess volume of the precursor solution is contacted with the support, after some time the excess solution is removed by drying. During impregnation, the distribution of nanoparticles is difficult to control which limits the use of this method.

2.6.2 Precipitation and Co-precipitation

Precipitation is the formation of insoluble solid from a solution upon the addition of a precipitation agent. During co-precipitation, two different metal ions form a solution that precipitates a homogenous bimetallic precipitate. The precipitate, which is usually a metal-hydroxide or carbonate depending on the nature of the precipitation agent, is then washed to remove any residual precipitation agent (Campanati, Fornasari & Vaccari, 2003). After washing, it is dried and calcined to decompose the carbonate or hydroxide into an oxide. The main advantages of co-precipitation include ease of composition control, operation at low temperatures, and homogeneity. However, the limitations include difficulty in controlling particle size distribution, trace impurities can also be precipitated and batch-to-batch reproducibility (Campanati, Fornasari & Vaccari, 2003).

2.6.3 Microemulsion

A microemulsion is a thermodynamically stable and isotropic system that consists of three components i.e. a polar phase, non-polar phase, and surfactant (Fischer, 2011). The phase present at a lower volume is the dispersed phase and forms droplets known as micelles, in the microemulsion (Fischer, 2011). In a system with a high volume of water the dispersed phase oil forms normal micelles (O/W). Conversely, for reverse micelles (W/O) water is the dispersed phase (Shiri, Henderson & Mucalo, 2019). The surfactant acts as an adsorbent at the boundary between the two immiscible phases and stabilizes the micelles (Nyathi, 2016). The main advantages of this method are; high degree of particle size and composition control (Shiri, Henderson & Mucalo, 2019). However, the requirement of large amounts of surfactants limits this method.

2.6.4 Solvothermal synthesis

Solvothermal synthesis is a non-aqueous, surfactant-free heat treatment using organics as a solvent and ligand (Pinna et al., 2005). In this method, a metal precursor such as metal acetate, metal halide, or metal alkoxide is dissolved in an organic solvent (e.g. alcohols, ketones, and amines). The solution is heated between 50-250 °C in an oil bath, autoclave, or microwave reactor while stirring (Deshmukh & Niederberger, 2017). After the heat treatment, the precipitate is separated from the reaction liquid by centrifugation. Pinna et al. (2005) outlined the reaction mechanism during the synthesis of Fe_3O_4 when using $Fe(acac)_3$ and benzyl alcohol. Benzyl alcohol can act as a nucleophile and attack one of the carbonyl groups of the acetylacetonate ligand (Niederberger & Garnweitner, 2006). Alcoholysis leads to benzyl acetate and an enolate ligand. Benzyl alcohol coordinates to the Fe center and is released as benzyl acetate leaving the Fe-bound hydroxyl group in a ligand exchange reaction. The enolate ligand from alcoholysis attacks the coordinated benzyl alkoxide and 4-phenyl-2-butanone is released. The Fe-bound hydroxyl group binds with another Fe center, representing the starting point of nanoparticle formation.

In a study by Yáñez-Vilar et al. (2009) MFe_2O_4 (M=Mn, Co, or Ni) nanoparticles were synthesized using solvothermal synthesis. The effect of different solvents (benzyl alcohol and hexanol) on the particle size was investigated. TEM showed that hexanol leads to slightly smaller (5.0 ± 0.8nm) ferrite nanoparticles than benzyl alcohol (7.4 ± 0.8nm), this was attributed to the higher Lewis basicity of hexanol which enhances the solvolysis of the metal precursor. Consequently, the nucleation reaction is faster and favored than the growth reaction which leads to smaller nanoparticles when using hexanol.

Most recently, Wolf et al. (2018) synthesized Co_3O_4 nanoparticles using cobalt acetate tetrahydrate and benzyl alcohol in the presence of ammonium hydroxide solution or ammonium acetate. In the presence of ammonium hydroxide, monodispersed single-phase Co_3O_4 nanoparticles were obtained, while in ammonium acetate single-phase CoO nanoparticles were obtained. The formation of CoO indicates an insufficient oxygen supply (Wolf et al., 2018). Niederberger and Garnweitner (2006) reported that the precursor and solvent are the sole providers of oxygen therefore, adding NH_4OH provides another oxygen source.

3 Research Approach

3.1 Background

Preferential oxidation of CO (CO-PROX) is one of the techniques used for the purification of hydrogen gas for use in fuel cells. Hydrogen gas produced by steam reforming contains 0.5-1 % CO (Holladay et al., 2009). CO is poisonous to the Pt/C catalyst in the anode of the fuel cell, hence, the amount of CO needs to be reduced to concentrations less than 10 ppm for fuel cells (Woods et al., 2010). Catalysts used for CO-PROX need to be active and selective for CO oxidation over a wide temperature range. Co_3O_4 is one of the most studied base metal oxides for CO-PROX, it has shown high CO oxidation activity and is a cheaper alternative for noble metals (Jansson et al., 2000).

For base metal oxides CO-PROX proceeds via the Mars-van Krevelen mechanism, where CO adsorbs on the metal oxide surface and extracts its lattice oxygen. This leaves an oxygen vacancy which is filled by oxygen from the gas phase (Gamarra et al., 2007). For Co_3O_4 the active species for CO-PROX is the Co^{3+}/Co^{2+} redox couple. However, in the presence of H_2 and increasing temperature Co_3O_4 reduces to lower oxidation states of cobalt. This leads to a decrease in the activity and selectivity of CO conversion to CO_2, and the formation of CH_4 (Nyathi, 2016; Khasu, 2016; Nyathi et al., 2020).

Currently, in literature, the addition of MnO_x and FeO_x promoters increases the catalytic performance of Co_3O_4 during CO-PROX. This is because of their good redox properties which result in good oxygen mobility during CO oxidation (Zhang et al., 2012; Zhao et al., 2012). To the best of our knowledge, catalytic performance evaluations of MnO_x and FeO_x promoted Co_3O_4 based catalysts are performed at temperatures below 250 °C (Zhang et al., 2012; Zhao et al., 2012). In the current study, we want to investigate the performance and stability of MnO_x and FeO_x promoted Co_3O_4 at temperatures above 250 °C. The stability and high activity of Co_3O_4 at high temperatures for CO-PROX is advantageous for industrial application as it eliminates the need for cooling processes after WGS to accommodate the phase stability of the catalyst. In the current study, we investigate the performance and stability of MnO_x and FeO_x promoted Co_3O_4/CeO_2 at temperatures of up to 450 °C. The optimum molar ratio of Co: Mn has been reported to be 8Co:1Mn (Zhang et al., 2012; Zhao et al., 2012). However, optimum ratio of Co: Fe has not been investigated. In the current study, different molar ratios of Co: Fe were investigated to deteremine the optimum Co: Fe ratio.

3.2. Hypothesis

The addition of a promoter (MnO_x or FeO_x) to Co_3O_4/CeO_2 catalyst will increase the activity and stability of the catalyst at temperature above 250 °C by preventing the phase change of Co_3O_4 to Co. This will result in the onset temperature for CO methanation increasing. This is because there is an electron transfer between Co_3O_4 and the promoters because of the redox properties of the promoters.

3.2 Research objectives

i. Synthesis monodispersed Co_3O_4 nanoparticles
ii. Prepare and characterize Co_3O_4/CeO_2 catalysts promoted with MnO_x or FeO_x while varying the Co: promoter ratio
iii. Evaluate the catalytic performance of the catalysts from 50 to 450 °C

iv. Investigate the effect of the promoters on the stability of Co_3O_4 during CO-PROX

3.4. Key questions

i. What is the effect of promoters on the reduction and oxidation temperature of Co_3O_4/CeO_2
ii. What is the effect of the promoters on the CO activation temperature of Co_3O_4/CeO_2?
iii. What is the optimum molar ratio between the promoter and Co_3O_4?
iv. How do the promoters affect the catalytic performance and stability of Co_3O_4/CeO_2?

3.3 Research Approach

Co_3O_4 nanoparticles were synthesized using a solvothermal method which results in nanoparticles with narrow particle size distribution (Wolf et al., 2018). To promote and support the nanoparticles, wet impregnation via ultrasonication was used. The properties of the catalysts were studied using various Techniques: Transmission Electron microscopy, Elemental mapping, Powder X-ray Diffraction, Temperature programmed reactions (TPR/TPO), CO-Temperature programmed reaction, and Inductively Coupled Plasma-Optical Emission Spectroscopy. The performance of the catalysts was evaluated in a fixed bed reactor coupled with a Micro Gas Chromatograph.

4 Research Approach

4.1 Chemicals

Table 4.1: List of chemicals used

Chemical	Purity	Supplier
Acetone	99.0%	Kimix
Benzyl Alcohol	≥ 99.0%	Sigma Aldrich
Cobalt (II) Acetate Tetrahydrate	Reagent grade	Sigma Aldrich
Ethanol	99.0%	Kimix
Iso-propanol	99.0%	Kimix
Ammonia Solution	25.0 wt.%	Kimix
Iron (III) nitrate nonahydrate	98.0%	Sigma Aldrich
Manganese (II) nitrate hydrate	98.0%	Sigma Aldrich

4.2 Synthesis of Co_3O_4 nanoparticles

Monodispersed nanoparticles were synthesized via the solvothermal method (Wolf, Fischer, and Claeys, 2018). 3.2 g of the cobalt (II) acetate tetrahydrate precursor was dissolved in 140 ml of benzyl alcohol under magnetic stirring at 450 rpm in a 600 ml beaker for two hours. Upon dissolution of the cobalt (II) acetate precursor, 140 ml of a 25 wt.% aqueous ammonium hydroxide (NH_4OH) solution was added dropwise while stirring. A change of color, from pink to a brown emulsion, was observed. The emulsion was transferred into a 500 ml round bottom flask. For thermal treatment, the round bottom flask was transferred to a rotary evaporator preheated at 165 °C. The pressure was set to 900 mbar and the flask with the emulsion was subjected to a rotation speed of 150 rpm for three hours.

The emulsion was cooled to room temperature to quench the reaction and then transferred to a 1L Schott bottle where its volume was tripled by adding isopropanol. Tripling the volume with isopropanol allows the dissolution of organics and unreacted contents for facile washing of the nanoparticles. The suspension was then centrifuged at 7000 rpm for one hour with the supernatant discarded for recovery of the settled nanoparticles. The recovered nanoparticles were re-dispersed in 400ml of ethanol and centrifuged. After dispersion, the nanoparticles were washed three times with acetone. The nanoparticles were dried in a fume hood under ambient conditions for 12 hours.

4.3 Supporting and promoting Co_3O_4

The nanoparticles were promoted and anchored on the support using wet impregnation via ultrasonication to improve the dispersion of the active metal oxide as outlined by Wolf et al. (2018). Two suspensions were made, in suspension (I) specific amounts of Co_3O_4 nanoparticles and promoter precursor (Fe (III) nitrate nonahydrate or Mn (II) nitrate hydrate) were dispersed in 300 ml of ethanol. In suspension (II) 2.7g of ceria was dispersed in 300 ml of ethanol. The suspensions were sonicated for two hours. Suspension (I) was added dropwise to suspension (II) and this was further sonicated for two hours. The suspension was transferred into a rotary evaporator to remove ethanol at 300 mbar, 200 rpm, and 80 °C. The catalysts were dried in a fume hood for 12 hours and further dried in a drying oven at 120 °C for 8 hours. Lastly, the dried catalysts were calcined at 450 °C while flowing air for four hours at a heating rate of 5 °C/min.

Table 4.2: Mass of cobalt nanoparticles and promoter precursors.

Catalyst name	**Catalyst**	**Mass of promoter precursor (g)**	**Mass of Co_3O_4 nanoparticles (g)**	**Co: promoter molar ratio**
Unpromoted	Co_3O_4/CeO_2	N/A	0.30	N/A
0.3 wt.% MnO_x	Co_3O_4-MnO_x/CeO_2	0.08	0.30	10:1
0.5 wt.% MnO_x	Co_3O_4-MnO_x/CeO_2	0.07	0.30	8:1
1.0 wt.% MnO_x	Co_3O_4-MnO_x/CeO_2	0.10	0.30	6:1
0.3 wt.% FeO_x	Co_3O_4-FeO_x/CeO_2	0.15	0.30	10:1
0.5 wt.% FeO_x	Co_3O_4-FeO_x/CeO_2	0.19	0.30	8:1
1.0 wt.% FeO_x	Co_3O_4-FeO_x/CeO_2	0.20	0.30	6:1

4.4 Ex-situ characterization of catalysts

4.4.1 Transmission electron microscopy (TEM)

TEM was used to determine the size distribution and morphology of the fresh and used catalysts. An FEI T20 Transmission Electron Microscope equipped with a LaB_6 field emission gun and operated at 200kv was used. The microscope is fitted with a 2k x 2k Gatan camera. For sample preparation, a small amount of the catalyst was dispersed in ethanol. Several drops of the suspension were deposited onto a carbon-coated copper grid and dried in the air before analysis. To determine the average particle size and particle size distribution the micrographs were analyzed using

open-source ImageJ software. The length of 300 nanoparticles was measured to calculate the number and volume-based average particle sizes together with the standard deviations were calculated using equations 4.1 to 4.4 (Nyathi, 2016). The volume-based average particle size was compared with the crystallite size obtained by Rietveld refinement (see section 4.3.3).

$$Number\ based\ average\ particle\ size\ (\bar{l}_n) = \frac{\sum_{i=1}^{N} n_i l_i}{N} \qquad \text{Equation 4.1}$$

$$Volume\ based\ average\ particle\ size\ (\bar{l}_v) = \frac{\sum_{i=1}^{N} n_i {l_i}^4}{\sum_{i=1}^{N} n_i {l_i}^3} \qquad \text{Equation 4.2}$$

$$Number\ based\ standard\ deviation = \sqrt{\frac{\sum_{i=1}^{N} n_i\,(l_i - \bar{l}_n)^2}{N-1}} \qquad \text{Equation 4.3}$$

$$Volume\ based\ standard\ deviation = \sqrt{\frac{\sum_{i=1}^{N} n_i\,{l_i}^3 (l_i - \bar{l}_v)^2}{\frac{N-1}{N}\sum_{i=1}^{N} n_i {l_i}^3}} \qquad \text{Equation 4.4}$$

The variable l_i is the length of the nanoparticle i, n_i is the number of nanoparticles of size l_i and N is the total number of nanoparticles counted.

4.4.2 Scanning Transmission Electron Microscopy coupled with Energy Dispersive Spectroscopy

STEM and elemental mapping were used to determine the elemental distribution of the fresh and used catalysts. The imaging and elemental mapping were performed at the Norwegian Centre of Transmission Electron Microscopy. An FEI Titan G2 Transmission Electron Microscope operating at 200kv was used. The microscope is fitted with a DCOR Cs probe corrector and six STEM detectors. The detectors are for Bright field (BF), Annular Bright field (ABF), Annular dark-field (ADF), and High-Angle Annular Dark Field (HAADF) imaging. For elemental mapping, it has four Super-X Bruker energy dispersive detectors and a Velox software package. For sample preparation, a small amount of the catalyst was dispersed in ethanol. A few drops of the suspension were deposited onto a QUANTIFOIL® TEM grid.

4.4.3 X-ray diffraction (XRD)

The crystalline phases present in the fresh and used catalysts were determined using a Bruker D8 Advance X-ray diffractometer. The diffractometer operates at 35 kV and 40 mA. It is equipped with a cobalt source (λ = 1.78897 Å) and a VANTEC position-sensitive detector. A 2θ scan range of $20° < 2\theta < 130°$ (step size: 0.01° and time per scan was 0.3 seconds) was chosen. The phases present in the samples were identified by relating the intensities and positions of the diffraction lines of the samples with the standards stored in the International Centre for Diffraction Database (ICDD PDF2 2006 database).

Rietveld refinement of the XRD patterns using TOPAS 5 software was used to determine the cobalt phases present and their weight fractions, the unit cell parameters, and the volume-based average crystallite size. In Rietveld refinement, the XRD patterns of the catalysts are modeled based on known reference XRD patterns (Fischer, 2011).

4.4.4 Temperature-programmed reactions

The reduction and re-oxidation behavior of the catalysts was studied by a TPR-TPO cycle in Micrometrics AutoChem2920. 100 mg of catalyst was placed between two quartz wool pieces in a U-shaped quartz reactor. The sample was dried by flowing Ar (flow rate: 10 ml (NTP)/min) while heating to 120 °C (heating rate: 10 °C/min) and held for one hour at 120 °C. The temperature was then cooled to 60 °C and the gas was changed to 5 % H_2 in Ar (flow rate: 50 ml (NTP)/min). Hydrogen consumption was monitored using a thermal conductivity detector (TCD) during a temperature ramp to 950 °C (heating rate 5°C/min). The sample remained at 950 °C for one hour before being cooled down to 50 °C in Ar (flow rate: 10 ml (NTP)/min). To perform TPO the gas was changed to 5 % O_2 in He (flow rate: 50 ml (NTP)/min) while heating up from 50 to 950 °C and recording oxygen consumption. The sample remained at 950 °C for one hour before cooling down to 50 °C in Ar.

The hydrogen consumption per peak area was calibrated using Ag_2O on the Autochem 2920. The calibration gives the H_2 consumption as a function of the peak area shown in equation 4.5 (Petersen, 2018).

$$H_2\ consumption = 2.8 \times 10^{-5} + peak\ area(tcd\ min) \times 2.3 \times 10^{-4} \quad \text{Equation 4.5}$$

The complete reduction of one mole of Co_3O_4 requires 2 moles of H_2 and proceeds via equations 4.6 and 4.7.

$$Co_3O_4 + H_2 \rightarrow 3CoO + H_2O \quad \text{Equation 4.6}$$

$$CoO + H_2 \rightarrow Co + H_2O \quad \text{Equation 4.7}$$

The degree of reduction of each catalyst was calculated using equation 4.8.

$$\text{Degree of reduction} = \frac{H_{2,consumed}}{4N_{Co3O4}} \times 100 \quad \text{Equation 4.8}$$

Peak deconvolution of the hydrogen and oxygen consumption profiles was performed on Origin software. The peaks were fitted using a built-in standard pseudo-Voigt function (OriginLab Cooperation, 2003).

4.4.5 Inductively Coupled Plasma Optical Emission Spectroscopy (ICP-OES)

ICP-OES was used to determine the loading of cobalt and the promoters on the ceria support. The samples were digested in 3 ml of HCl, 3 ml of HF, and a few drops of HNO_3 in a reactor containing bi-distilled water. The mixture was then heated to 130 °C, stirred for about an hour, and then cooled under a jet of water. To make sure that there is no residue, 60ml of H_3BO_3 was added under stirring. The solution was subsequently filtered and transferred to a volumetric flask. The solution was injected into a Varian OES 730 Series spectrometer.

4.5 Catalytic Performance Evaluation

4.5.1 Reactor isothermal zone

The reactor tube was packed with SiC and mounted into the rig. The temperature was set at 200 °C while flowing N_2. The reactor tube has a thermowell along its center as shown in figure 4.1. The thermowell is fitted with a moveable J-type thermocouple. The temperature was measured for every 10mm length of the reactor to determine the isothermal zone.

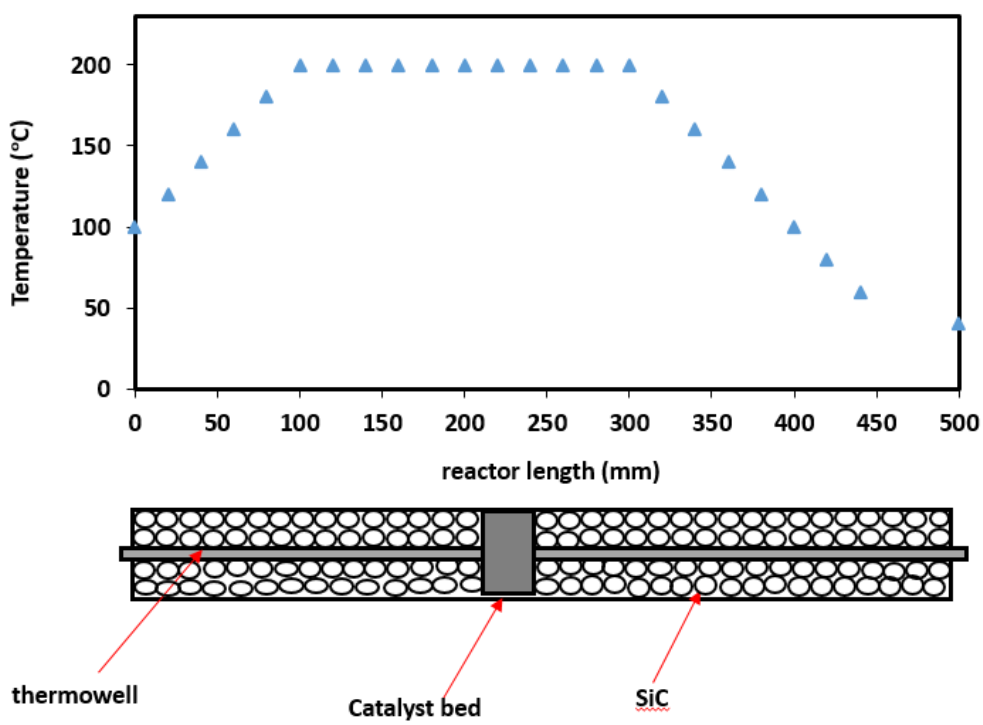

Figure 4.1: Temperature profile at 200 °C.

4.5.2 Calibrations

To determine the relative amounts of the gases from the reactor outlet, online gas chromatography was conducted using an Agilent CP4900 micro-GC fitted with a TCD. The micro-GC has three columns for gas separation. Column 1 is a 20 m molecular sieve 5Å PLOT. This column separates H_2, and its carrier gas is Ar. Column 2 is a 10 m molecular sieve 5Å PLOT. The carrier gas for this column is H_2 , the gasses it separates O_2, N_2, CH_4, and CO. Lastly, column 3 which is a 1 m COX heated injector separates CO_2 and its carrier gas is H_2. The parameters of the GC are shown in table 4.3.

The reactor effluent was sampled every six minutes and Galaxie software was used to determine the peak areas of each of the gases which were related to their molar flow rates by their respective response calibration factors. The micro-GC was calibrated using two AFROX gas cylinders. One containing 21 % O_2 and 79 % N_2 and another 5.1 % N_2, 10.2 % Ar, 10.2 % CO_2, 14.3 % CH_4, 20 % CO, and 40.2 % H_2. The response factors

of the gasses were calculated using N_2 as a reference gas since it does not get consumed during the reaction. The molar flow rates of each gas were calculated as shown in equations 4.9 and 4.10 below.

$$F_i = \frac{n_{N_2} \times A_i}{n_i \times A_{N_2}} \qquad \text{Equation 4.9}$$

$$n_{i_{out}} = \frac{n_{N_2} \times A_i}{F_i \times A_{N_2}} \qquad \text{Equation 4.10}$$

Where F_i is the response factor of the gas component i with reference to N_2. A_{N_2} is the peak area of N_2 and A_i is the peak area of gas component i, n_{N_2} is the molar flow rate of N_2 and n_i is the molar flow rate of gas component i.

Table 4.3: Micro GC parameters.

Parameters	**Channel 1**	**Channel 2**	**Channel 3**
Column type	Molecular sieve 5Å PLOT	Molecular sieve 5Å PLOT	COX
Column length (m)	10	20	1
Column temperature (°C)	50	60	50
Column pressure (kPa)	150	150	150
Carrier gas	Ar	H_2	H_2
Gases analysed	H_2	O_2, CO, CH_4, N_2	CO_2
Detector type	TCD	TCD	TCD
Injection temperature (°C)	50	60	50
Duration (min)	6	6	6

The percentage of CO conversion ($\mathbf{X_{CO}}$), CO_2 yield ($\mathbf{Y_{CO2}}$), CH_4 yield ($\mathbf{Y_{CH4}}$), and O_2 to CO_2 selectivity ($S_{CO_2}^{O_2}$) were calculated using the following equations:

$$X_{CO}(\%) = \frac{n_{CO_{in}} - n_{CO,out}}{n_{CO_{in}}} \times 100$$ Equation 4.11

$$Y_{CO_2}(\%) = \frac{n_{CO_{in}} - n_{CO,out} - n_{CH_4,out}}{n_{CO_{in}}} \times 100 = \frac{n_{CO_{2,out}}}{n_{CO_{in}}} \times 100$$ Equation 4.12

$$Y_{CH_4}(\%) = \frac{n_{CO_{in}} - n_{CO,out} - n_{CO_{2,out}}}{n_{CO_{in}}} \times 100 = \frac{n_{CH_{4,out}}}{n_{CO_{in}}} \times 100$$ Equation 4.13

$$S_{CO_2}^{O_2}(\%) = \frac{n_{co,in} - n_{CO_{out}} - n_{CH_{4_{out}}}}{2\times(n_{O_2 in} - n_{O2_{out}})} \times 100 = \frac{n_{CO_{2,out}}}{2\times(n_{O_{2,in}} - n_{O_{2,out}})} \times 100$$ Equation 4.14

4.5.3 Reactor set up

The catalytic performance evaluations of the catalysts were performed in a custom-built fixed bed reactor. The rig setup shown in figure 4.2 consists of two stainless steel reactor tubes, which have 19 mm outer diameter and are 500 mm long. However, for this study one reactor was used. The reactors tubes were mounted in a four-zone metal heating block. The temperature of each heating zone was controlled using the GEFRAN 800 control units. The temperature inside the reactor tubes and reactor heads was measured using the GEFRAN 40 control units.

AFROX pre-mixed gas cylinders were used during catalytic performance evaluations. Cylinder (i) contains a gas mixture of 1 % CO, 56 % H_2, and 43 % N_2, and cylinder (ii) contains 21 % O_2 and 79 % N_2. The gas passes through pressure regulators which maintain the inlet pressure to the MFCs below 20 bar. Once the gases exit the MFCs, they were mixed in a blending pot at 4 bar. Before entering the reactor the pressure was regulated to atmospheric pressure. Once the gas mixture exits the reactor it passes through a Lauda condenser to trap water from the reactor outlet.

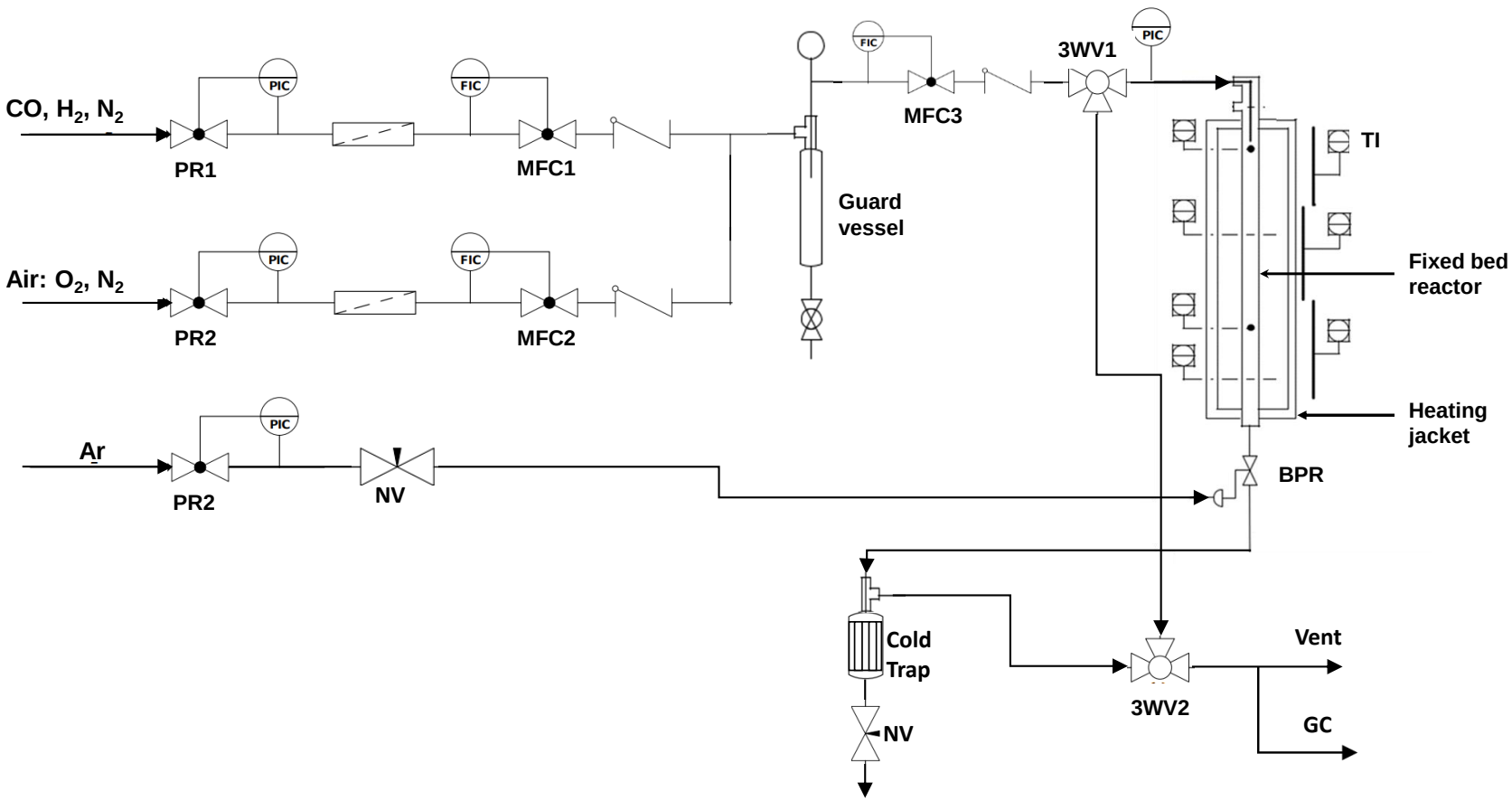

Figure 4.2: A schematic representation of a physical setup of the rig set-up. PR: pressure regulator, MFC: mass flow controller, 3WV: three-way valve, NV: needle valve, BPR: back pressure regulator, TI: temperature indicator, and GC: gas chromatogram.

4.5.4 Reactor packing

To pack the reactor a wad of glass wool was placed at the bottom of the reactor followed by SiC with a particle size of 1mm until the isothermal zone was reached. This was followed by another wad of glass wool. 1 g of catalyst was mixed with 3g of SiC with a particle size of 300 μm to increase the volume of the catalyst bed. This mixture was loaded into the reactor after, which another layer of glass wool was added on top. Finally, SiC with a particle size of 1 mm was added to fill up the reactor and to pre-heat the gas before reaching the catalyst bed as shown in figure 4.3. The reactor was mounted into the heating block and connected to the gas inlet and outlet. A gas mixture containing 1 % CO, 1 % O_2, 56 % H_2, and 43 % N_2 was used during the catalytic performance evaluations and a space velocity of 60000 ml (NTP)/g_{Co3O4}/hr was maintained. The temperature was ramped up from 50 to 450 °C at a ramp rate of 0.24 °C/min.

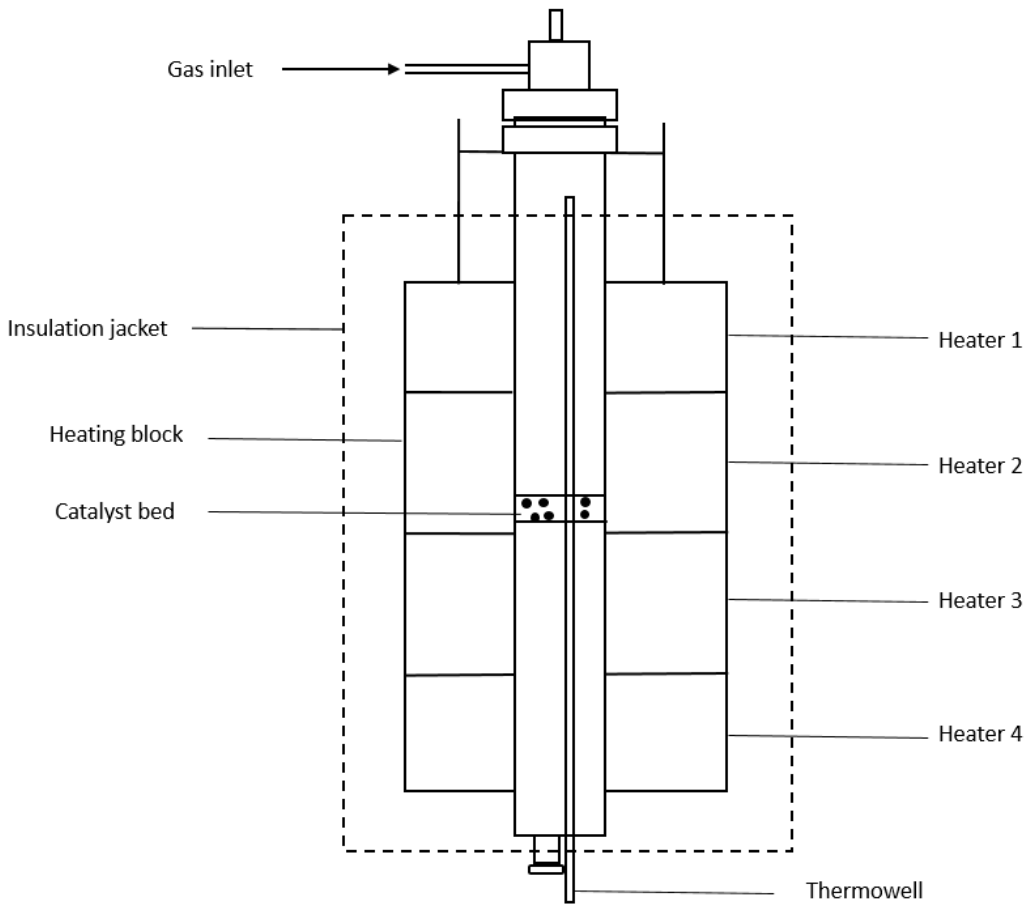

Figure 4.3:: Cross section of the reactor tube showing the reactor with the catalyst bed in the heating jacket.

4.6 CO-Temperature programmed reaction

To investigate the temperature for CO activation and oxygen storage capacity of the catalysts, CO-temperature programmed reactions were performed. 1 g of catalyst was mixed with 3 g of SiC (300 μm) and loaded into the reactor. A gas mixture of 4 % CO and 96 % N_2 flowed into the reactor while increasing the temperature from 50 to 450 °C at 0.24 °C/min. The CO conversion and CO_2 yield (Y_{co2}) were calculated using equations 4.11 and 4.12 respectively.

5 Results and Discussion

5.1 Characterization

5.1.1 ICP-OES

ICP-OES was used to determine the loading of Co_3O_4 nanoparticles and the promoters. The targeted loading for Co_3O_4 was 10 wt.%. To vary the molar ratio of Co: promoter we targeted 0.3, 0.5, and 1 wt.% loading of the promoters. The actual loadings were close to the targeted values for Co_3O_4 and FeO_x as shown in table 5.1. This shows the success of using ultrasonication-assisted wet impregnation when promoting and supporting Co_3O_4. However, for the Mn promoter, the weight percentages are much lower than the targeted loadings. This might be because the Mn precursor is hygroscopic, it absorbs and retains moisture. So, when you weigh the required mass of the precursor, the mass also includes H_2O and the mass of Mn required is underestimated. The loading of Co_3O_4 was further confirmed by Rietveld refinement using TOPAS 5 software on the XRD patterns of the samples. The values obtained from both methods are in good agreement.

Table 5.1: Co_3O_4, MnO_x, and FeO_x loadings obtained from ICP-OES and XRD.

Catalyst name	**Type of Promoter**	**Targeted Co_3O_4 loading wt.%)**	**Actual Co_3O_4 loading (wt.%) (ICP-OES)**	**Actual Co_3O_4 loading (wt.%) (XRD)**	**Targeted promoter loading (wt.%)**	**Promoter wt.% (ICP-OES)**
Co_3O_4/CeO_2	N/A	10	8.80	8.00	N/A	N/A
0.3 wt.% MnO_x	MnO_x	10	9.09	9.00	0.30	0.18
0.5 wt.% MnO_x	MnO_x	10	9.00	8.90	0.50	0.30
1 wt.% MnO_x	MnO_x	10	9.75	9.75	1.00	0.80
0.3 wt.% FeO_x	FeO_x	10	9.90	9.00	0.30	0.25
0.5 wt.% FeO_x	FeO_x	10	9.50	8.90	0.50	0.40
1 wt.% FeO_x	FeO_x	10	9.00	9.20	1.00	0.92

5.1.2 TEM

The Co_3O_4 nanoparticles were synthesized using solvothermal treatment to ensure that we obtain nanoparticles with uniform particle size distribution (Wolf et al., 2017). The synthesis of Co_3O_4 monodispersed nanoparticles is important in this study. A wide variety in the particle size distribution of Co_3O_4 can result in size effects affecting the catalytic performance of our samples.

With TEM we were able to confirm the success of the synthesis of monodispersed nanoparticles, the number-based and volume-based average particle size, particle size distribution, and shape of the unsupported Co_3O_4 nanoparticles. Using the imageJ free software 300 particles in the micrographs of unsupported Co_3O_4 were measured. The nanoparticles are cubic and show little to no agglomeration. The nanoparticles have a number-based average particle size of 7.0 ± 1.9 nm and a volume-based average particle size of 9.6 ± 1.6 nm as shown in figure 5.1. The number and volume-based average particles sizes are comparable. Additionally, the particle size distribution is reasonably narrow as seen in figure 5.1. This was further confirmed by the small standard deviations obtained (±1.9 nm for the number based and ± 1.6 nm for the volume particle sizes).

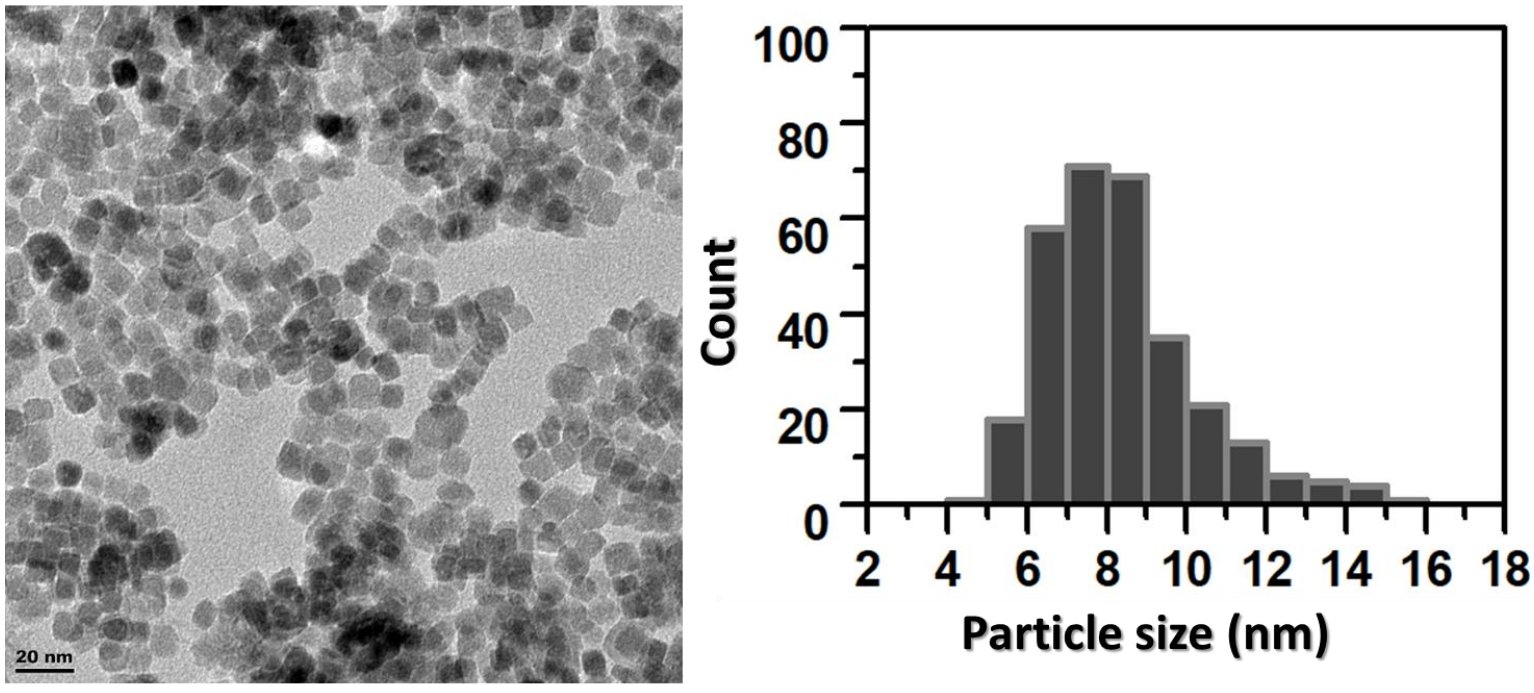

Figure 5.1: Unsupported Co_3O_4 nanoparticle size and nanoparticle size distribution calculated from 300 particles.

A micrograph of the supported and promoted Co_3O_4 nanoparticles is shown in figure 5.2. After the Co_3O_4 nanoparticles were supported on CeO_2 it was harder to analyze their dispersion on the support. This is because of the low contrast between Co and Ce. Therefore the dispersion of promoted and unpromoted Co_3O_4 on CeO_2 was not determined.

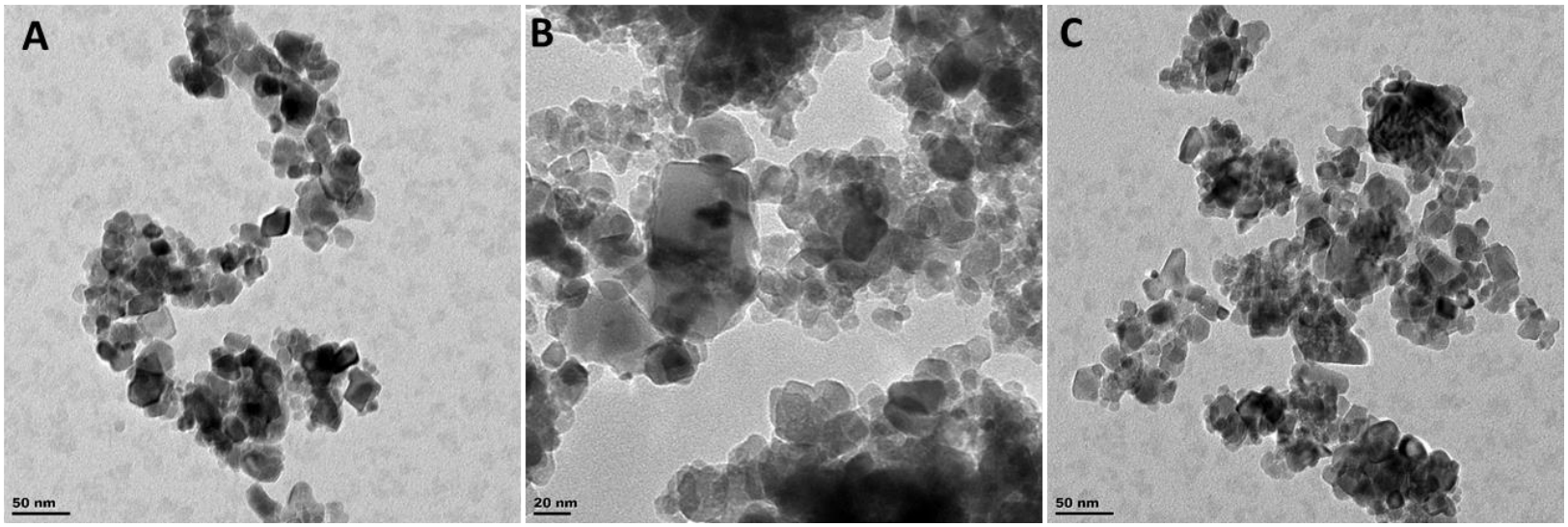

Figure 5.2: Promoted and supported Co_3O_4. (A)Co_3O_4/CeO_2, (B) MnOx-Co_3O_4/CeO_2, and (C) FeO_x-Co_3O_4/CeO_2.

5.1.3 Scanning Transmission Electron Microscopy coupled with Energy Dispersive Spectroscopy

A Bright-field STEM image of the unpromoted catalyst is shown in figure 5.5. The d-spacing of 0.24 nm corresponds to the (111) crystal plane of Co_3O_4 (Gryzybek et al., 2015; Slowik et al., 2016). While the d-spacings of 0.28nm and 0.46 nm correspond to (200) and (111) crystal planes respectively (Gryzybek et al., 2015; Slowik et al., 2016). One of the Co_3O_4 nanoparticles has various crystalline orientations: (200) and (311) planes.

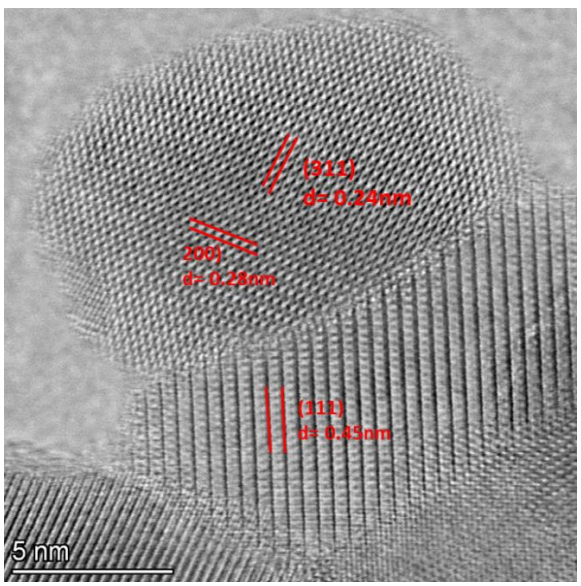

Figure 5.3: Bright-field STEM image of unpromoted Co_3O_4/CeO_2

Figure 5.4 shows the bright-field micrographs and elemental distribution of Ce, Co, Mn, or Fe for 0.3 wt.% promoted catalysts. There is a Co signal on the CeO_2 support and some of the signals show that some Co_3O_4 nanoparticles were not distributed on the support. The Co_3O_4 nanoparticles that are not interacting with support are more likely to agglomerate during the catalytic performance evaluations which may cause a loss in surface area. The signal for Mn and Fe promoters is distributed on both CeO_2 and Co_3O_4. However, the signal is more distributed in Co_3O_4. The elemental maps for the higher loadings of the promoters are shown in Appendix 2.

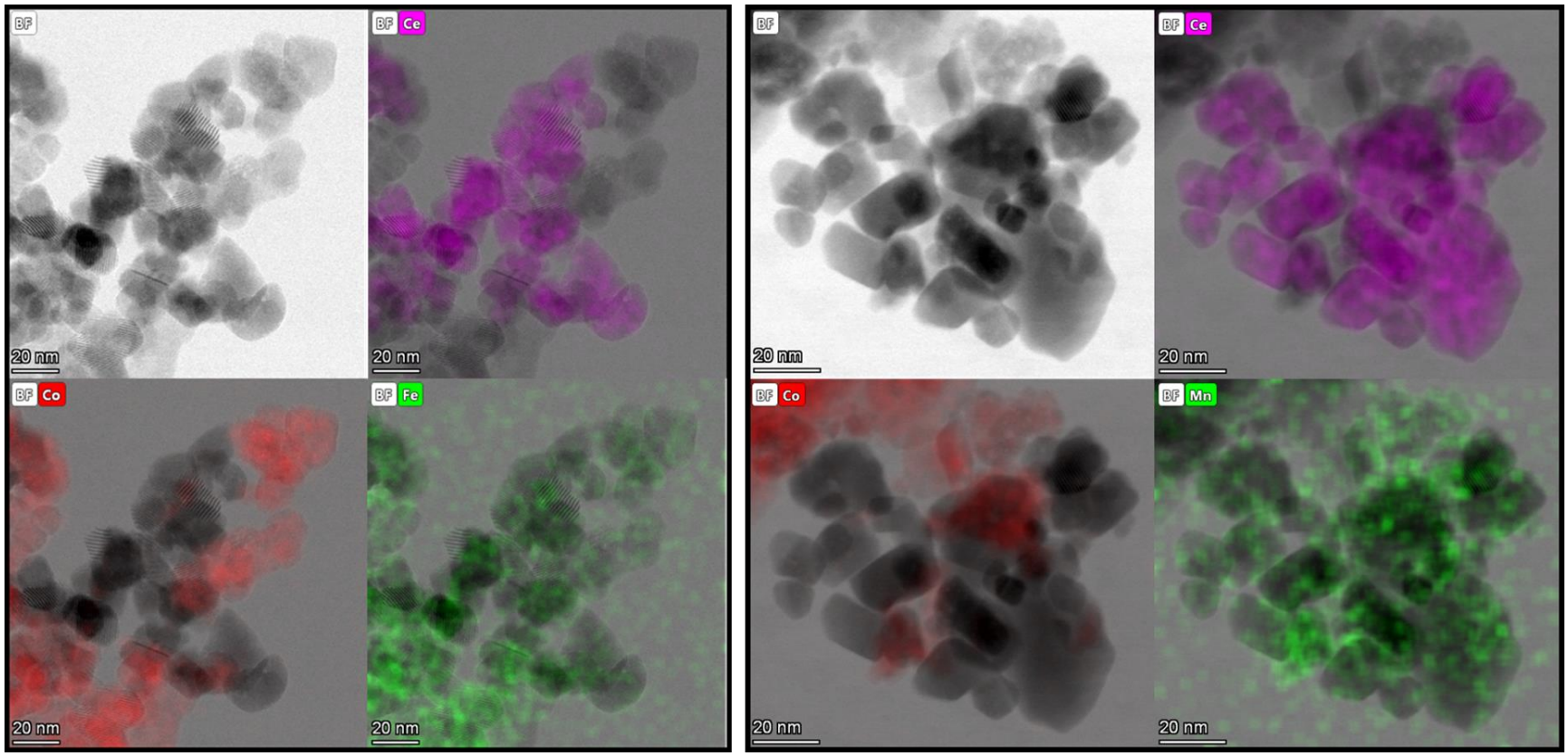

Figure 5.4: Bright-field micrographs and elemental maps for Ce, Co, Fe, or Mn (A)0.3 wt.% FeO_x promoted catalyst (B) 0.3 wt.% MnO_x promoted catalyst.

5.1.3. PXRD

PXRD measurement confirms the crystalline phases present, crystallite size, and loading of the cobalt oxide. The diffraction lines of the prepared samples were compared to the ICDD PDF database. The diffraction lines of the unsupported sample confirm the presence of crystalline, single-phase Co_3O_4 nanoparticles as shown in Appendix 2. For the unpromoted and promoted supported catalyst, the intensity of the diffraction lines corresponding to Co_3O_4 is low. This might be due to the high dispersion of Co_3O_4, high crystallinity of CeO_2, and overlapping diffraction lines as shown in figures 5.5 A and B. This was also observed in similar studies (Guo and Liu, 2008; Grzybek et al., 2019; Nyathi et al., 2021). Furthermore, no diffraction lines were corresponding to the promoters this might be because a small amount of the promoters was added, or they are amorphous or highly dispersed. This was also observed in studies by (Zhang et al., 2012; Zhao et al., 2012).

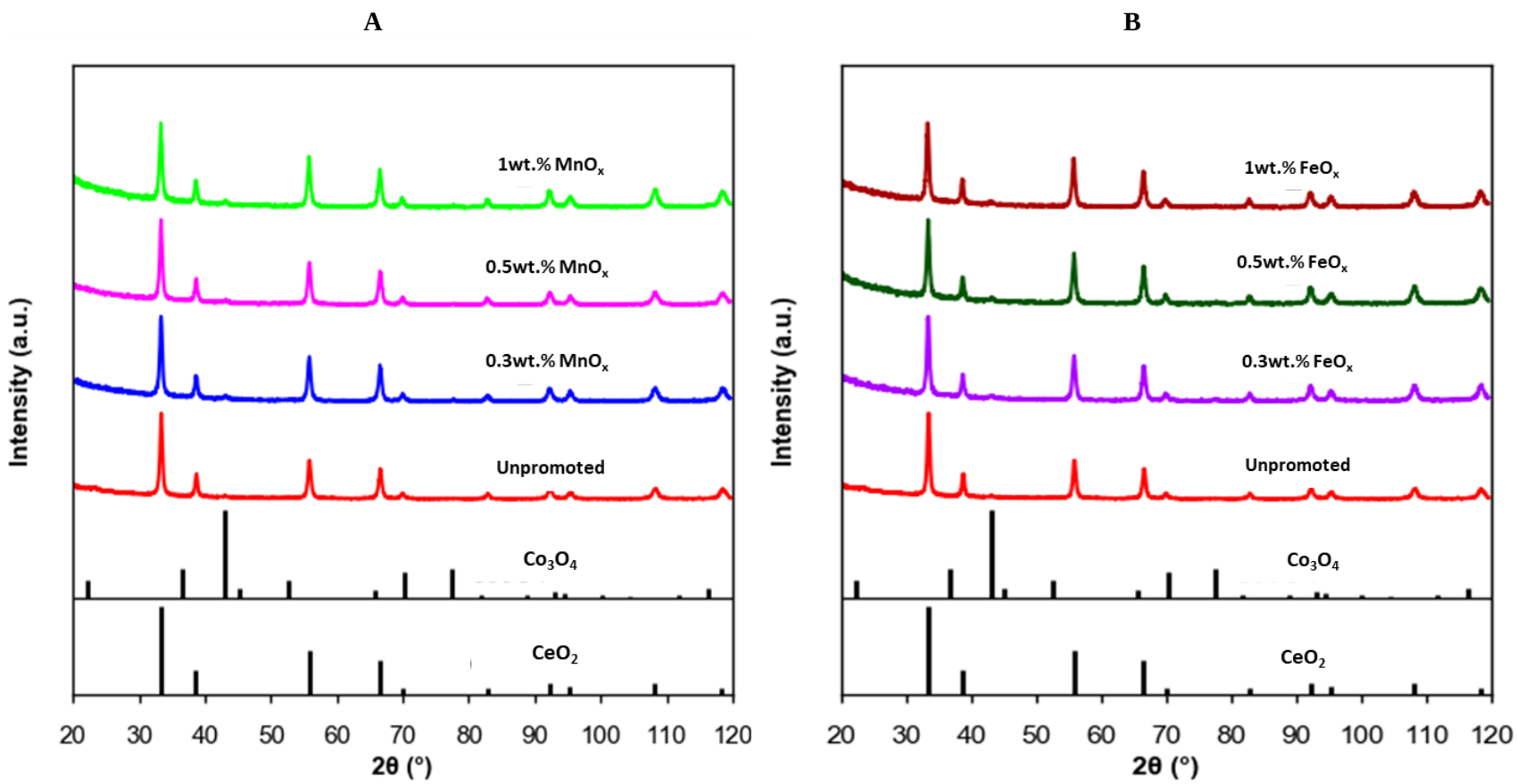

Figure 5.5: XRD patterns of A: MnO_x and B: FeO_x promoted Co_3O_4/CeO_2 catalysts and the reference diffraction lines of Co_3O_4 and CeO_2

The average Co_3O_4 crystallite size was determined using the Rietveld method for all the calcined catalysts as shown in table 5.2. There is an increase in the Co_3O_4 crystallite size after supporting and promoting the nanoparticles, which might be due to sintering during the calcination step during the synthesis of these catalysts.

Table 5.2: Crystallite size of Co_3O_4 obtained from Rietveld method.

Sample	Crystallite size nm
Co_3O_4/CeO_2	10.0 ± 4.8
0.3 wt.% MnO_x	15.0 ± 2.6
0.5 wt.% MnO_x	15.3 ± 2.6
1 wt.% MnO_x	16.7 ± 4.3
0.3 wt.% FeO_x	16.0 ± 4.0
0.5 wt.% FeO_x	15.6 ±2.6
1 wt.% FeO_x	14.9 ± 2.6

5.1.4 TPR

The reduction of Co_3O_4 to metallic Co at temperatures > 225 °C has been identified as one of the deactivation mechanisms of Co_3O_4-based catalysts during CO-PROX (Zhao et al., 2012; Khasu et al., 2017; Nyathi et al., 2017). TPR was conducted to determine the effect of promoters on the reducibility and degree of reduction of Co_3O_4 supported on CeO_2 (Co_3O_4/CeO_2). The temperature of the reduction peaks and the number of peaks vary in the literature depending on factors such as the particle/crystallite size of Co_3O_4 nanoparticles, type of support used, metallic loading onto a support, and synthesis method used (Gawade et al., 2012; Zhao et al., 2012; Nyathi, 2016; Khasu, 2017; Lukashuk et al., 2016).

The reduction of Co_3O_4 occurs in two reduction steps see equations 2.16 and 2.17. The reduction of MnO_2 and Fe_2O_3 occurs in three steps as shown in equations 5.1 to 5.6.

$$3MnO_2 + 2H_2 \rightarrow Mn_3O_4 + 2H_2O \qquad \text{Equation 5.1}$$

$$Mn_3O_4 + H_2 \rightarrow 3MnO + H_2O \qquad \text{Equation 5.2}$$

$$MnO + H_2 \rightarrow Mn + H_2O$$ Equation 5.3

$$3Fe_2O_3 + 2H_2 \rightarrow 2Fe_3O_4 + 2H_2O$$ Equation 5.4

$$Fe_3O_4 + 2H_2 \rightarrow 3FeO + 2H_2O$$ Equation 5.5

$$FeO + H_2 \rightarrow Fe + H_2O$$ Equation 5.6

The hydrogen consumption of MnO_x and FeO_x promoted catalysts are shown in figures 5.6 and 5.8, respectively. The reduction profile for the unpromoted catalyst has three hydrogen peak maxima. The first reduction peak occurs at 249 °C which corresponds to the reduction of Co_3O_4 to CoO. The maximum temperature for the second reduction occurs is at 317 °C. Lastly, the broad peak at 700 °C is ascribed to the reduction of CeO_2 (Gómez, Miró, and Biox, 2013; Nyathi, 2020).

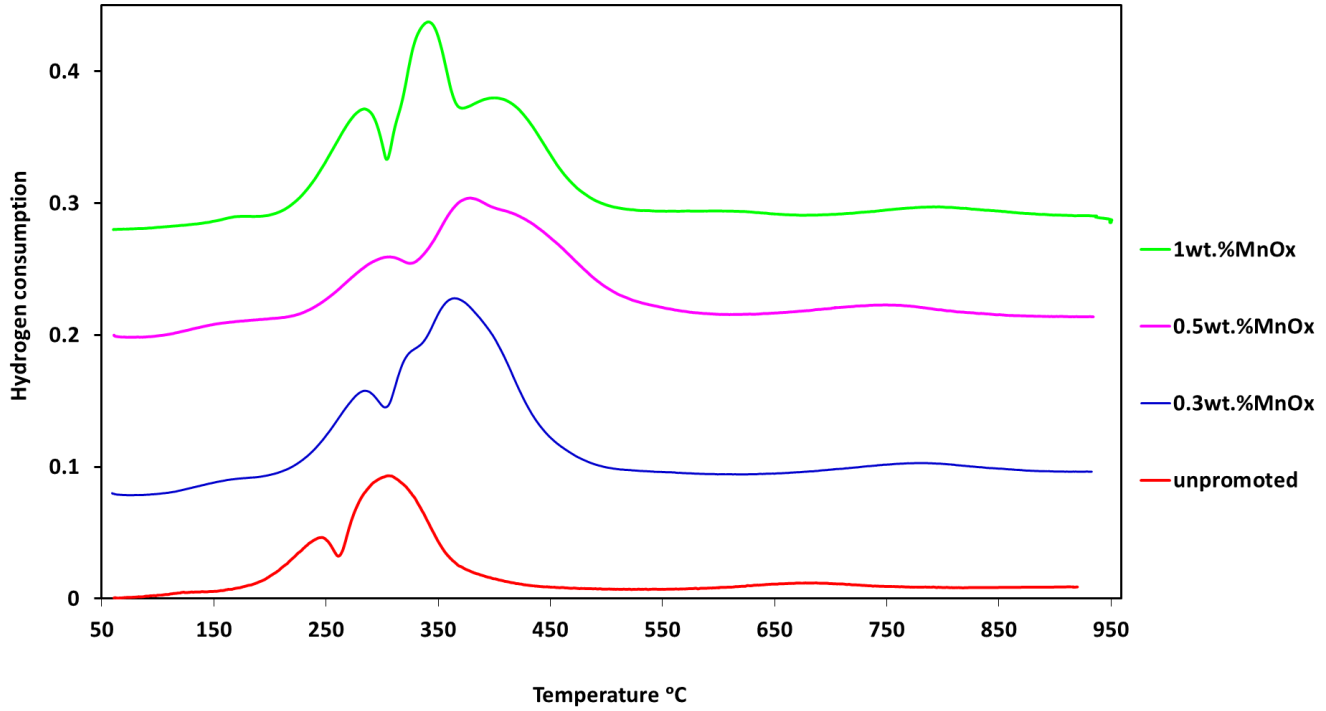

Figure 5.6: TPR profiles of unpromoted catalyst Co_3O_4/CeO_2 and MnO_x-promoted catalysts.

The promoted catalysts have four reduction peaks. The first two reduction peaks correspond to the reduction of Co_3O_4 to Co, MnO_2 to MnO, and Fe_2O_3 to FeO. The third peaks correspond to the reduction of MnO to Mn and FeO to Fe. The fourth peak at higher temperature corresponds to CeO_2 reduction. Compared to the unpromoted catalyst, the Co_3O_4 reduction peaks for the promoted catalysts are shifted to higher temperatures. For 0.3 wt.% MnO_x promoted catalyst, the reduction peak for Co_3O_4 and MnO_2 occurs at 284 °C. The maximum temperature for the reduction for CoO and Mn_3O_4 occurs at 327 °C. The reduction of Mn_3O_4 occurs at 364 °C. The second and third peaks overlap. While the reduction of CeO_2 occurred at 775 °C. For the 0.3 wt.% FeO_x promoted catalyst, the reduction of Co_3O_4 and Fe_2O_3 occur 270 °C. The reduction of CoO and Fe_3O_4 occurs at 346 °C, CeO_2 reduces at 740 °C. Further increase in the amount promoter further increases the reduction temperature of Co_3O_4. For the 0.5 wt.% MnO_x promoted catalyst, the first reduction peak occurs at 291 °C. The maximum temperature for the reduction of CoO and MnO_2 occurs at 373 °C. The reduction of MnO occurs at 429 °C. The second and third peaks merge. Peak deconvolution of the reduction profiles was performed using the pseudo-Voigt function in Origin 2016 software. Figure 5.7 shows the peak fitted profile for 0.5 wt% MnO_x promoted catalyst (see Appendix 2 for the fitted profiles of the other MnO_x promoted catalyst). The reduction of CeO_2 occurred at 760 °C.

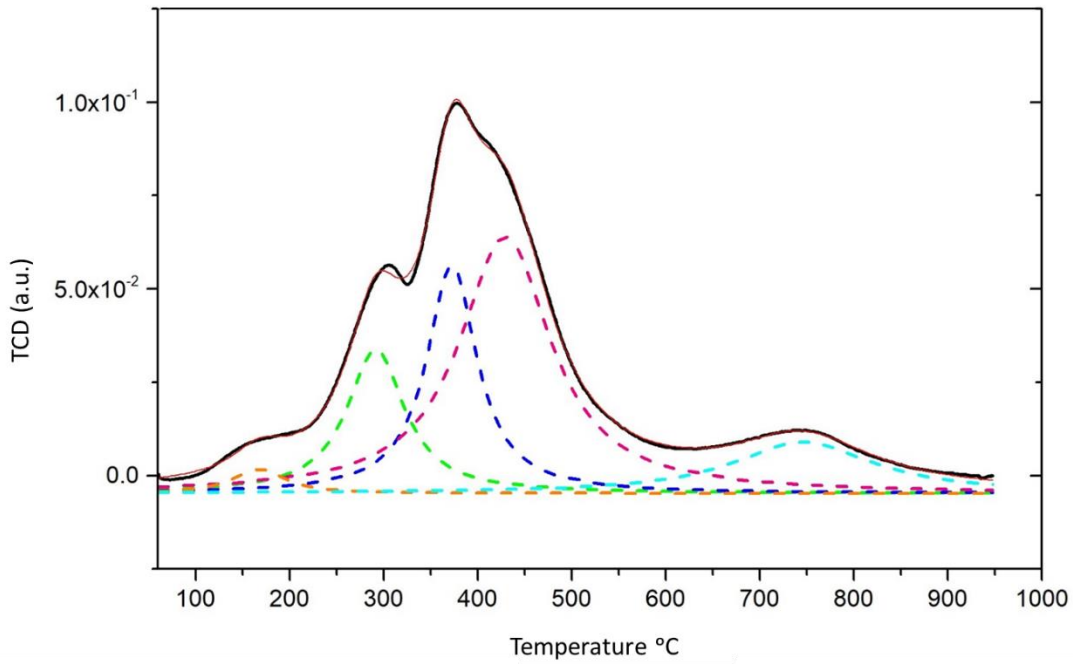

Figure 5.7: 0.5 wt% MnOx promoted deconvoluted hydrogen consumption profile. Solid black line - raw data, red solid line - cumulative curve, and dotted lines- fitted lines.

For the 0.5 wt.% FeO_x promoted catalyst, the first reduction peak occurs at 284 °C, the reduction of CoO and Fe_3O_4 occurs at 370 °C. The reduction of FeO and CeO_2 occurs at 500 °C and 780 °C, respectively. The first reduction peak occurs at 286 °C for 1 wt.% MnO_x. The second reduction peak occurs at 346 °C. The reduction of MnO occurs at 408 °C. Reduction of CeO_2 occurs at 800 °C. For the 1wt.% FeO_x promoted catalyst, the first reduction occurs 300 °C. The reduction step occurs at 390 °C. Reduction of FeO and CeO_2 occur at 492 °C and 750 °C. Table 5.3 summarises the hydrogen consumption and degree of reduction of the catalysts calculated using equations 4.3 and 4.6, respectively. The unpromoted catalyst

has the highest H_2 consumption and its degree of reduction is 96%. For the promoted catalysts the degree of reduction decreases with increasing loading of the promoter. This shows the interaction of the cobalt with the promoters stabilizes its oxide phase.

Table 5.3: Hydrogen consumption and degree of reduction for unpromoted catalyst and promoted catalysts.

Sample	**Onset reduction temperature**	**H_2 consumption (mmol)**	**Degree of reduction (%)**
Co_3O_4/CeO_2	170	1.60×10^{-3}	96.0
0.3 wt.% MnO_x	220	1.50×10^{-3}	90.0
0.5 wt.% MnO_x	230	1.42×10^{-3}	85.2
1 wt.% MnO_x	225	1.3×10^{-3}	78.0
0.3 wt.% FeO_x	190	1.48×10^{-3}	88.8
0.5 wt.% FeO_x	220	1.37×10^{-3}	82.2
1 wt.% FeO_x	222	1.22×10^{-2}	73.2

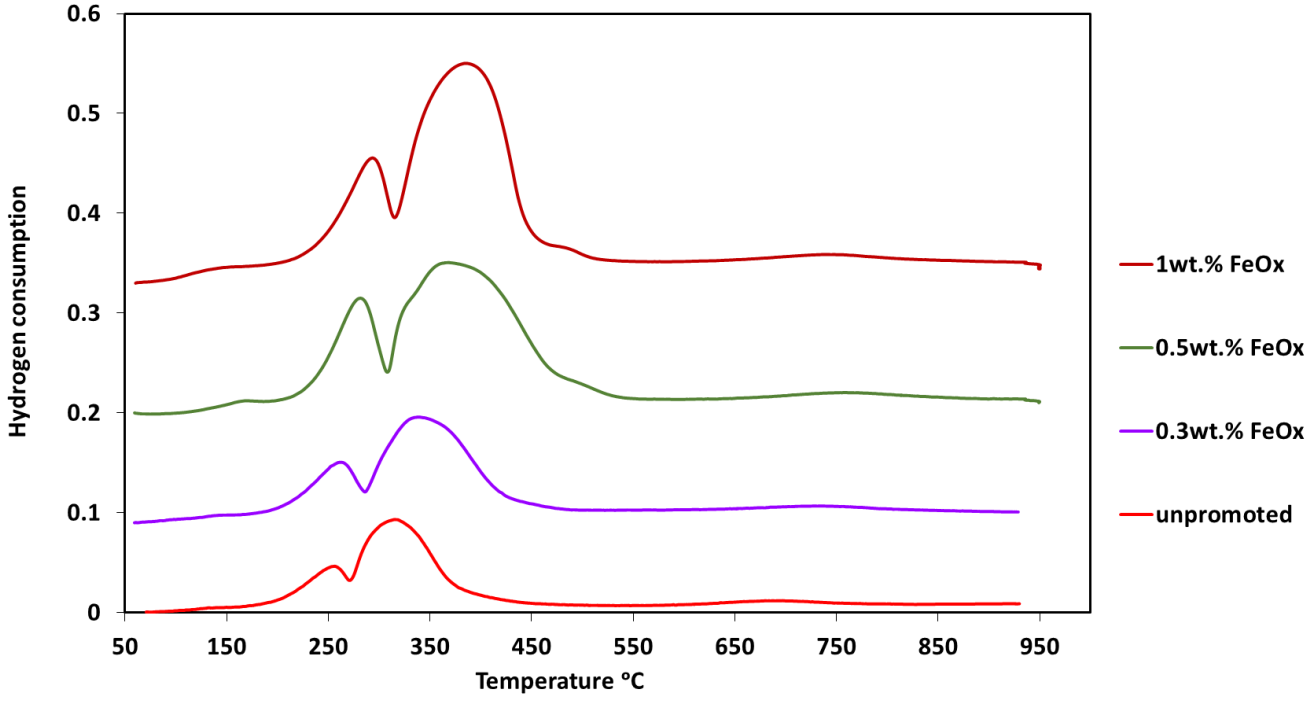

Figure 5.8: TPR profiles of unpromoted catalyst Co_3O_4/CeO_2 and FeO_x-promoted catalyst.

The addition of promoters increases the reduction temperatures of Co_3O_4 compared to the unpromoted catalyst. This implies that for the promoted catalyst, the cobalt oxide phase is more stabilized and hence harder to reduce to metallic Co as the temperature increases. This observation correlates well with observations in previous studies by (Zhang et al., 2012). The increase in the reduction temperature of the promoted catalyst might be a result of a strong interaction between Co and the promoter (Zhang et al., 2012). It has been suggested that there is an electron transfer between the promoter and cobalt which facilitates the oxidation of Co^{2+} and stabilization of Co^{3+} (Zhang et al., 2012; Zhao et al., 2012).

5.1.5 TPO

The redox properties of catalysts play a vital role in the Mars Van Krevelen mechanism which is widely accepted to be at the center of CO-PROX over metal oxide catalysts such as Co_3O_4 (Lukashak et al., 2016). Even though in literature the facile donation of lattice oxygen from the metal oxide to the reactant has been identified as a key step in the Mars-Van Krevelen mechanism; the re-oxidation rate is also a fundamental step (Zou, Meng & Zha, 2010). The ability of the catalysts to replenish their oxygen vacancies is important in sustaining a redox cycle. In the case of cobalt-based catalysts, the reduction of Co_3O_4 to metallic Co has been identified as one of the deactivation mechanisms during CO-PROX (Zhao et al., 2012; Nyathi, 2016; Khasu, 2017).

TPO was performed after TPR to investigate the effect of the promoters on the re-oxizability after reduction.

In literature, the TPO of unsupported metallic cobalt is characterized by two oxygen consumption peaks below 600 °C (Sewell, van Steen & O'Connor, 1995; Iwanek et al., 2021). These peaks correspond to the sequential oxidation of metallic Co to CoO first, then CoO to Co_3O_4 as shown in equations 5.7 and 5.8.

$$Co + \frac{1}{2}O_2 \rightarrow CoO$$ Equation 5.7

$$3CoO + \frac{1}{2}O_2 \rightarrow Co_3O_4$$ Equation 5.8

At temperatures above 840 °C Co_3O_4 decomposes to form thermodynamically stable CoO as shown in equation 5.9 (Sewell, van Steen & O'Connor, 1995).

$$Co_3O_4 \rightarrow 3CoO + \frac{1}{2}O_2$$ Equation 5.9

The oxygen consumption profiles for the unpromoted and MnO_x promoted catalysts are shown in figure 5.12. While figure 5.13 shows the oxygen consumption profiles of the FeO_x- promoted catalysts. The unpromoted catalyst has two overlapping oxygen consumption peaks below 600 °C and one oxygen desorption peak above 850 °C as shown in figure 5.9 and this corresponds with literature. The peak for oxidation of Co to CoO occurs at 430 °C and the sequential oxidation occurs at 501 °C. The overlapping of these peaks means that the oxidation of Co to CoO and CoO to Co_3O_4 are occurring simultaneously as shown in figure 5.12 (Petersen, 2018). Lastly, Co_3O_4 decomposes at 852 °C.

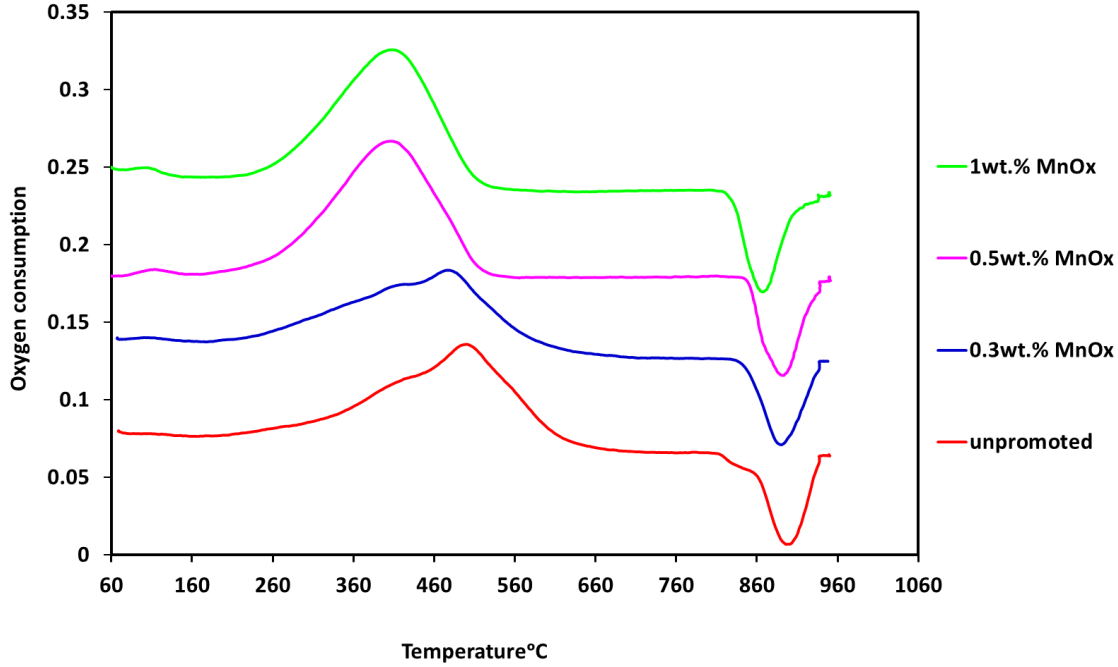

Figure 5.9: TPO profiles of unpromoted catalyst Co_3O_4/CeO_2 and MnO_x-promoted catalysts.

For 0.3 wt.% MnO_x promoted catalyst the oxygen consumption temperatures shifted to lower temperatures. The peak maximum for Co to CoO oxidation occurs at 425 °C and the maximum temperature for oxidation of CoO to Co_3O_4 occurs at 486 °C. The decomposition of Co_3O_4 occurs

at 891 °C. For 0.3 wt.% FeO_x promoted catalyst the oxidation occurs at 410 °C and the maximum temperature for oxidation of CoO to Co_3O_4 occurs at 507 °C. The decomposition peak minimum of Co_3O_4 occurs at 896 °C.

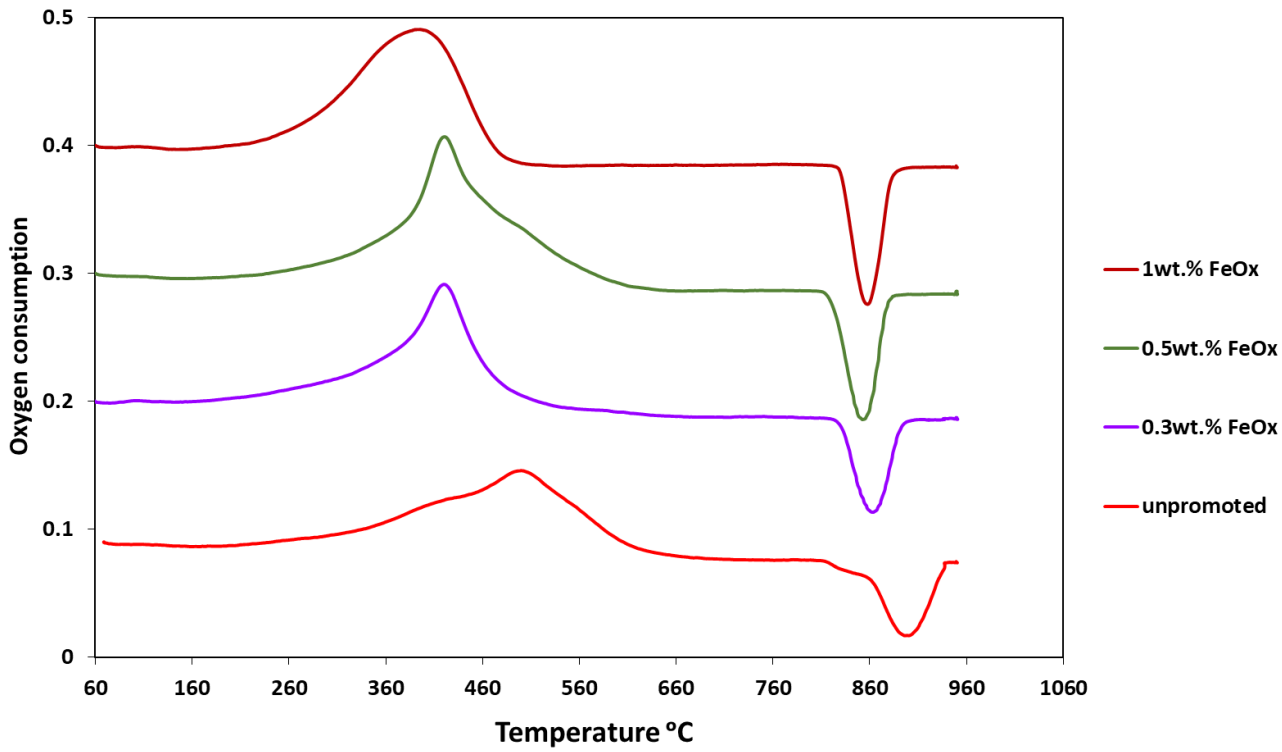

Figure 5.10: TPO profiles of unpromoted catalyst Co_3O_4/CeO_2 and FeO_x-promoted catalysts.

Figure 5.11 shows the peak fitted profile for 0.5wt% MnO_x promoted catalyst (see Appendix 2 for the other catalysts). For 0.5wt% MnO_x promoted catalyst, Co to CoO oxidation occurs 367 °C, the peak maximum of the oxidation of CoO to Co_3O_4 occurs at 426 °C. The decomposition of Co_3O_4 occurs at 868 °C. For 0.5 wt.% FeO_x promoted catalyst the oxidation occurs at 349 °C, the second oxidation step peak maximum occurs at 420 °C. Co_3O_4 decomposes at 862 °C. Further increase of the loading of the promoters decreases the re-oxidization temperature. The oxidation of Co to CoO occurs at 361 °C and oxidation of CoO to Co_3O_4 occurs at 424 °C for 1 wt.% MnO_x promoted catalyst. The decomposition of Co_3O_4 occurs at 890 °C. For 1 wt.% FeO_x promoted catalyst, the first oxidation occurs at 330 °C and the peak maximum of the second oxidation step occurs at 390 °C. The decomposition of Co_3O_4 occurs at 857 °C.

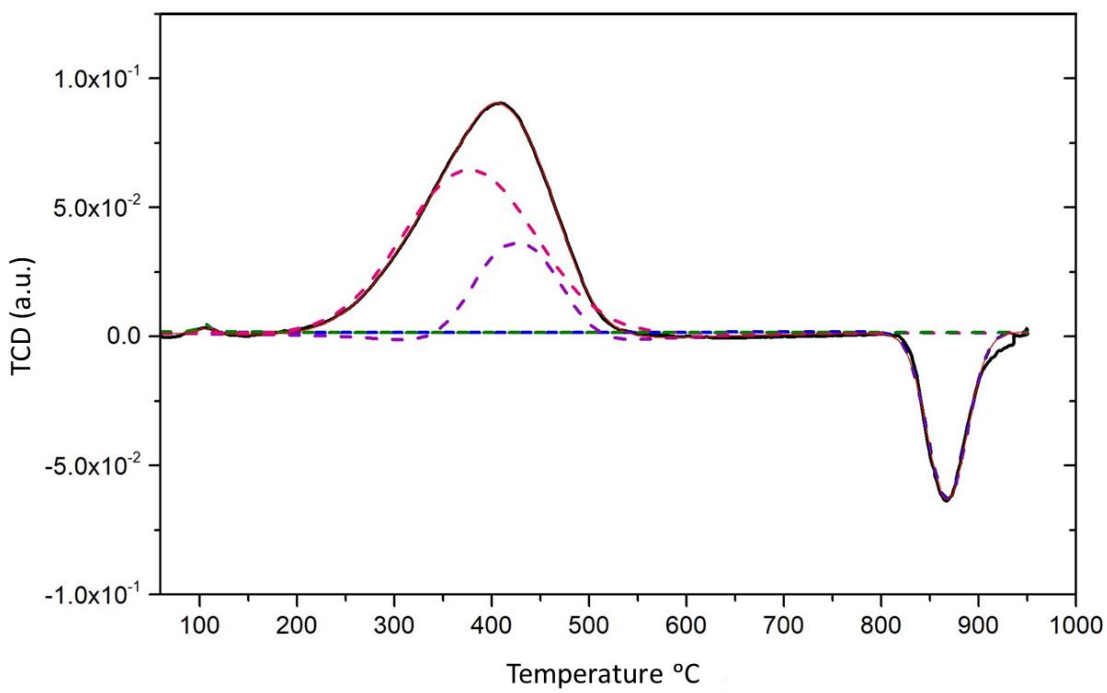

Figure 5.11: 0.5wt% MnO_x deconvoluted oxygen consumption profile. Solid black line - raw data, red solid line - cumulative curve, and dotted lines- fitted lines.

5.1.7. CO-TPRE

The temperature for CO activation and the oxygen storage capacity were investigated by performing CO-TPRE evaluations. These experiments were conducted in the rig set up in the absence of gaseous oxygen and hydrogen to ensure the oxygen involved in the oxidation of CO is solely lattice oxygen of the catalysts. 1g of sample was used and the temperature was ramped from 50 °C to 450 °C while flowing 5% CO in 95% N_2. The CO consumption and CO_2 yield were determined from CO-TPRE.

CO-TPRE was performed for unpromoted catalyst, 0.3wt%, and 1 wt.% promoted catalysts. For unpromoted catalyst, CO activation commences at 320 °C. A maximum CO consumption of 4% was achieved at 330 °C as shown in figure 5.12. At this temperature, CO is reacting with surface lattice oxygen. A further increase in temperature results in the deactivation of the catalyst which we can attribute to the surface reduction of the Co_3O_4. A carbon mass balance was calculated for the catalysts and the graphs shown in Appendix 2 show that the mass of carbon out in the form of CO and CO_2 is slightly less than the carbon in. Thus, it can be concluded that the CO consumption is not only due to CO oxidation. The consumption of CO can also be either CO by disproportionation or dissociation as shown in equations 5.10 and 5.11 respectively Coking during CO-TPRE was also reported by Lukashuk (2016).

$$2CO \rightarrow C + CO_2 \qquad \text{Equation 5.10}$$

$$CO \rightarrow C + O$$ Equation 5.11

For the MnO_x-promoted catalysts, CO activation commences at 300 °C. The maximum CO conversion achieved by 0.3 wt.% MnO_x is 25 % while 1 wt.% MnO_x promoted catalyst achieved 50 %. Thus, the addition of the MnO_x promoter increases the oxygen storage capacity of the catalyst. The maximum CO_2 yield achieved by 0.3 wt.% MnO_x was 21 % while 1 wt.% MnO_x promoted achieved 40 % yield. For 0.3 wt.% FeO_x promoted the maximum CO conversion achieved was 25% CO conversion as shown in figure 5.16 and a maximum CO_2 yield of 24 %. Furthermore, the maximum CO conversion for 1 wt.% FeO_x promote was 51 % and a maximum yield CO_2 of 45 % was achieved.

The promoted catalysts have lower CO activation temperatures. Additionally, they have a higher oxygen storage capacity when compared to the unpromoted catalyst. The lower CO activation temperature for the promoted catalysts might be the result of the better redox properties of these catalysts. This might be due to the berthollide structure of the promoters which contains labile lattice oxygen. This allows the promoters to form variable oxidation states which allow for easier electron transfer. It was concluded that increasing the amount of the promoters increases the number of Co-O-Mn and Co-O-Fe interfaces, this results in higher oxygen mobility or that the promoters provide alternative active sites for the Mars Van Krevelen mechanism. So, the increase in the CO conversion is the result of having two sources of oxygen in the promoted catalysts.

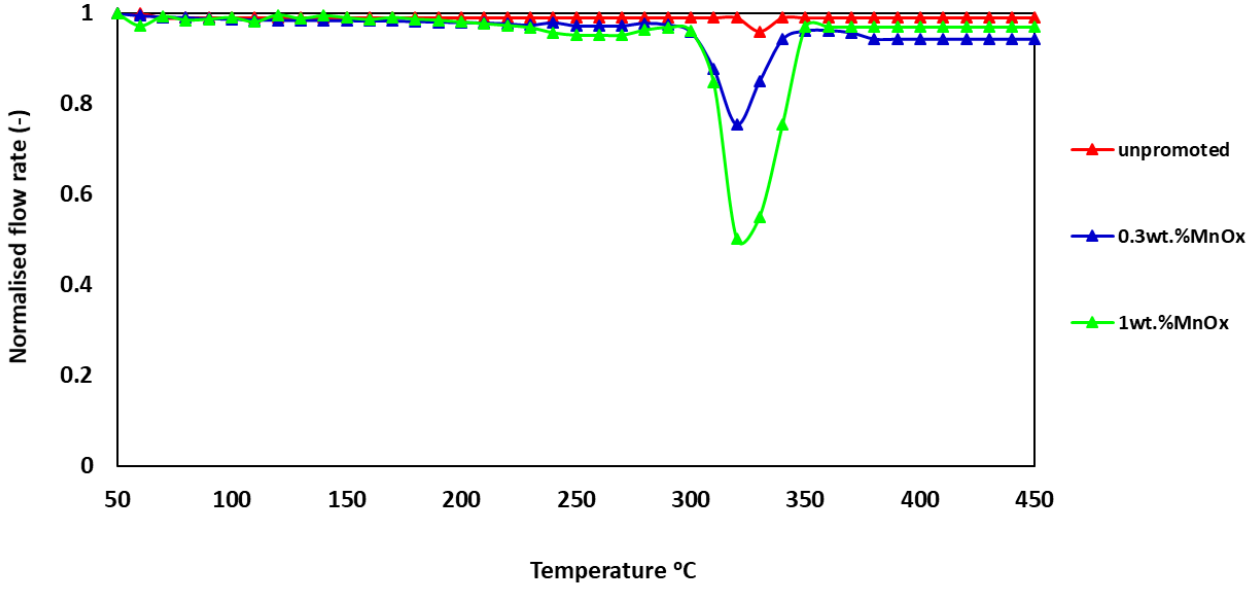

Figure 5.12: CO-TRE profiles of unpromoted catalyst and MnO_x-promoted catalysts.

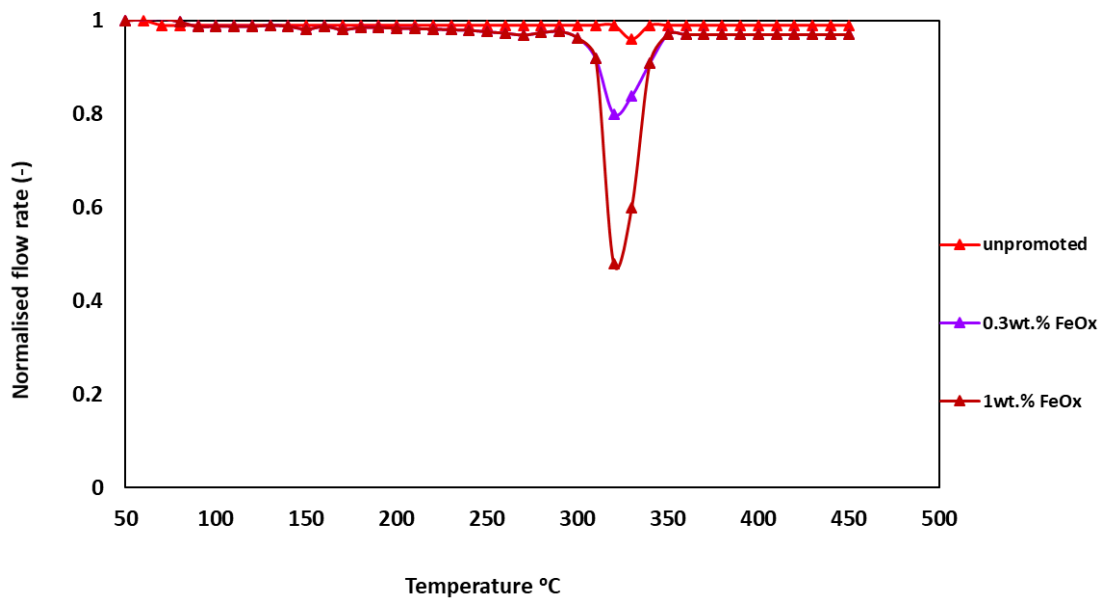

Figure 5.13: CO-TPRE profiles of unpromoted catalyst and FeO_x-promoted catalysts.

5.2 Catalytic performance evaluations

For the unpromoted catalyst, the catalytic performance is shown in figure 5.14. CO is converted to CO_2 from 50 °C reaching a maximum CO to CO_2 conversion of 71 % at 220 °C. Further increase in the temperature decreases the activity. The onset temperature of CH_4 formation is above 270 °C, which correlates to the formation of metallic Co. Therefore, below 270 °C CO-PROX is the only CO consumption reaction taking place, and above 270 °C both CO-PROX and CO-methanation are active reactions. Above 275 °C CO-methanation is the more dominant reaction. At 400 °C there is no more CO_2 formed and we have 100 % CO conversion to CH_4 which implies that the catalyst is fully reduced.

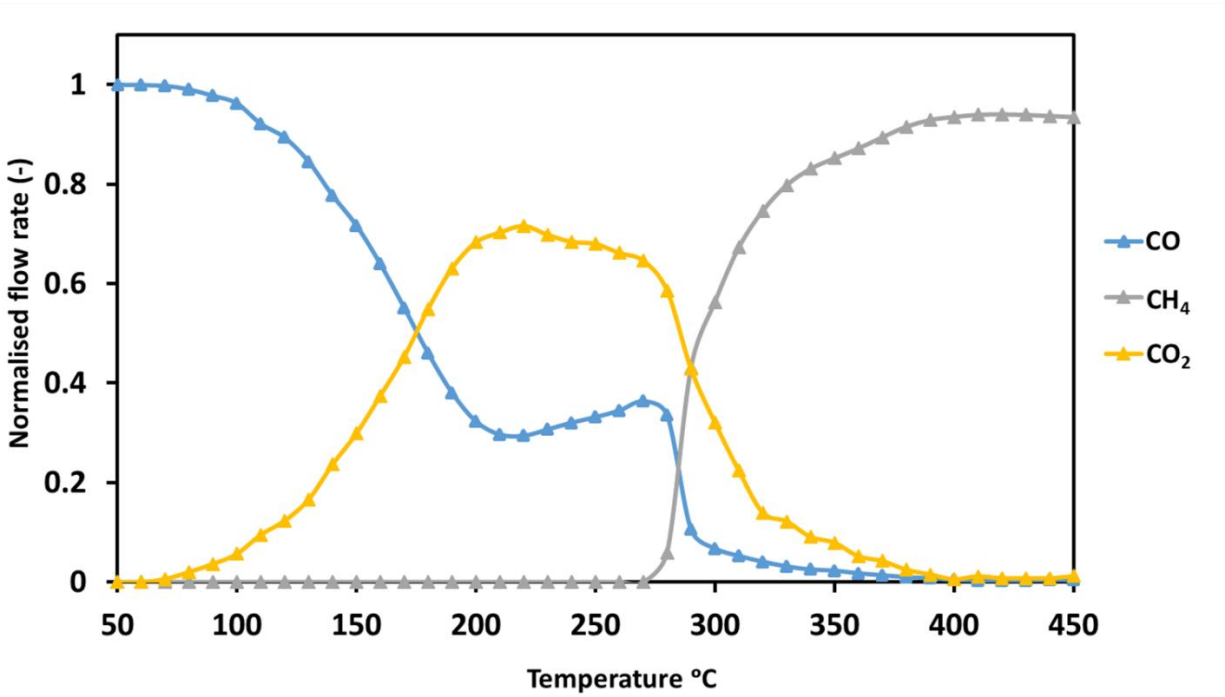

Figure 5.14: Normalised outlet flow rates of CO, CO_2, and CH_4 as a function of temperature for unpromoted catalyst.

For all the promoted catalysts the activity is higher than the unpromoted catalyst which is attributed to the improved redox properties and oxygen storage capacity of the catalysts upon the addition of MnO_x as shown in the TPR-TPO and CO-TPRE experiments. For the 0.3 wt.% MnO_x promoted catalyst, CO to CO_2 conversion increases and reaches a maximum of 85 % from 240-270 °C and decreases after 270 °C. The formation of CH_4 commences above 270 °C which is like the unpromoted catalyst. However, for this catalyst CO_2 formation continues until 450 °C concurrently with CH_4 formation even though the yield is low. This implies that this catalyst does not get fully reduced to metallic Co. For 0.3 wt.% FeO_x promoted catalyst, CO to CO_2 conversion increases and reaches a maximum of 75 % at 230 °C and decreases after 230 °C. The formation of CH_4 commences above 300 °C which is at a higher temperature than the unpromoted catalyst and the 0.3 wt.% MnO_x promoted catalyst. CO_2 formation continues until 410 °C when full reduction is reached.

The 0.5 wt.% MnO_x promoted catalyst achieves a maximum CO to CO_2 conversion of 98.8 % from 210-230 °C. Higher CO conversions are reached at lower temperatures compared to the unpromoted and 0.3 wt.% MnO_x promoted catalysts as shown in figure 5.15. The formation of CH_4 commences above 300 °C. Similarly, the 0.3 wt.% promoted catalyst did not get fully reduced. Increasing the loading of FeO_x to 0.5 wt.% increases the CO conversion to 100 % from 210-220 °C as shown in figure 5.16. The formation of CH_4 commences above 300 °C and this catalyst does not fully reduce until 450 °C.

The 1 wt.% MnO_x promoted catalyst achieves a maximum CO to CO_2 conversion of 92 % from 180-220 °C which is at a slightly lower temperature compared to the 0.5 wt.% promoted catalyst. CH_4 commences above 310 °C which is at a higher temperature than in the previous catalysts. A further increase in the loading of FeO_x to 1 wt.% decreases the maximum CO conversion to 88% between 220-230 °C. CH_4 formation commences above 310 °C and there is no full reduction. Increasing the loading of FeO_x leads to a similar trend to the MnO_x promoted catalyst.

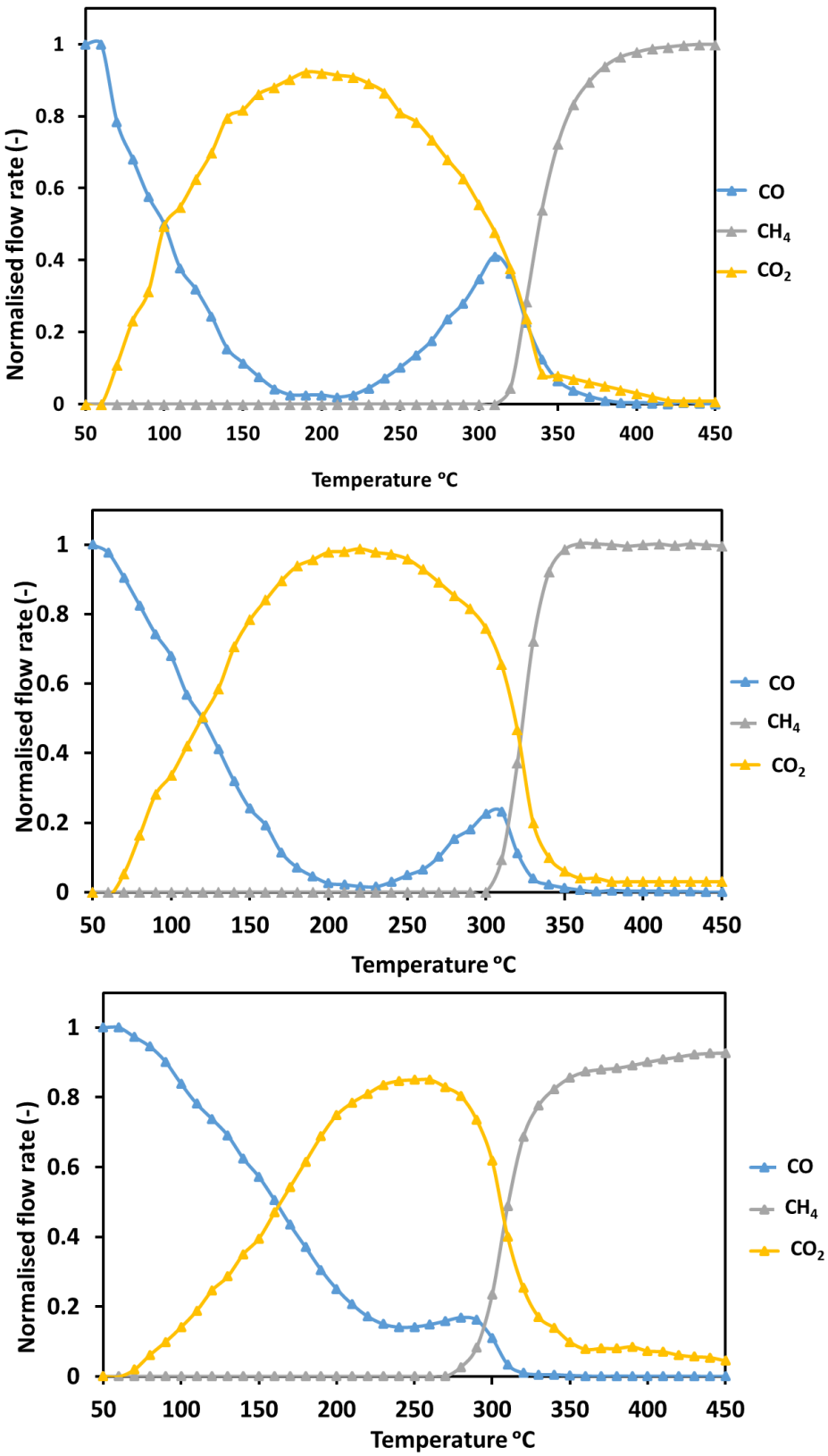

Figure 5.15: Normalised outlet flow rates of CO, CO_2, and CH_4 as a function of temperature for 0.3 wt.% MnO_x promoted catalyst (bottom), 0.5 wt.% MnO_x promoted catalyst (middle), and 1 wt.% MnO_x promoted catalyst (top).

The performance of these catalysts can be correlated to their redox properties. The addition of the promoters increases the reduction temperatures and decreases re-oxidation temperatures as discussed in the TPR/TPO sections. Good redox properties are advantageous for the Mars van Krevelen mechanism which leads to high CO conversions at lower temperatures. However, there is an optimum Co: promoter molar ratio for high CO conversion. For both the MnO_x and the FeO_x promoted catalysts the optimum ratio is 8Co: 1promoter which is similar to a study by Zhang et al. (2012). Further increase in the promoter loading decreases the conversion. This might be due to the decrease in the reducibility of the catalyst with increasing promoter loading. Studies have shown that catalysts that are harder to reduce are less effective for the Mars van Krevelen mechanism (Zhao et al.,2012; Nyathi, 2016; Fadlalla, Nyathi & Claeys, 2022). Optimum loading of the promoter ensures the extent of reduction and re-oxidation balance. Additionally, it is suggested that higher loadings of the promoter may cover the surface of Co_3O_4 nanoparticles which blocks the active sites. In a study by Zhao et al. (2012), MnO_x promoted Co_3O_4 performed better than FeO_x promoted Co_3O_4. However, we cannot compare their findings with ours since they did not specify the ratio between cobalt and the promoter.

During CO-PROX, H_2 oxidation is another competing reaction. Thus, a catalyst must also be selectivity towards CO_2 formation. During the catalytic performance evaluations, a non-stoichiometric ratio of 1:1 CO/O_2 was co-fed. This means that there might be oxygen available to oxidize H_2 thus decreasing the selectivity of CO_2 (Mishra and Prasad, 2011). Figures 5.17 and 5.18 show the CO_2 selectivity as a function of temperature for the MnO_x and FeO_x promoted catalysts respectively. At temperatures below 300 ºC, the CO_2 is dependent on the amount of the promoter added. The selectivity of the catalysts decreases with increasing temperature with the unpromoted catalyst having the lowest selectivity. The 1 wt.% MnO_x and FeO_x promoted catalysts had the highest selectively of 93 %, which decreases from 190 ºC. This shows that from 190 ºC H_2 oxidation is a competing reaction with CO-PROX. With a further temperature increase above 300 ºC, the CO_2 selectivity decreases more drastically. This is because CO methanation commences and decreases the conversion of CO to CO_2.

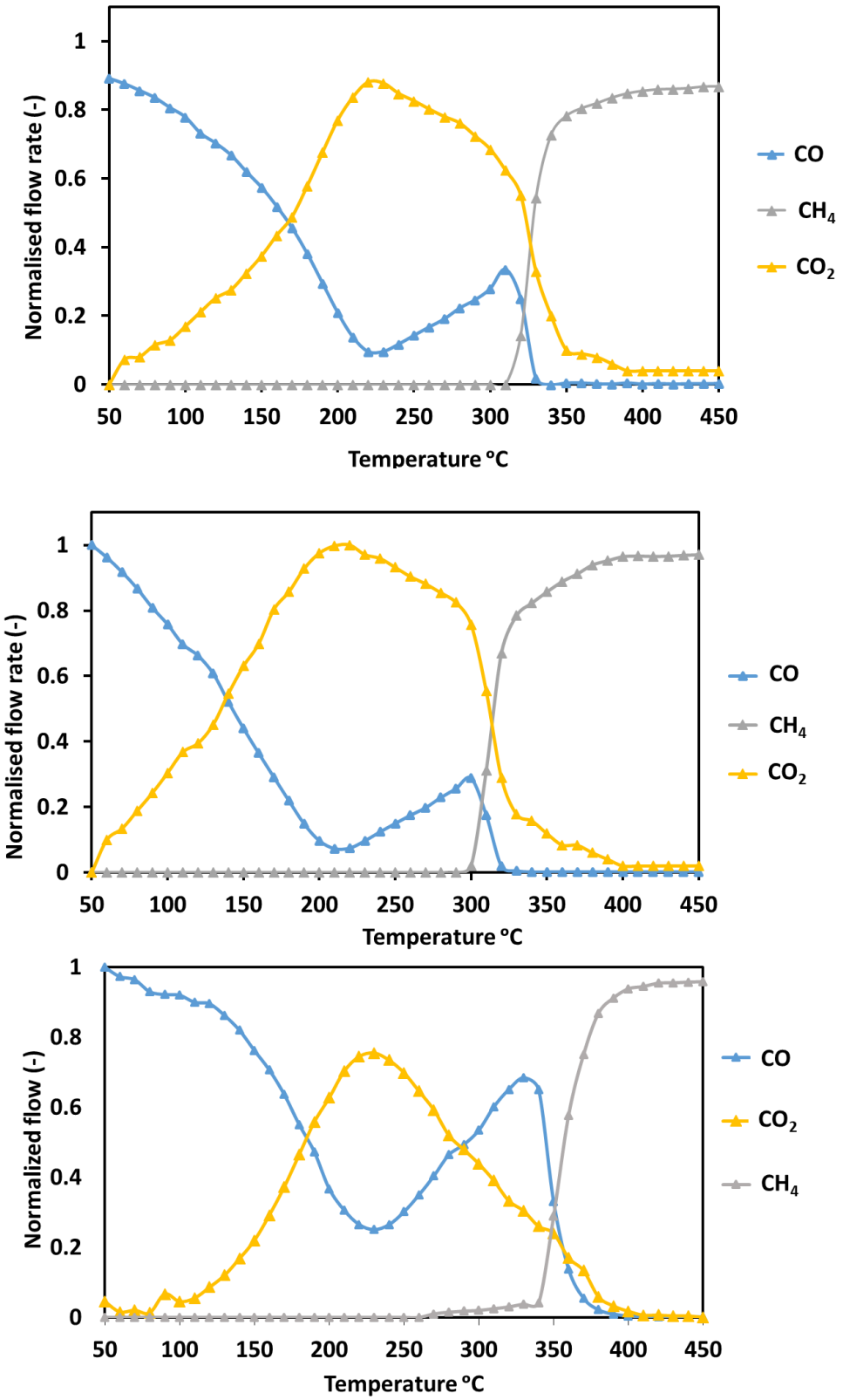

Figure 5.16: Normalised outlet flow rates of CO, CO_2, and CH_4 as a function of temperature for 0.3 wt.% FeO_x (bottom), 0.5 wt.% FeO_x (middle), and 1 wt.% FeO_x (top)

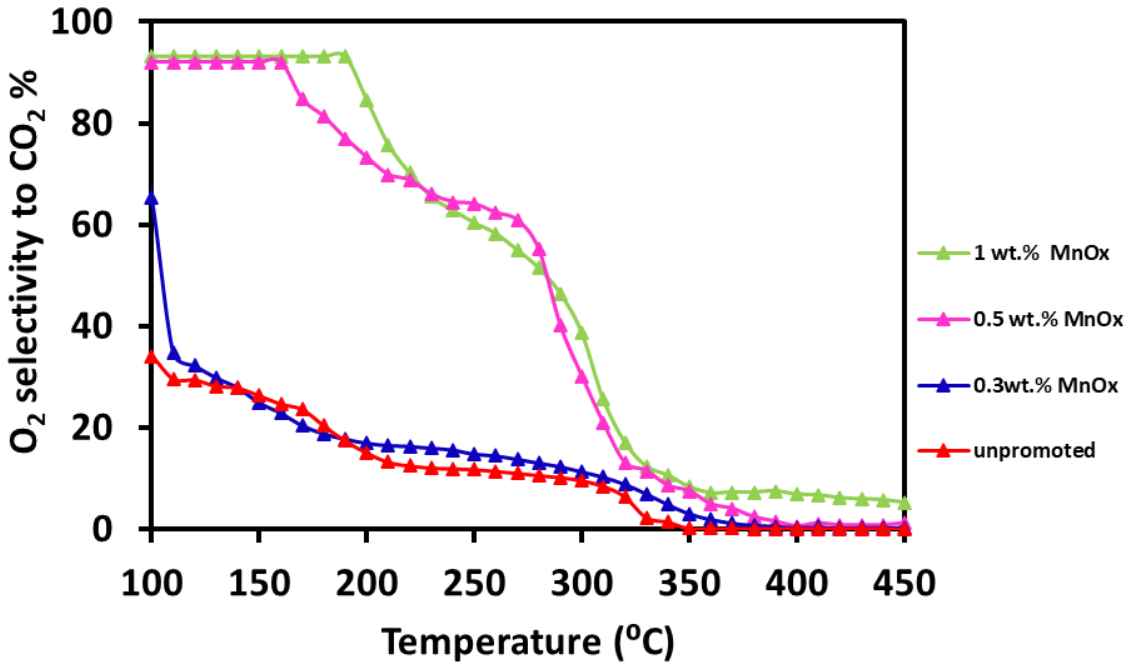

Figure 5.17: O_2 to CO_2 selectivity as a function of temperature for unpromoted and MnO_x promoted catalysts

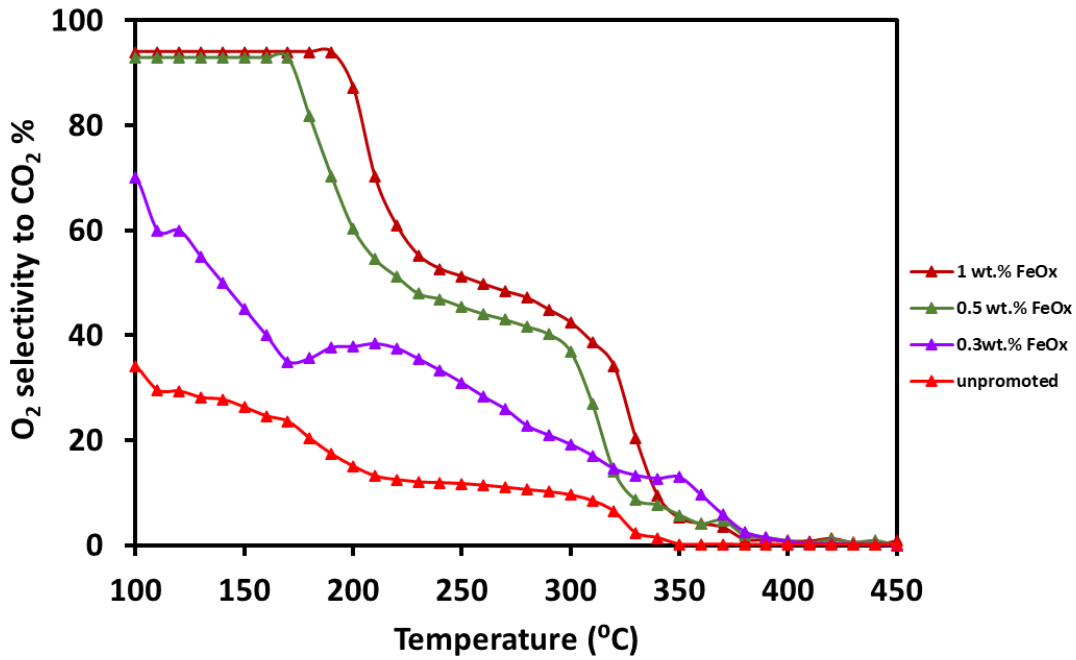

Figure 5.18: O_2 to CO_2 selectivity as a function of temperature for unpromoted and FeO_x promoted catalysts

5.3 Characterization of used catalysts

5.3.1 XRD

After the catalytic performance evaluations, the used catalysts were passivated to avoid re-oxidation. Figure 5.20 shows the XRD pattern of the MnO_x promoted catalysts. The phases, crystallite sizes, and percentages of the cobalt species present could not be determined. This was also observed in the XRD patterns of the FeO_x promoted catalysts (see in Appendix 2). This is because the sharp intense diffraction lines of silicon carbide overshadow the diffraction lines of cobalt. From the catalytic performance evaluations, we can conclude that Co_3O_4 does reduce to metallic Co as evidenced by the onset of methanation. However, for the promoted catalysts the production of CO_2 continued to occur until 450 °C even though the yield was very small. This shows that they did not fully reduce there were some active sites for CO conversion to CO_2.

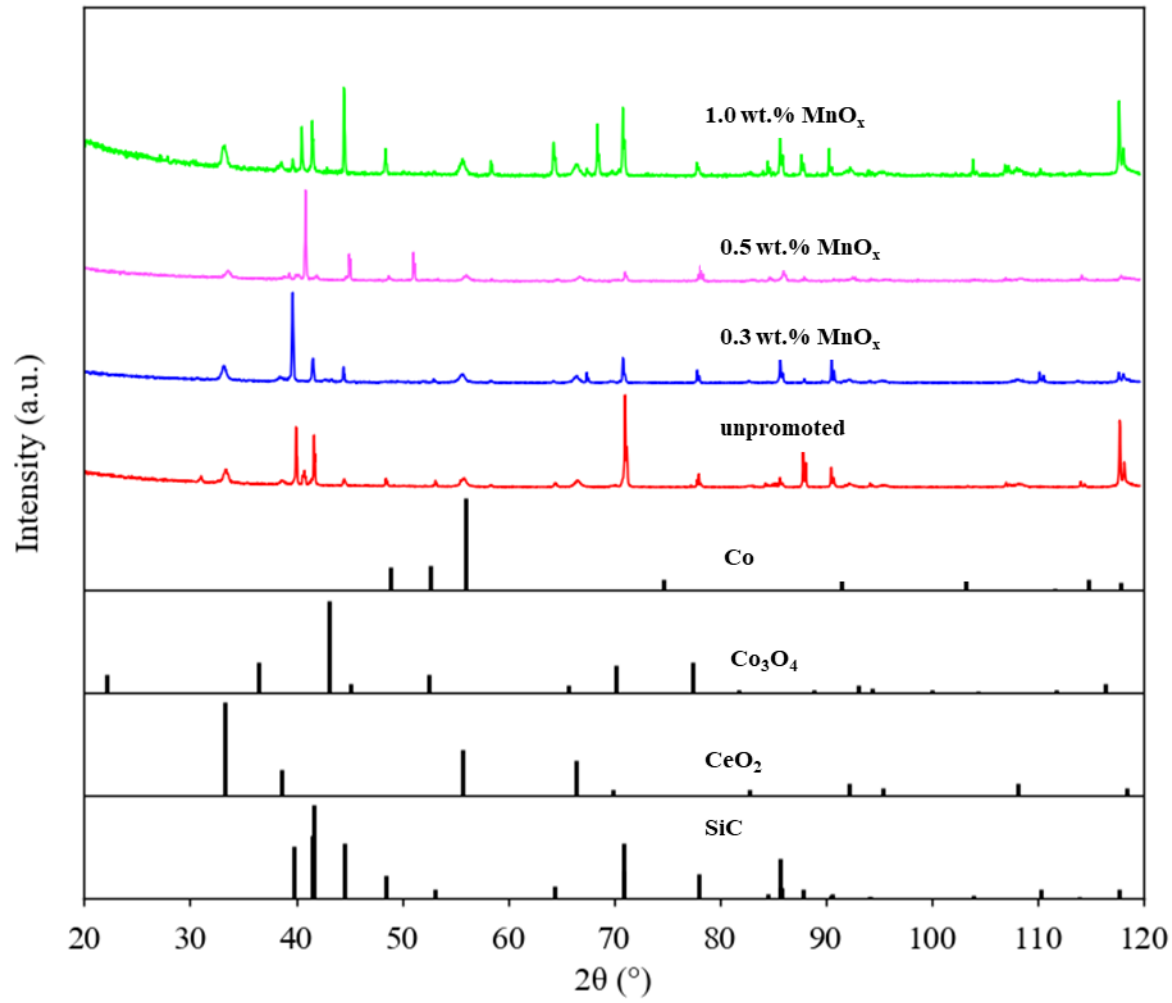

Figure 5.19: XRD patterns of used unpromoted and MnO_x promoted catalysts.

5.3.2 STEM coupled with Energy Dispersive Spectroscopy

Figure 5.20 shows the bright-field images and HAADF elemental maps for Ce, Co, Fe, or Mn of 0.3 wt.% promoted catalysts. The bright-field images of both catalysts show agglomeration of the catalysts. The signal for Co is distributed over the CeO_2 support in both catalysts. However, there are regions with higher intensity of the Co signal which might be where there is agglomeration. The signal of the promoters is evenly distributed over CeO_2 and Co.

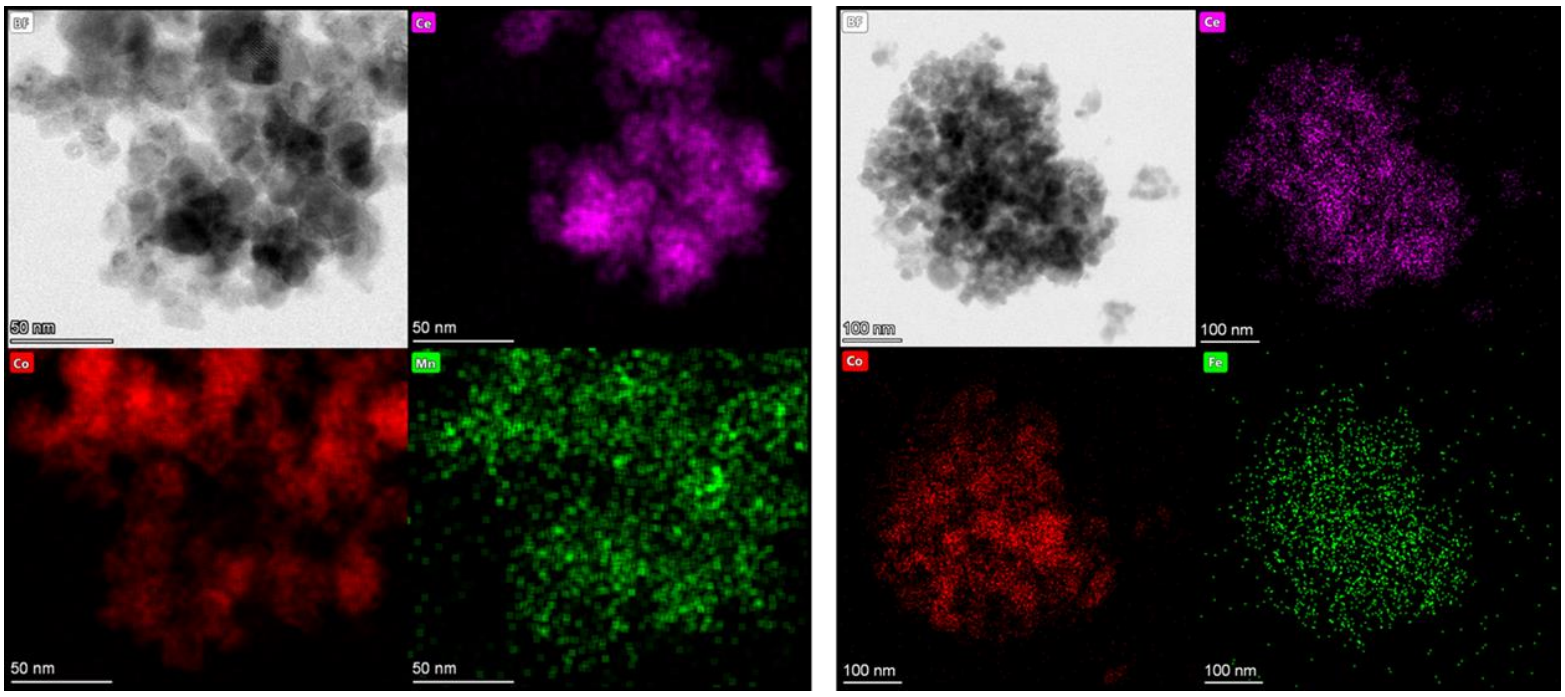

Figure 5.20:Bright-field images and High-Angle Annular Dark field elemental maps for Ce, Co, Fe, or Mn (A)0.3 wt.% MnO_x promoted catalyst (B) 0.3 wt.% FeO_x promoted catalyst.

6 Conclusion

PEMFCs are among the leading clean and sustainable energy sources. However, they require clean H_2 as their platinum anode catalyst is susceptible to CO poisoning. One of the methods for cleaning H_2 for fuel cells is CO-PROX. CO-PROX requires a catalyst that can achieve 99.99% CO conversion to CO_2 with limited H_2 oxidation. Co_3O_4 based catalysts are among the most active catalysts for CO-PROX, however, at temperatures above 225 °C they deactivate via reduction to Co^0 which is active for CO methanation. Hence, the influence of promoters on the stability of the Co_3O_4 phase at high temperatures is an area of interest.

The current study investigated the effect of MnO_x and FeO_x promoters on Co_3O_4/CeO_2 during CO-PROX. The effects of different loadings of the promoters on the stability, activity, selectivity were investigated. The solvothermal method was used to synthesize Co_3O_4 nanoparticles. This method results in monodispersed nanoparticles. The nanoparticles were promoted and supported via ultrasonication-assisted wet impregnation. After the synthesis the samples were characterized via TEM, XRD, STEM coupled with elemental mapping, ICP-OES, and Temperature programmed reactions. The catalytic performance evaluations were performed at a temperature range of 50-450 °C. To investigate the effect of the promoters on the stability of Co_3O_4 at high temperatures

It was oberserved that the Co_3O_4 crystallite size increases when the nanoparticles are supported and this is due to calcination. Guo and Liu (2008) studied the effect of calcination temperature on the catalytic performance of Co_3O_4/CeO_2 and found that the activity decreased with increasing temperature. The decrease in activity was attributed to the sintering as a result of decrease in surface area due to increasing calcination temperature.

For MnO_x promoted catalyst the 0.5 wt.% promoted catalyst achieved the highest CO conversion of 98.8 % from 210-230 °C. For FeO_x promoted catalysts also the 0.5 wt.% promoted achieved the highest CO conversion of 100% from 220- 230 °C. Additionally, the temperature for the onset of CO methanation increased with the addition of promoters. For the catalysts loaded with 1 wt.% of the promoters, the onset temperature was 310 °C, whereas for the unpromoted catalysts and catalysts with low promoter loading the onset temperature was 275 °C. This shows that the addition of the correct ratio of promoters improves the activity and stability of Co_3O_4 during CO-PROX. Catalysts promoted with 1 wt.% are harder to reduce which leads to the late onset of CO methanation. However, we also see a decrease in the maximum CO conversion achieved by these catalysts. Catalysts that are harder to reduce result in a less effective Mars-van Krevelen mechanism. A balance in the extent of reduction and re-oxidation for highly active and selective CO-PROX catalyst because if it reduces too quickly then it deactivates.

The CO_2 selectivity of the promoted catalysts was higher than that of the unpromoted catalyst. The 1 wt.% promoted catalyst achieved the highest of 93%, which decreased from 190 ºC indicating that H_2 oxidation was a competing reaction.

7 Recommendations

- To prevent sintering of Co_3O_4 nanoparticles we can calcine at lower temperatures for a longer period of time.
- The dispersion of Co_3O_4 can be improved by changing the solvent from ethanol to water during the impregnation. Additionally, the volume of the solvent can be increased.
- In industry, the reformate gas from WGS contains H_2O and CO_2. Therefore, it would be beneficial to conduct this study in the presence of H_2O and CO_2 to simulate for real-life application
- It has been hypothesized that there is an electron transfer between the promoters and Co_3O_4 which prevents the reduction of cobalt. Thus, conducting the catalytic performance evaluations in-situ XPS would be beneficial to monitor the changes in the oxidation states of the promoters and Co_3O_4 during CO-PROX.
- The 0.5 wt. % FeO_x achieved 100 % CO conversion and 93 % CO_2 selectivity which makes it a good catalyst CO-PROX industrial application. Conducting a time-on stream of 100 hours experiment at 210 ºC would give insight into the stability of this catalyst.
- During the synthesis, the distribution of the promoter can be limited to Co_3O_4 nanoparticles by first adding the promoter to Co_3O_4 and then dry and calcine. Then supporting the calcined promoted Co_3O_4.

8 References

Arango-Diaz, A., Cecilia, A.J., Marrero-Jerez, J., Nuñez, P., Jiménez-Jiménez, J. & Rodríguez-Catellón. 2016. Freeze-dried Co_3O_4-CeO_2 catalysts for the preferential oxidation of CO with the presence of CO_2 and H_2O in the feed. *Ceramics International*. 42(6): 7462-7474

Argyle, M. D. & Bartholomew, C. H. 2015. Heterogeneous catalyst deactivation and regeneration: A review. *Catalysts*. 5(1): 145-269

Avgouropoulosa, G., Ioannidesa,T., Matralisa, K.H., Batista, J. & Hocevar, S. 2001. CuO-CeO_2 mixed oxide catalysts for the selective oxidation of carbon monoxide in excess hydrogen. *Catalysis Letters*. 72(1): 33-40

Bao, T., Zhao, Z., Dai, Y., Lin, X., Jin, R., Wang, G. & Muhammad, T. 2012. Supported Co_3O_4-CeO_2 catalysts on modified activated carbon for CO preferential oxidation in H2-rich gases. *Applied Catalysis B: Environmental*. 119-120: 62-73

Bartholomew, C.H. 2001. Mechanisms of Catalyst Deactivation. *Applied Catalysis A: General*. 212: 16-70

Beck, A., Yang, A., Leland, A.R., Riscoe, A., Lopez, A.F., Goodman, E.D. & Cargnello, M. 2018. Understanding the Preferential Oxidation of Carbon Monoxide (PrOx) Using Size-Controlled Au Nanocrystal Catalyst. *American Institute of Chemical Engineers*. 1- 45

Bičáková, O. and Straka, P. 2010. The resources and methods of hydrogen production. *Acta Geodyn. Geomater*. 7(2): 175-188

Broqvist, P., Panas, I. & Persson, H. 2002. A DFT study on CO oxidation over Co_3O_4. *Journal of Catalysis*. 210(1): 198-206

Büyüközkan, G., Karabulut, Y. & Mukul, E. 2018. A novel renewable energy selection model for United Nations' sustainable development goals. *Energy*.165 (1): 290-3012.

Campanati, M., Fornasari, G. & Vaccari, A. 2003. Fundamentals in the preparation of heterogeneous catalysts. *Catalysis Today*. 77 (4): 299-314

Chin, S.Y., Alexeev, O.S. & Amiridis, M.D. 2005. Preferential oxidation of CO under excess H_2conditions over Ru catalysts. *Applied Catalysis A: General*. 157-166

Dagle, R.A, Wang, Y., Xia, G., Strohm, J.J., Holladay, J. & Palo, D.R. 2007. Selective CO methanation catalysts for fuel processing applications. *Applied Catalysis A: General*. 326: 213-218

Deshmukh, R. & Niederberger, M. 2017. Mechanistic Aspects in the Formation, Growth and Surface Functionalization of Metal Oxide Nanoparticles in Organic Solvents. *Chemistry-A European Journal* 23(36): 8542-8570

Di, L., Wu, G., Dai, W., Guan, N. & Li, L. 2015. Ru/TiO_2 for the preferential oxidation of CO in H_2-rich stream: Effects of catalyst pre-treatments and reconstruction of Ru sites. *Fuel*. 143: 318-326

Echigo, M. & Tabata, T. 2004. CO removal form reformed gas by catalytic methanation for polymer electrolyte fuel cell applications. *Journal of Chemical engineering in Japan*. 37(1): 75-81

Edwards, P.P., Kuznetsov, V.L., David, W.I.F, & Brandon, N.P. 2008. Hydrogen and fuel cells: Towards a sustainable energy future. *Energy policy*. 36 (1): 4356-4362

Fischer, N. 2011. Preparation of nano- and Ångstrøm-sized cobalt ensembles and their performance in the Fischer-Tropsch synthesis. Ph.D. Thesis. University of Cape Town, South Africa

Fischer, N., van Steen, E. & Claeys, M. 2011. Preparation of supported nano-sized cobalt oxide and fcc cobalt crystallites. *Catalysis Today*. 171(1):174-179

Forzatti, P. & Lietti, L. 1999. Catalyst deactivation. *Catalysis Today*. 52: 165-181

Fu, Y., Tian, Y. & Lin, P. 1991. Low-Temperature IR Spectroscopic Study of Selective Adsorption of NO and CO on $CuO/\gamma\text{-}Al_2O_3$. *Journal of Catalysis*. 132: 85-91

Gamarra, D. & Martínez-Arias, A. 2009. Preferential oxidation of CO in rich H_2 over CuO/CeO_2: Operando-DRIFTS analysis of deactivating effect of CO_2 and H_2O. *Journal of Catalysis*. 263(1): 189-195

Gamarra, D., Belver, C., Fernández-García, M. & Martínez-Arias, A. 2007. Selective CO Oxidation in Excess H_2 over Copper-Ceria Catalysts: Identification of Active Entities/Species. *Journal of the American Chemical Society*. 129(40): 12064-12065

Gamarra, D., Munuera, G., Hungría, B.A., Fernández-García, M., Conesa, J.C., Midgley, A.P., Wang, Q.X. & Hanson, J.C. et al. 2007. Structure−Activity Relationship in Nanostructured Copper−Ceria-Based Preferential CO Oxidation Catalysts. *Journal of the Physical Chemistry*. 111(29): 11026-11038

Gawade, P., Bayram, B., Alexander, A.M. & Ozkan, U. 2012. Preferential oxidation of CO (PROX) over CoO_x/CeO_x in hydrogen-rich streams: Effect of cobalt loading. *Applied Catalysis B: Environmental.* 128 (1): 21-30

Giorgi, L. and Leccese, F. 2013. Fuel Cells: Technologies and Applications. *The Open Fuel Cells Journal*. 6: 1-20

Grisel, R., Weststrate, K., Gluhoi, A. & Nieuwenhuys. E.B. 2002. Catalysis by Gold nanoparticles. *Gold Bulletin*. 35 (2): 39-45

Grzybek, G., Ciura, K., Gryboś, J., Indyk, P., Davó-Quiñonero, A., Lozano-Castelló, D., Bueno-Lopez, A. & Kotarba, A. et al. 2019. *Journal of Physical Chemistry*. 123: 20221-20232

Guczi, L., Beck, A. & Frey, K. 2009. Role of promoting oxide morphology dictating the activity of Au/SiO_2 catalyst in CO oxidation. *Gold Bulletin*. 42(1): 5-12

Guo, Q and Liu, Y. 2008. Preferential oxidation of CO in H_2 over $Co_3O_4\text{-}CeO_2$ catalysts. *Reaction Kinetics Catalyst Letter*. 92(1): 19-25

Han, Y.F., Kahlich, M.J., Kinne, M. & Behm, R.J. 2004. CO removal from realistic methanol reformate via preferential oxidation-performance of a Rh/MgO catalyst and comparison to $Ru/\gamma\text{-}Al_2O_3$, and $Pt/\gamma\text{-}Al_2O_3$. *Applied Catalysis B: Environmental*. 50: 209-218

Hansen, W.T., Wagner, B.J., Hansen, L.P., Dahl, S., Topsøe, H. & Jacobsen, J.C. 2001. Atomic-Resolution in Situ Transmission Electron Microscopy of a Promoter of a Heterogeneous Catalyst. *Science*. 294(5546): 1508-1510

Haryanto, A., Fernando, S., Murali, N. & Adhikari, S. 2005. Current status of hydrogen production techniques by steam reforming of ethanol: A review. *Energy Fuels.* 19 (5): 2098-2106

Hernández, A.J., Gómez, A.S., Zepeda, A.T., Fierro-González, C.J. & Fuentes, A.G. 2015. Insight into the Deactivation of Au/CeO_2 Catalysts Studied by In Situ Spectroscopy during the CO-PROX Reaction. *ACS Catalysis*. 5(7): 4003-4012

Holladay, J.D., Hu, J., King, D.L. & Wang, K. 2009. An overview of hydrogen production technologies. *Catalysis Today*. 139 (1): 244-260.

Hu, L., Peng, Q. & Li, Y. 2008. Selective Synthesis of Co_3O_4 Nanocrystal with Different Shape and Crystal. *Journal of the American Chemical Society*. 16136–16137

Hu, L., Sun, K., Peng, Q., Xu, B. & Li, Y. 2010. Surface active sites on Co_3O_4 nanobelt and nanocube model catalysts for CO oxidation. *Nano Research.* 3: 363–368

Huang, C., Chen, Y., Su, C. & Hsu, C. 2007. The cleanup of CO in hydrogen for PEMFC applications using Pt, Ru, Co, and Fe in PROX reaction. *Journal of Power Sources*. 174: 294-301

Igarashi, H., Uchida, H., Suzuki, M., Sasaki, Y. & Watanabe, M. 1997. Removal of carbon monoxide from hydrogen-rich fuels by selective oxidation over platinum catalyst supported on zeolite. *Applied Catalysis A: General*. 159 (1): 159-169

Ivanova, S., Pitchon, V., Petit, C. and Caps, V. 2010. Support Effects in the Gold Catalyzed PROX Reaction. *ChemCatChem.* 2: 566-563

Jansson J., Palmqvist A.C., Fridell E., Skoglundh M., Osterlund L., Thormahlen P. & Langer V. 2000. On the catalytic activity of Co_3O_4 in Low-Temperature CO oxidation. *Journal of catalysis.* 211(2): 387-397

Kahlich, M.J., Gasteiger, H.A. & Behm, R.J. 1997. Kinetics of the selective low temperature oxidation of CO in H_2 rich gas over Au/α-Fe_2O_3. *Journal of Catalysis*. 182: 430-440

Khasu, M. 2016. In situ study of Co_3O_4 morphology in the CO-PROX reaction. MSc. Thesis. University of Cape Town. South Africa

Khasu, M., Nyathi, T., Morgan, D.J., Hutchings, J.G., Claeys, M. & Fischer, N. 2017. Co_3O_4 morphology in the preferential oxidation of CO. *Catalysis & Technology*. 1-32

Kim, Y. H., Park, E. D., Lee, H. C. & Lee, D. 2009. Selective CO removal in a H_2-rich stream over supported Ru catalysts for the polymer electrolyte membrane fuel cell (PEMFC). *Applied Catalysis A: General*. 366(2): 363-369

Ko, B.J. & Kim, H.D. 2004. Preparation and reactivity of mixed metal oxide for selective oxidation of carbon monoxide in hydrogen mixtures. *Solid State Ionics*. 323-327

Konsolakis, M., Sgourakis, M. & Carabineiro, A.C. 2015. Surface and redox properties of cobalt–ceria binary oxides: On the effect of Co content and pretreatment conditions. *Applied Surface Science*. 314: 48-54

Kotobuki, M., Watanabe, A., Uchida, H., Yamashita, H. & Watanabe, M. 2005. Development of Pt/ZSM-5 Catalyst with High CO Selectivity for Preferential Oxidation of Carbon Monoxide in a Reformed Gas. *Chemistry Letters*. 34(6): 866-867

Kozlov, A., Kim, D.H., Yezerets, A., Andersen, P., Kung H. & Kung M. 2002. Effect of preparation method and redox treatment on the reducibility and structure of supported ceria-zirconia mixed oxide. *Journal of catalysis*. 209 (2): 417-426

Lakshmanan, P., Park, J.E. & Park, E.D. 2014. Recent Advances in Preferential Oxidation of CO in H_2 over Gold Catalysts. *Catalysis Survey from Asia*. 18: 75-88

Li, Z., Mi, W., Gong, J., Lu, Z., Xu, L. & Su, Q. 2008. CO removal by two stage methanation for polymer electrolyte fuel cell. *Journal of Natural Gas Chemistry*. 17(4): 359-364

Lipman, T.E and Weber, A.Z. 2018. Fuel Cells and Hydrogen Production. *A volume in the Encyclopedia of Science and Technology.* 1182

Liu, C., Gong, L., Lu, M., Sun, T., Dai, R., Liu, Q., Huang, X., Liu, G. & Huang, Z. 2017. The Solid-State-Grinding Synthesis of Manganese-Modified Cobalt Oxides and Application in the Low-Temperature CO Preferential Oxidation in H_2-Rich Gases. *Catalysis Survey Asia*. 21: 175-184

Liu, C., Liu, Q., Bai, L., Dong, A., Liu, G. & Wen, S. 2013. Structure and catalytic performances of nanocrystalline Co_3O_4 catalysts for low temperature CO oxidation prepared by dry and wet synthetic routes. *Journal of Molecular Catalysis A: Chemical*. 370:1-6

Liu, K., Song, C. & Subramani, V. 2010. Hydrogen and Syngas Production and Purification Technologies. *John Wiley and Sons*

Liu, Z., Zhou, R. & Zheng, X. 2007. Comparative study of different methods of preparing CuO-CeO_2 catalysts for preferential oxidation of CO in excess hydrogen. *Journal of Molecular Catalysis A: Chemical*. 267(1-2): 137-142

Luengnaruemitchai, A., Osuwan, S. & Gulari, E. 2014. Selective catalytic oxidation of CO in the presence of H_2 over gold catalyst. *International Journal of Hydrogen Energy*. 29(4): 429-435

Lukashuk, L., Föttinger, K., Kolar, E., Rameshan, C., Teschner, D., Hävecker, M., Knop-Gericke, A. & Yigit, N. et al. 2016. Operando XAS and NAP-XPS studies of preferential CO oxidation on Co_3O_4 and CeO_2-Co_3O_4 catalysts. *Journal of Catalysis*. 344: 1-15

Majlan, H.E., Daud, W.R., Iyuke, E.S., Mohamad, B.A., Kadhum, A.A., Mohammad, W.A., Takriff, M. & Bhaman, N. 2009. Hydrogen purificiation using compact pressure swing adsorption system for fuel cell. *International Journal of Hydrogen Energy*. 34: 2771-2777

Mavrikakis, M., Stoltze, P. & Norskøv, J. 2000. Making gold less noble. *Catalysis Letters*. 64 101–106

Mishra, A. and Prasad, P. 2011. A review on preferential oxidation of Carbon monoxide in hydrogen rich gases. *Bulletin of Chemical Reaction Engineering & Catalysis*. 6(1): 1-14

Niederberger, M. & Garnweitner, G. 2006. Organic Reaction Pathways in the Nonaqueous Synthesis of Metal Oxide Nanoparticles. *Chemistry-A European Journal* 12(28): 7282-7302

Nyathi, M.T. 2016. Preferential Oxidation of Carbon Monoxide in Hydrogen-rich Gases over Supported Cobalt Oxide Catalysts. MSc. Thesis. University of Cape Town, South Africa

Nyathi, M.T., Fischer, N., York, P.E.A. & Claeys, M. 2017. Effect of crystallite size on the performance and phase transformation of Co_3O_4/Al_2O_3 catalysts during CO-PROX- an in situ study. *Faraday Discussions*. 197: 269-285

Nyathi, M.T., Fischer, N., York, E.P.A. & Claeys. 2020. Environment-Dependent Catalytic Performance and Phase Stability of Co3O4 in the Preferential Oxidation of Carbon Monoxide Studied In Situ. *ACS Catalysis*. 10(20): 11892-11911

Ockwig, N.W. & Nenoff, M.T. 2007. Membranes for hydrogen separation. *Chemical Reviews*. 107(10): 4078-4110

Oh, S.H. & Sinkevitch, R.M. 1993. Carbon Monoxide Removal from Hydrogen-Rich Fuel Cell Feedstreams by Selective Catalytic Oxidation. *Journal of Catalysis*. 142: 254-262

Omata K., Takada T., Kasahara S. & Yamada M. 1996. Active site of substituted cobalt spinel oxide for selective oxidation of CO/H_2: Part II. *Applied Catalysis A: General*. 146: 255-267

Park, E.D., Lee, D. & Lee, H.C. 2009. Recent progress in selective CO removal in H_2 rich stream. *Catalysis Today*. 139: 280-290

Peterson, A.P. 2018. Alumina-modified cobalt catalysts for the Fischer-Tropsch synthesis. Ph.D. Thesis. University of Cape Town. South Africa

Pinna, N., Grancharov, S., Beato, P., Bonville, P., Antonietti, M. & Niederberger, M. 2005. Magnetite Nanocrystals: Nonaqueous Synthesis, Characterization, and Solubility. *Chemistry of Materials*. 17(11): 3044-3049

Quinet, E., Piccolo, L., Morfin, F., Avenier, P., Diehl, F., Caps, V. & Rousset, J. 2009. On the mechanism of hydrogen-promoted gold catalysed CO oxidation. *Journal of Catalysis*. 268: 384-389

Ratnasamy, P., Srinivas, D., Satyanarayana, V.C., Manikandan, S.R., Kumaran, S., Sachin, M. & Shetti, N.V. 2004. Influence of the support on the preferential oxidation of CO in hydrogen-rich steam reformates over the CuO–CeO_2–ZrO_2 system. *Journal of Catalysis*. 221(2): 455-465

Relvas, F., Whitley, R.D., Silva, C. & Mendes, A. 2018. Single stage pressure swing adsorption for producing fuel cell grade hydrogen. *Industrial & Chemical Research*. 57: 5106-5118

Rodrigues, A., Amphlett, J.C., Mann, R.F., Peppley B.A & Roberge, P.R. 1997. Carbon monoxide poisoning of proton-exchange membrane fuel cells. *IECEC-97 Proceedings of the Thirty-Second Intersociety Energy Conversion Engineering Conference.* 2: 768-773

Schubert, M., Plzak, V., Garche, J. & Behm, J. 2001. Activity, selectivity, and long-term stability of different metal oxide supported gold catalysts for the preferential CO oxidation in H_2-rich gas. *Catalysis Letters*. 76(3-4): 143-150

Sewell, G.S van Steen, E. & O'Connor, C.T. 1995. Use of TPR/TPO for characterization of supported catalysts. *Catalysis Letters*. 37: 255-260

Shiri, S.M.Z., Henderson, W. & Mucalo, M. 2019. A Review of The Lesser-Studied Microemulsion-Based Synthesis Methodologies Used for Preparing Nanoparticle Systems of The Noble Metals, Os, Re, Ir, and Rh. Materials. 12: 1-26

Sircar, S. & Golden, T.C. 2000. Purification of hydrogen by pressure swing adsorption. *Separation Science and Technology*. 35(5): 667-687

Snytnikov, P.V., Sobyanin, V.A., Belyaev, V.D., Tsyrulnikov, P.G., Shitova, N.B. & Shlyapin, D.A. 2003. Selective oxidation of carbon monoxide in excess hydrogen over Pt, Ru, and Pd supported catalysts. *Applied Catalysis A: General*. 239: 149-156

Su, D., Dou, S. & Wang, G. 2014. Single Crystalline Co_3O_4 Nanocrystals Exposed with Different Crystal Planes for Li-O_2 Batteries. *Scientific Reports*. 4 (5767): 1-5

Takenaka, S., Shimizu, T. & Otsuka, K. 2004. Complete removal of carbon monoxide in hydrogen-rich gas stream through methanation over supported metal catalysts. International Journal of Hydrogen Energy. 28 (10): 1065-1073

Teng, Y., Kusano, Y., Azuma, M., Haruta, M. & Shimakawa, Y. 2011. Morphology effects of Co_3O_4 nanocrystals catalysing CO oxidation in a dry reactant gas stream. *Catalysis Science & Technology*. 1(6): 920-922

Trovarelli, A. 1999. Structural and Oxygen Storage/Release Properties of CeO_2-Based Solid Solutions. *Comments on Inorganic Chemistry*. 20(4-6): 263-284

Valden, M., Lai, X. & Goodman, W. 1998. Onset of Catalytic Activity of Gold Clusters on Titania with the Appearance of Nonmetallic Properties. *Science*. 281: 1647-1650

Van Steen, E. & Claeys, M. 2008. Fischer-Tropsch Catalysts for the Biomass-to-Liquid (BTL)- Process. *Chemical Engineering & Technology*. 31(5): 655-666

Wang, F., Büchel, R., Savitsky, A., Zalibera, M., Widmann, D., Pratsinis, E.S., Lubitz, W. & Schüth, F. 2016. In Situ EPR Study of the Redox Properties of CuO−CeO_2 Catalysts for Preferential CO Oxidation (PROX). *ACS Catalysis*. 6: 3520-3530

Wolf, M., Mutuma, K.B., Coville, N.J., Fischer, N. & Claeys, M. 2018. Role of CO in the Water-Induced Formation of Cobalt Oxide in a High Conversion Fischer–Tropsch Environment. *ACS Catalysis*. 8(5): 3985-3989

Woods, P., Gawade, P., Tan, B. & Ozkan, U. 2010. Preferential oxidation of carbon monoxide on Co/CeO_2. *Applied Catalysis B: Environmental.* 97: 28-35

Wootsch, A., Descorme, C. & Duprez, D. 2004. Preferential oxidation of carbon monoxide in the presence of hydrogen (PROX) over ceria–zirconia and alumina-supported Pt catalysts. *Journal of Catalysis.* 225(2): 259-266

Worner, A., Friedrich, C. & Tamme, R. 2003. Development of a Ru-bases catalyst system for selective oxidation of CO in hydrogen rich gas. *Applied Catalysis A: General.* 245(1): 1-14

Yáñez-Vilar, S., Sánchez-Andújar, M., Gómez-Aguirre, C., Mira, J., Señarís-Rodrígueza, A.M. & Castro-García, S. 2009. A simple solvothermal synthesis of MFe_2O_4 (M=Mn, Co and Ni) nanoparticles. *Journal of Solid State Chemistry*. 182(10): 2685-2690

Yang, S., Choi, D., Jang, S., Kim, A. & Choi, D. 2008. Hydrogen separation by multi-bed pressure swing adsorption of synthesis gas. *Adsorption.* 14: 582-590

Yong, L. & Wenjie, S. 2012. Morphology-dependent nanocatalysis on metal oxides. *Science China Chemistry*. 55(12): 2485-2496

Zhang, Q., Liu, X., Fan, W. & Wang, Y. 2012. Manganese-promoted cobalt oxide as efficient and stable non-noble metal catalyst for preferential oxidation of CO in H_2 stream. *Applied Catalysis B: Environmental*. 102: 207-214

Zhao, Z., Lin, X., Jin, R., Dai, Y. & Wang, G. 2011. High catalytic activity in CO PROX reaction of low cobalt-oxide loading catalysts supported on nano-particulate CeO_2-ZrO_2 oxides. *Catalysis Communications*. 12(15): 1448-1451

Zhao, Z., Lin, X., Jin, R., Dai, Y. & Wang, G. 2012. Improvement of nano-particulate $Ce_xZr_{1-x}O_z$ composite oxides supported cobalt oxide catalysts for CO preferential oxidation in H_2-rich gas. *Catalysis Science & Technology*. 2: 555-563

Zhao, Z., Lin, X., Jin, R., Wang, G. & Muhammad, T. 2012. MOx (M = Mn, Fe, Ni or Cr) improved supported Co_3O_4 catalysts on ceria–zirconia nanoparticulate for CO preferential oxidation in H_2-rich gases. *Applied Catalysis B: Environmental*. 115-116: 53-62

Zhao, Z., Yung, M. & Ozkan, U. S. 2008. Effect of support on the preferential oxidation of CO over cobalt catalysts. *Catalysis Communications*. 9(6): 1465-1471

9 Appendices

Appendix 1

Calibrations

Mass flow controllers

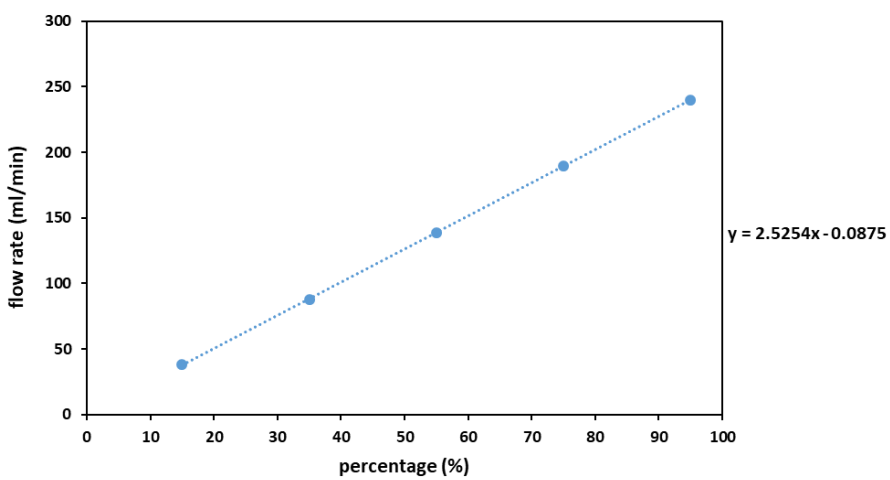

Figure 9.1: Calibration curve for MFC controlling the inlet gas mixture (CO, H_2, and N_2).

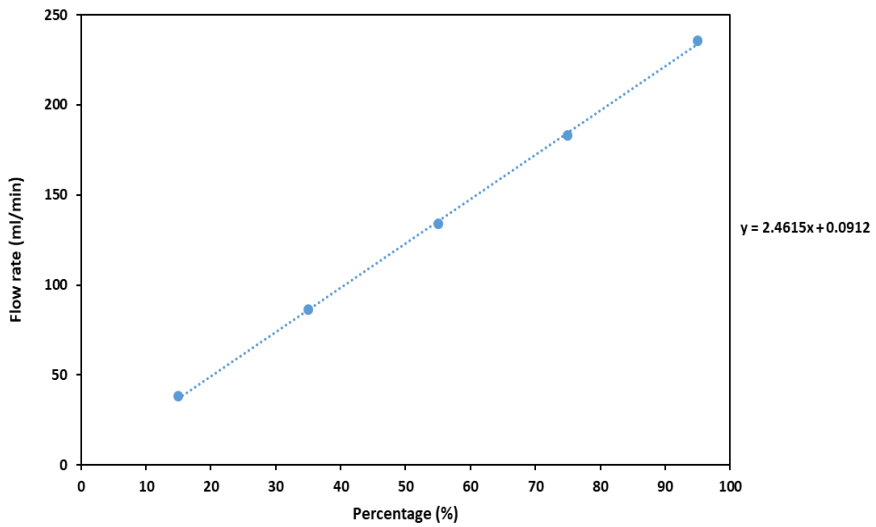

Figure 9.2: Calibration curve for MFC controlling the inlet O_2.

Gas Chromatogram

Table 9.1: Response factors of gasses in gas mixture used for GC calibration.

	H_2	N_2	CH_4	CO_2	CO
Volume (%)	40.2	5.1	14.3	10.2	20
Average area of 30 peaks	25514.7	348.5	827.2	253.6	1246.5
Response factor (Rf)	0.11	1.00	1.18	2.75	1.10

Table 9.2: Response factors of O_2 during GC calibration.

	O_2	N_2
Volume (%)	21	79
Average area of 30 peaks	1000.6	4324
Response factor (Rf)	1.15	1.00

Appendix 2

Characterization results

TEM

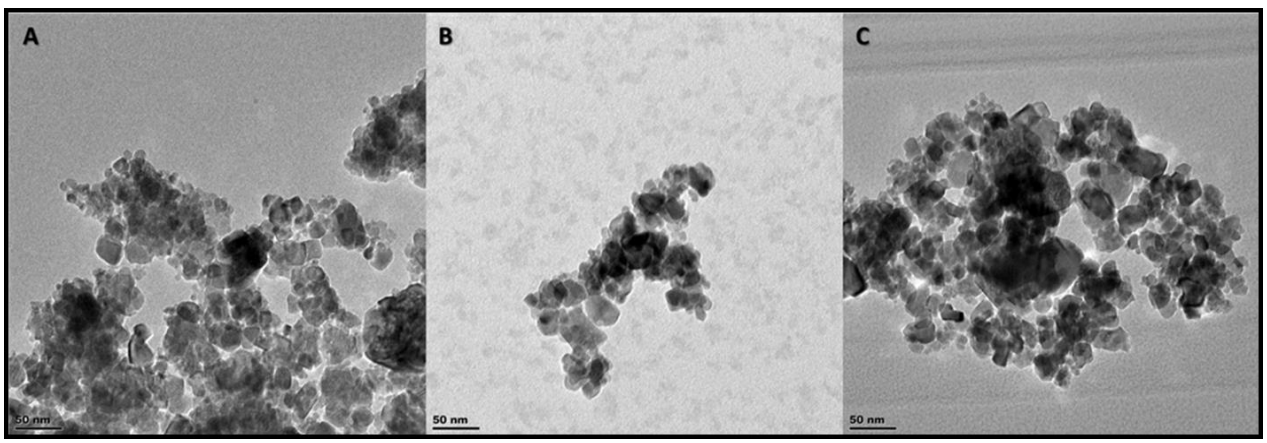

Figure 9.3: TEM images of MnO_x-promoted catalysts. (A) 0.3 wt.% MnO_x (B) 0.5 wt.% MnO_x , and (C) 1 wt.% MnO_x.

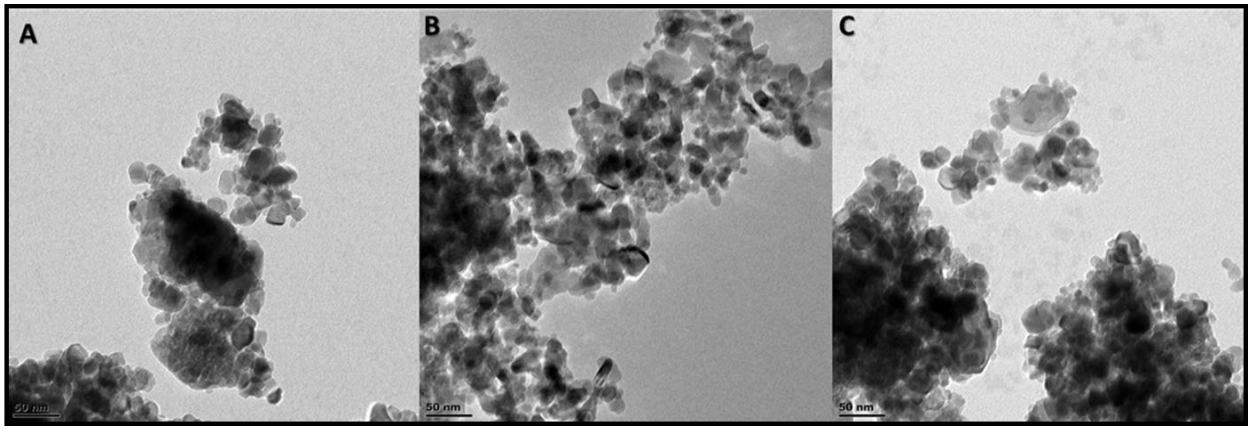

Figure 9.4: TEM images of FeO_x-promoted catalysts. (A) 0.3 wt.% FeO_x, (B) 0.5 wt.% FeO_x, and (C) 1 wt.% FeO_x.

Elemental mapping

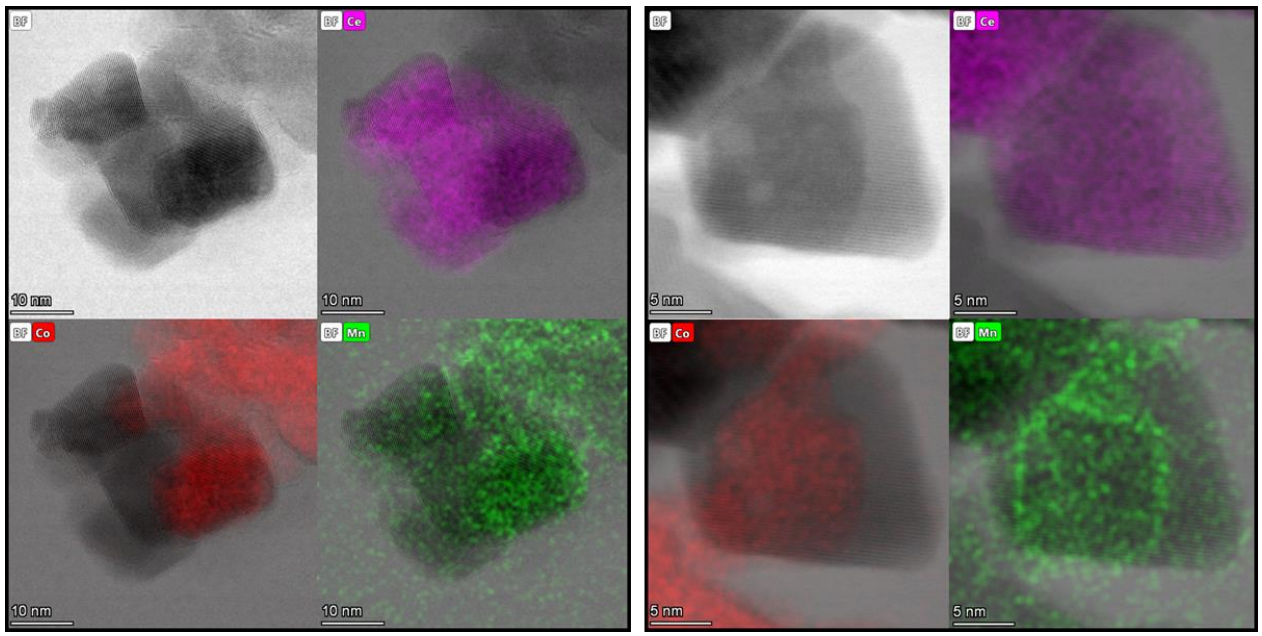

Figure 9.5: Bright field STEM image and elemental maps of Ce, Co, and Mn for (a) 0.5 wt.% MnO_x (b) 1 wt.% MnO_x.

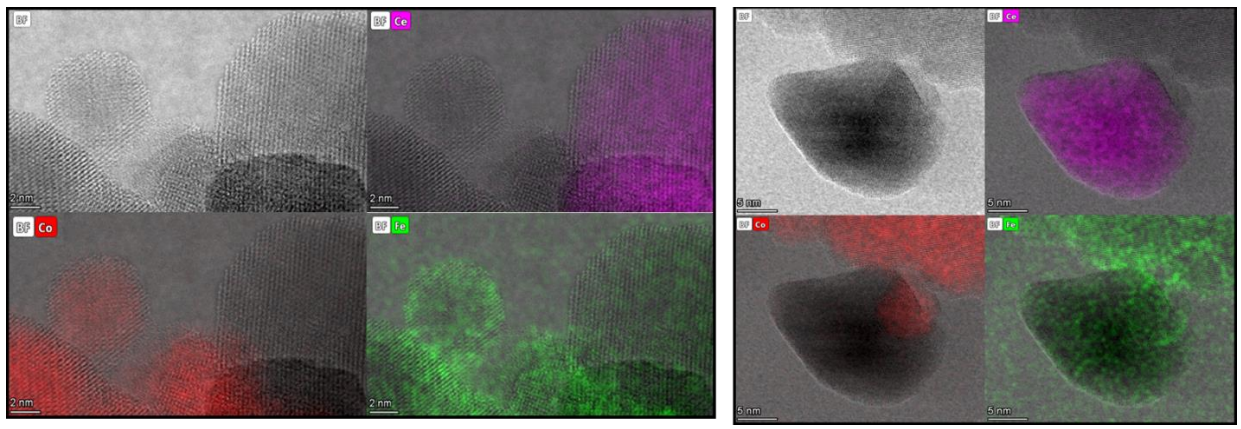

Figure 9.6: Bright field STEM image and elemental maps of Ce, Co, and Fe for (a) 0.5 wt.% FeO_x (b) 1 wt.% FeO_x.

Temperature Programmed Reduction

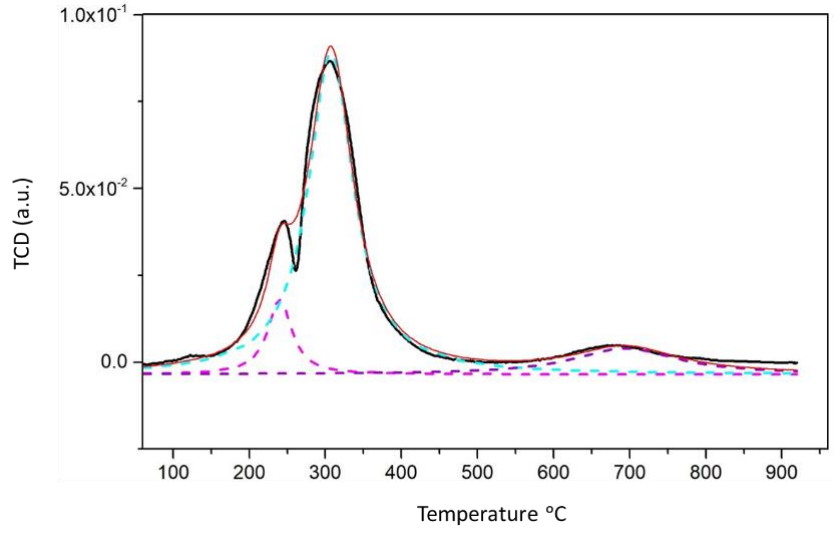

Figure 9.7: Deconvulated hydrogen consumption profile for unpromoted catalyst. Solid black line - raw data, red solid line - cumulative curve, and dotted lines- fitted lines.

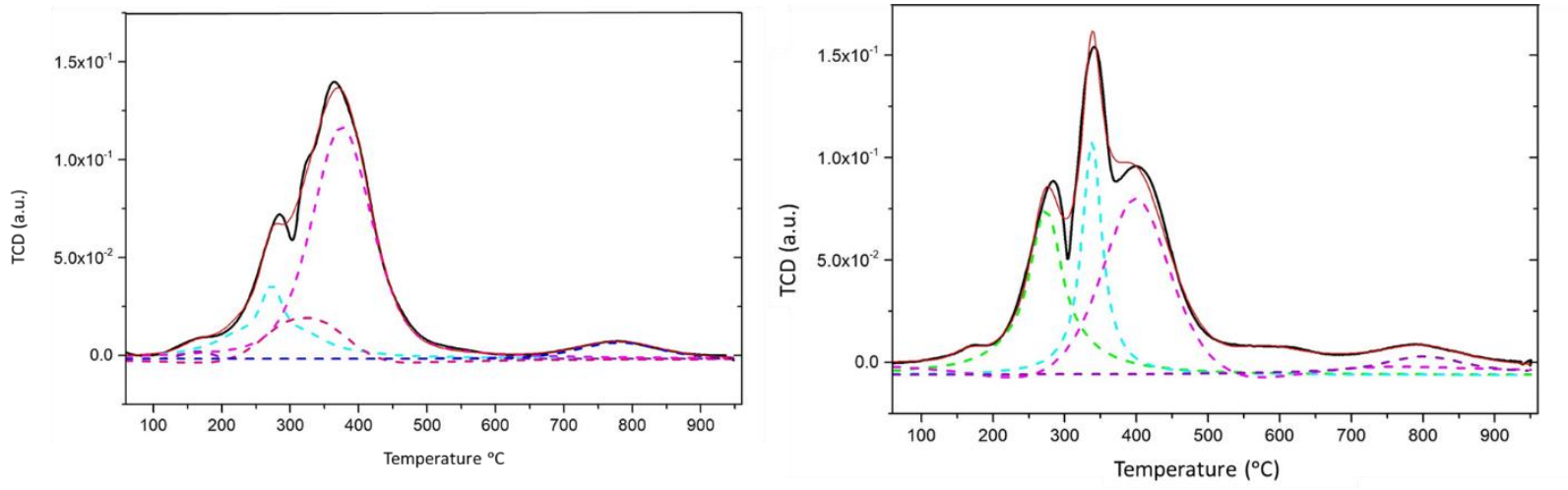

Figure 9.8: Deconvulated hydrogen consumption profiles for (a) 0.3 wt.% MnO_x and (b) 1 wt.% MnO_x. Solid black line - raw data, red solid line - cumulative curve, and dotted lines- fitted lines.

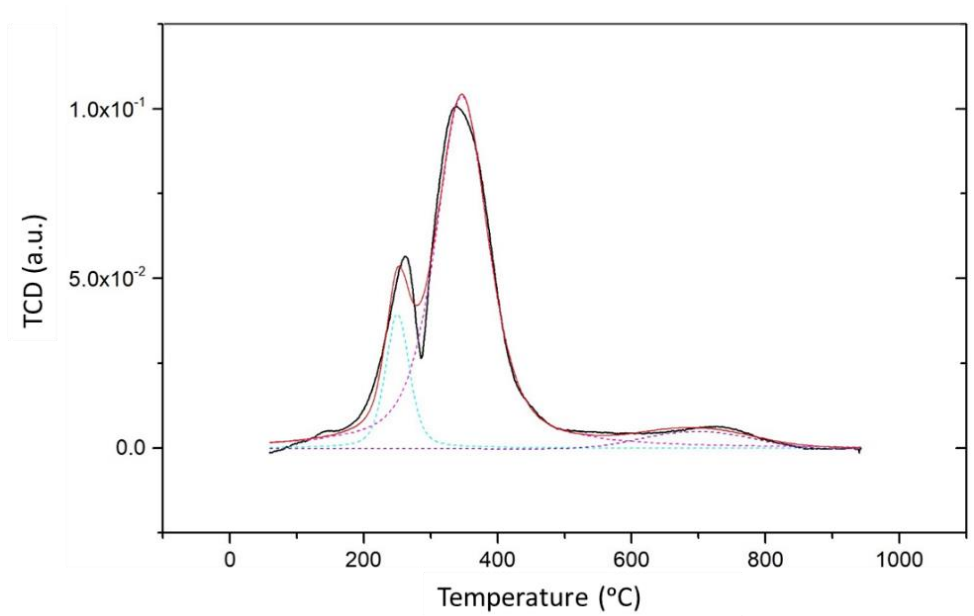

Figure 9.9: Deconvulated hydrogen consumption profile for (a) 0.3 wt.% FeO_x. Solid black line - raw data, red solid line - cumulative curve, and dotted lines- fitted lines.

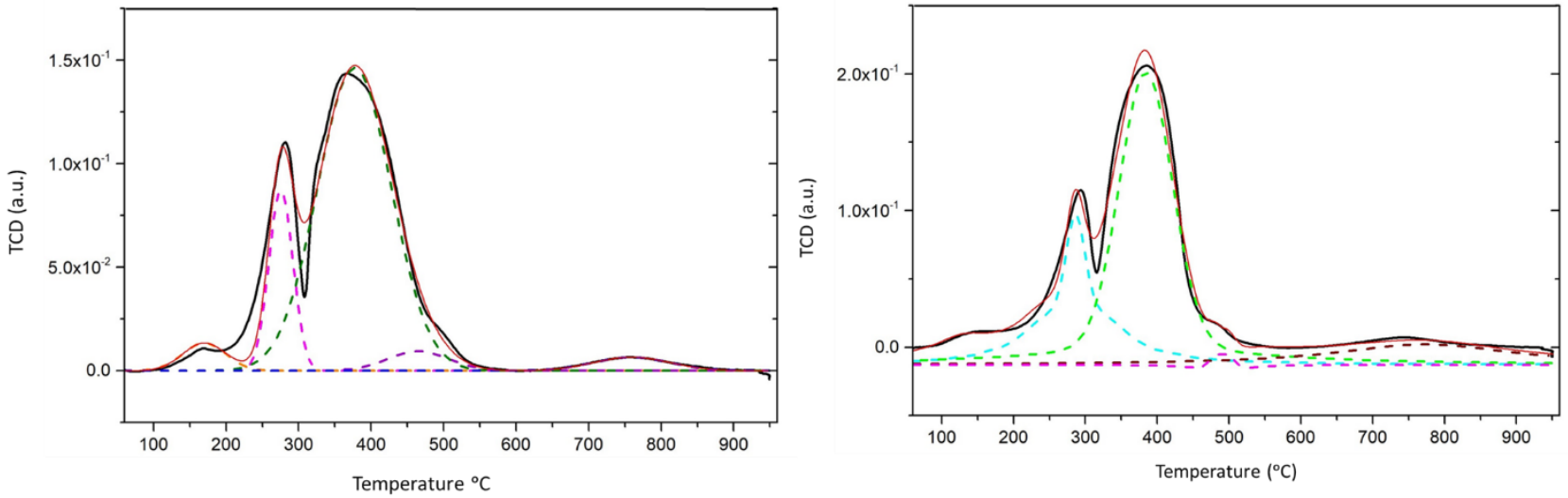

Figure 9.10: Deconvulated hydrogen consumption profile for (a) 0.5 wt.% FeO_x and (b) 1 wt.% FeO_x . Solid black line - raw data, red solid line - cumulative curve, and dotted lines- fitted lines.

Temperature Programmed Oxidation

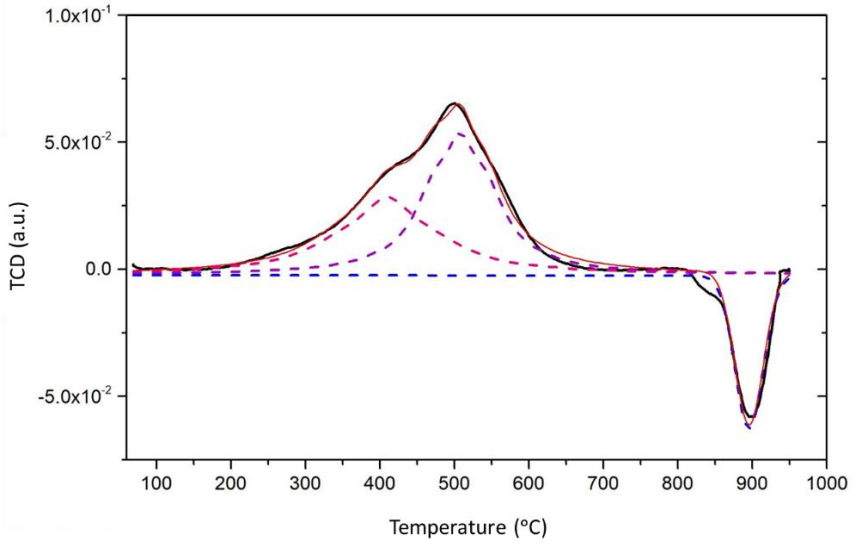

Figure 9.11: Deconvulated oxygen consumption profile for unpromoted catalyst. Solid black line - raw data, red solid line - cumulative curve, and dotted lines- fitted lines.

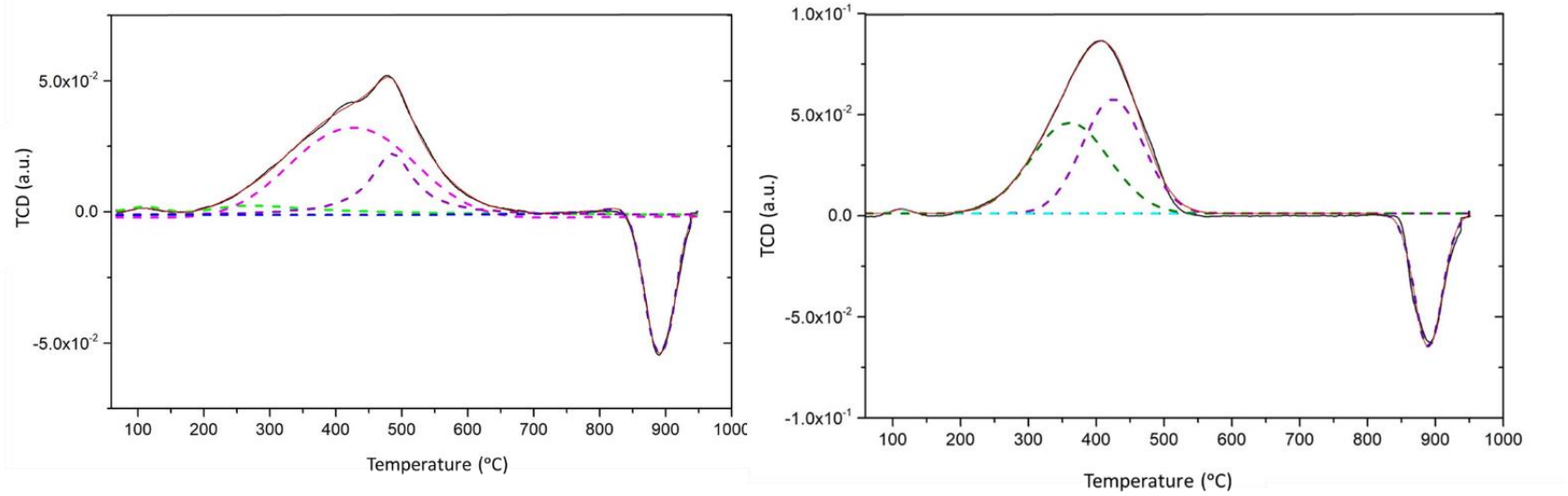

Figure 9.12: Deconvulated oxygen consumption profile for (a) 0.3 wt.% MnO_x and (b) 1 wt.% MnO_x . Solid black line - raw data, red solid line - cumulative curve, and dotted lines- fitted lines.

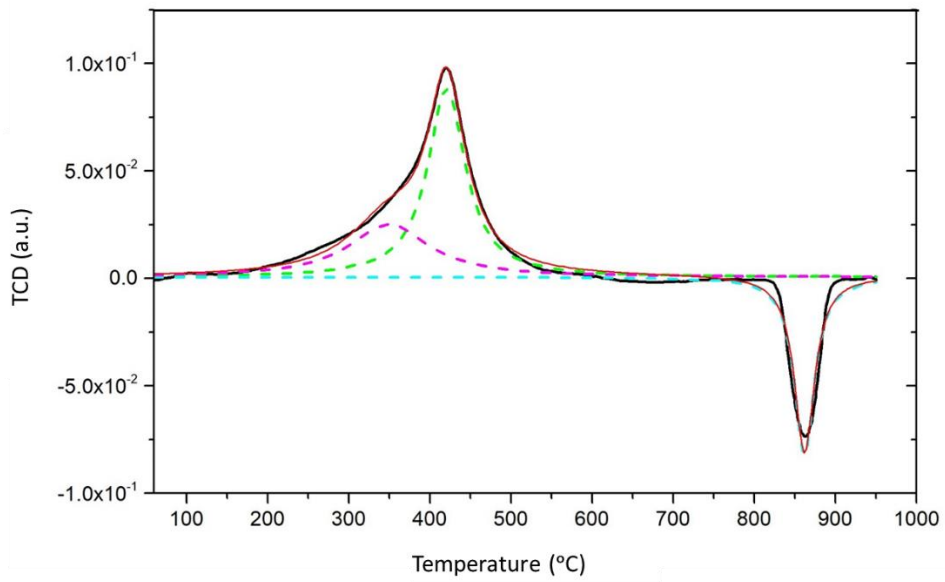

Figure 9.13: Deconvulated oxygen consumption profile for 0.3 wt.%. FeO_x. Solid black line - raw data, red solid line - cumulative curve, and dotted lines- fitted lines.

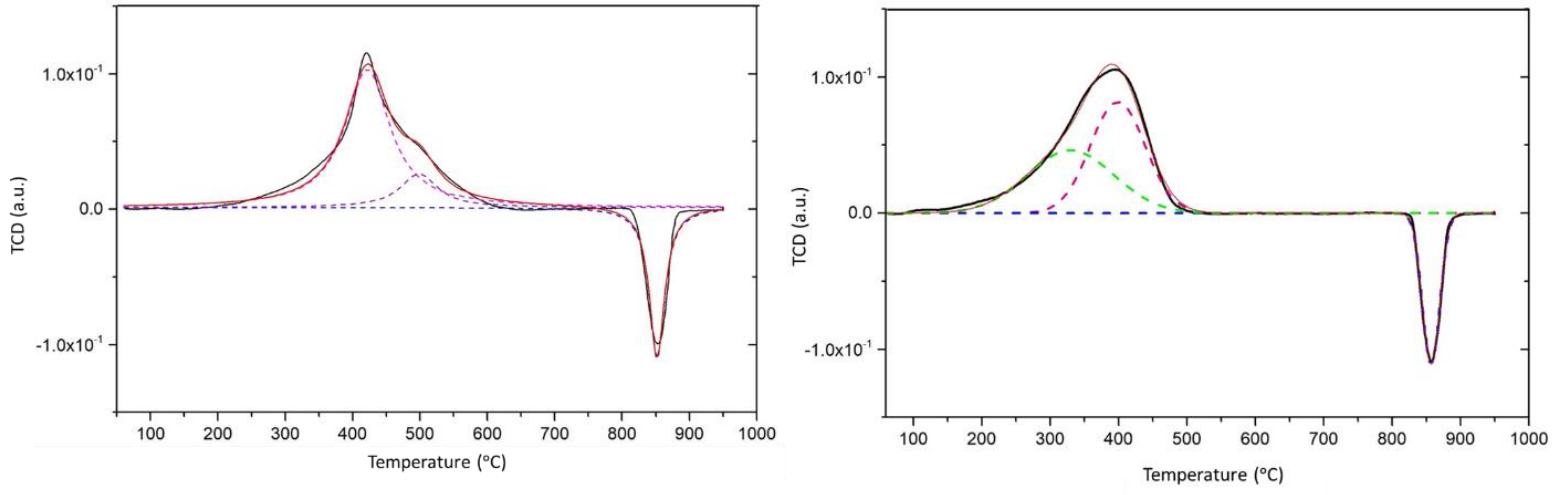

Figure 9.14: Deconvulated oxygen consumption profile for 0.5 wt.% FeO_x and (b) 1 wt.% FeO_x . Solid black line - raw data, red solid line - cumulative curve, and dotted lines- fitted line.

CO-Temperature Programmed Reaction (Carbon mass balance)

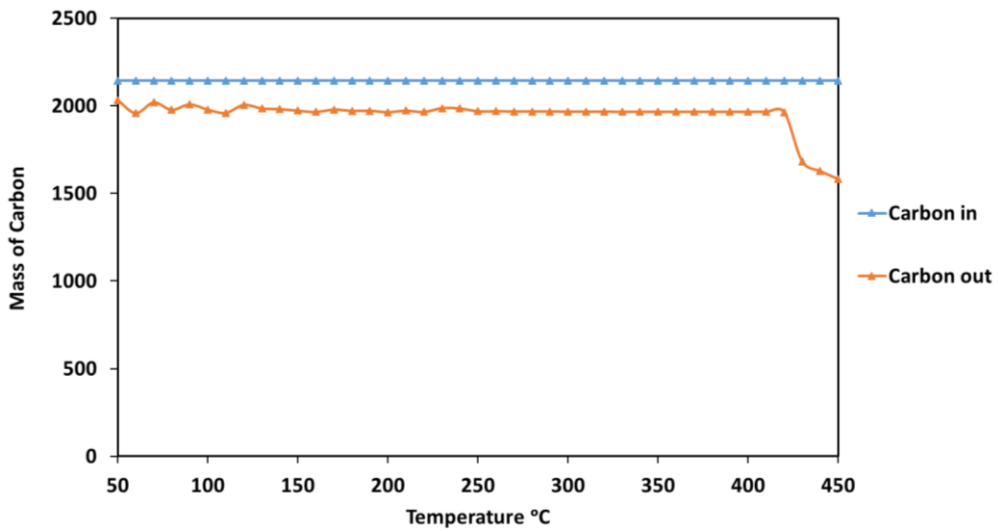

Figure 9.15: Deconvulated oxygen consumption profile for 0.5 wt.% FeO_x and (b) 1 wt.% FeO_x . Solid black line - raw data, red solid line - cumulative curve, and dotted lines- fitted line.

Used catalyst characterization

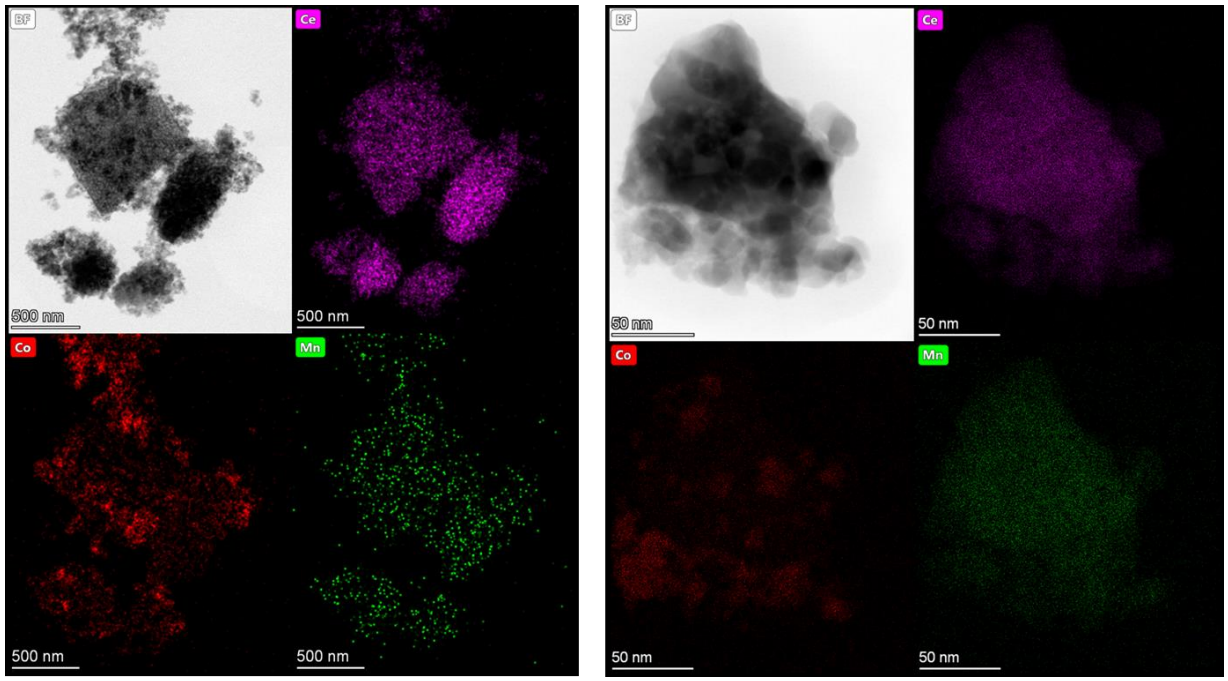

Figure 9.16: Bright-field images and High-Angle Annular Dark field elemental maps for Ce, Co, or Mn (A)0.5 wt.% MnO_x promoted catalyst (B) 1.0 wt.% MnO_x promoted catalyst.

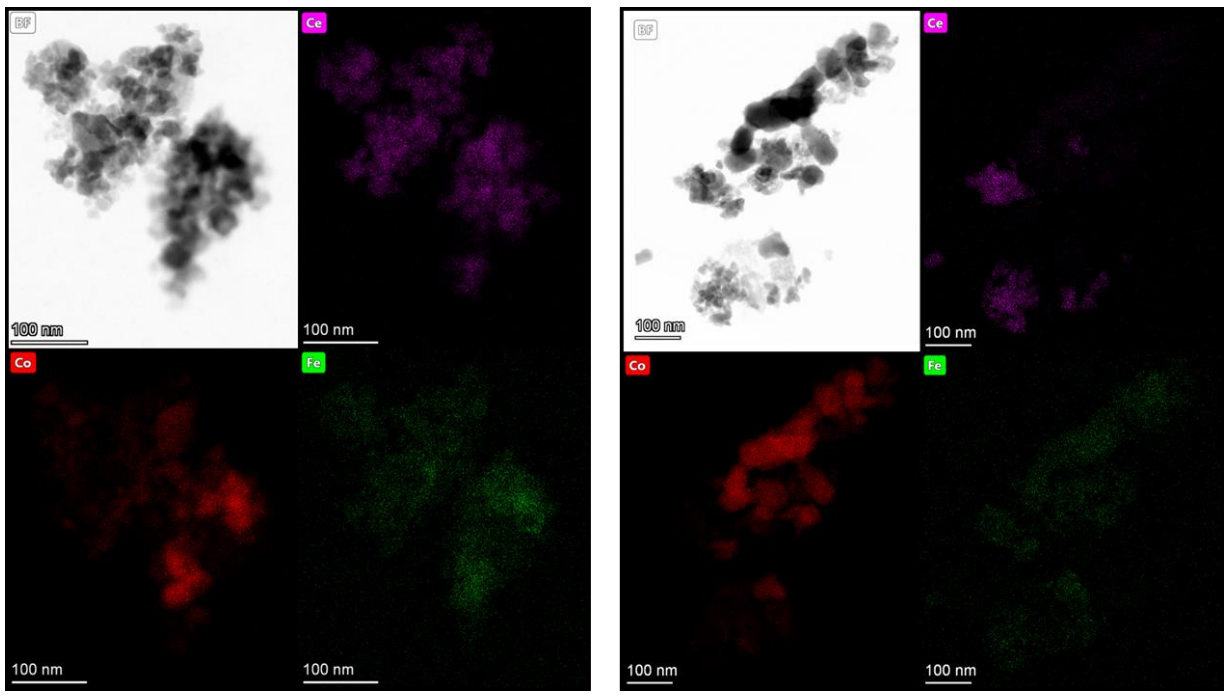

Figure 9.17: Bright-field images and High-Angle Annular Dark field elemental maps for Ce, Co, or Fe (A)0.5 wt.% MnO_x promoted catalyst (B) 1.0 wt.% FeO_x promoted catalyst.